

# Predicting superheavy dark matter of $10^{12}$ GeV and GUT-scale axion or GW radiation of $10^5$ Hz from structure formation and evolution

Zhijie (Jay) Xu,<sup>1\*</sup>

<sup>1</sup>Physical and Computational Sciences Directorate, Pacific Northwest National Laboratory; Richland, WA 99354, USA

Accepted XXX. Received YYY; in original form ZZZ

## ABSTRACT

Two approaches are presented for the nonlinear dark matter structures formation and evolution. Both approaches suggest a superheavy dark matter with a critical mass of  $10^{12}$  GeV along with gravitationally produced axion of mass  $10^{-9}$  eV or gravitational wave (GW) radiation of frequency  $10^5$  Hz released during structure formation. Dark matter particles of this mass can have a free streaming mass equal to the particle mass and form the smallest structure among all particles of any mass. In the radiation era, large-scale structures are suppressed because of rapid expansion. However, small-scale nonlinear structures can still form and evolve via direct collisions, enabled by the kinetic energy associated with the gravity of large-scale density perturbations. In the "bottom-up" approach, particles of this critical mass can form the smallest haloes of two particles as early as  $10^{-6}$  s with a density ratio of  $32\pi^2$  from the spherical collapse model. The halo mass increases rapidly to  $10^8 M_\odot$  at the matter-radiation equality to allow for an early and rapid galaxy formation and to  $10^{13} M_\odot$  that matches observations at  $z = 0$ . Halo growth eventually slows down due to the self-limiting from dark energy. In the "top-down" approach, the mass and energy cascades are identified for hierarchical structure formation with a scale-independent constant rate of the energy cascade  $\varepsilon_u \approx 10^{-7} m^2/s^3$ . The energy cascade leads to universal scaling laws on relevant scales  $r$ , that is, a two-thirds law for the kinetic energy ( $v_r^2 \propto \varepsilon_u^{2/3} r^{2/3}$ ) and a four-thirds law for the halo inner density ( $\rho_r \propto \varepsilon_u^{2/3} G^{-1} r^{-4/3}$ ), where  $G$  is the gravitational constant. By extending these scalings down to the smallest structure scale where three constants ( $\varepsilon_u$ ,  $\hbar$  and  $G$ ) dominate the physics, we can estimate the particle mass  $m_X = (\varepsilon_u \hbar^5 G^{-4})^{1/9} = 10^{12}$  GeV, size  $l_X = (\varepsilon_u^{-1} \hbar G)^{1/3} = 10^{-13}$  m, and a characteristic time  $\tau_X = c^2/\varepsilon_u = 10^{16}$  years. Both approaches suggest a particle mass of  $10^{12}$  GeV along with a binding energy  $E_X = (\varepsilon_u^5 \hbar^7 G^{-2})^{1/9} = 10^{-9}$  eV that strongly suggests a radiation field associated with the structure formation. For dark matter of  $10^{12}$  GeV, superheavy sterile neutrino can be a good candidate that also solves the neutrino mass puzzle and baryon asymmetry. For radiation of  $10^5$  Hz, natural candidates are the high-frequency gravitational wave or gravitationally produced axions by a rapidly varying spacetime metric due to the structure formation in the early universe. If exists, axion radiation should be produced around  $t_X = (\varepsilon_u^{-5} \hbar^2 G^2)^{1/9} = 10^{-6}$  s (QCD phase transition) with a mass of  $10^{-9}$  eV, a GUT scale decay constant  $10^{16}$  GeV, and an effective axion-photon coupling  $10^{-18}$  GeV<sup>-1</sup>. The energy density of this radiation is estimated to be about 1% of the CMB photons. This work suggests a heavy dark matter scenario along with axion/GW radiation. Potential extensions to self-interacting dark matter are also presented.

**Key words:** Dark matter; radiation; axion; gravitational wave; Simulation; Theory;

## CONTENTS

- 1 Introduction
- 2 Free streaming and critical particle mass
- 3 Spherical collapse model in radiation era
- 4 Structure formation by direct collisions
- 5 Nonlinear halo evolution in radiation era
- 6 Modified WIMP miracle involving gravity
- 7 Mass and energy cascade in dark matter
- 8 Inverse mass cascade in halo mass space
- 9 Energy cascade in halo mass space
- 10 Cosmic energy evolution
- 11 Energy cascade in spherical haloes
- 12 Scaling laws and halo density profiles
- 13 Dark matter particle mass and properties
- 14 The nature of cold dark matter
- 15 Axion and gravitational wave radiation
- 16 Self-interacting dark matter
- 17 Conclusions

© 2024 The Authors

\* E-mail: zhijie.xu@pnnl.gov;

## 1 INTRODUCTION

Numerous astronomical observations support the existence of dark matter (DM). The most striking indications come from the dynamical motions of astronomical objects. The flat rotation curves of spiral galaxies point to the existence of galactic dark matter haloes with a total mass much greater than that of luminous matter [1, 2]. Although the nature of dark matter is still unclear, the cold dark matter (CDM) hypothesis, emerging in the early 1980s [3], has quickly become a leading component in the theory of formation and evolution of cosmic structures. Incorporating CDM with the cosmological constant ( $\Lambda$ ) representing the dark energy, the  $\Lambda$ CDM theory is now generally considered the "standard" model of cosmology. Recent Planck measurements of the cosmic microwave background (CMB) anisotropies conclude that the amount of dark matter is about 5.3 times that of baryonic matter based on the  $\Lambda$ CDM cosmology [4].

In the standard  $\Lambda$ CDM paradigm, dark matter is cold (nonrelativistic), collisionless, dissipationless, nonbaryonic, and barely inter-

acts with baryonic matter except through gravity [5, 6, 7, 8]. Despite its great success in the formation and evolution of large-scale structures, there are theoretical and observational difficulties as well [9, 10, 11]. These are the so-called small-scale challenges to the  $\Lambda$ CDM paradigm, where predictions of cold dark matter on small scales are inconsistent with some observations. These challenges are generally known as the core-cusp problem [12, 13], the missing satellite problem [14, 15], the problem of "too big to fail" [16, 17], and the diversity problem in the shape of dwarf galaxy rotation curves [18]. Some non-cold and non-collisionless dark matter models beyond the  $\Lambda$ CDM framework were proposed to address these issues. Examples are warm dark matter (WDM) with a steep suppression of the power spectrum at small scales [19, 20, 21] and self-interacting dark matter (SIDM) [22, 23]. Within the standard  $\Lambda$ CDM cosmology, baryonic feedback mechanisms were also proposed to solve these small-scale challenges, especially the core-cusp problem [10, 24].

Whether these conflicts between  $\Lambda$ CDM and observations can be fully resolved by baryonic physics or require different dark matter models beyond  $\Lambda$ CDM is still under debate. However, the difficulty of  $\Lambda$ CDM on small scales certainly reflects the missing components in our current understanding. These missing components can generally be classified into two categories: 1) within the  $\Lambda$ CDM framework, including a better understanding of baryon physics and cold dark matter physics; 2) beyond the  $\Lambda$ CDM, including new dark matter models beyond CDM or even the nature of gravity (modified gravity theory, etc.). The  $\Lambda$ CDM model has great success in the formation and evolution of large-scale structures, the abundance of different forms of matter and energy, and its predictive power, which has already been tested against many discoveries.

Taking this into account, the first step in solving these difficulties and identifying the nature of dark matter should be to fully explore and exhaust all possible options within the  $\Lambda$ CDM theory (i.e., the first category). Along this line, natural questions are: Are there any missing components in our current understanding of cold dark matter within  $\Lambda$ CDM? If so, what are they? Can we postulate the cold dark matter particle mass and properties based on these new understandings? The answers to these questions are critical for detecting dark matter and supporting/rejecting the CDM hypothesis. Therefore, using cosmological N-body simulations and observational data, this paper proposes new understandings of cold dark matter and their impacts on the mass and properties of cold dark matter particles and structure formation and evolution within the  $\Lambda$ CDM paradigm.

Though the nature and properties of dark matter are still a great mystery, the leading cold dark matter candidate is often assumed to be a thermal relic, weakly interacting massive particles (WIMPs) that were in local equilibrium in the early universe [25]. These thermal relics freeze out as the reaction rate becomes comparable with the expansion rate of the universe. The self-annihilation cross-section required by the right abundance of DM is of the same order as the typical electroweak cross-section, in alignment with the supersymmetric extensions of the standard model ("WIMP miracle") [26]. The mass of thermal WIMPs ranges from a few GeV to hundreds GeV, with the unitarity argument giving an upper bound of several hundred TeV [27]. However, no conclusive signals have been detected in direct or indirect searches for thermal WIMPs in this mass range. This suggests a different thinking is required beyond the standard WIMP paradigm. The other strongly motivated dark matter candidate can be the axion particles from the Peccei–Quinn (PQ) solution to the strong CP problem. Axions satisfy two conditions of cold dark matter: a sufficient non-relativistic amount and the effectively collisionless nature [28]. In addition, the relativistic axion can also be

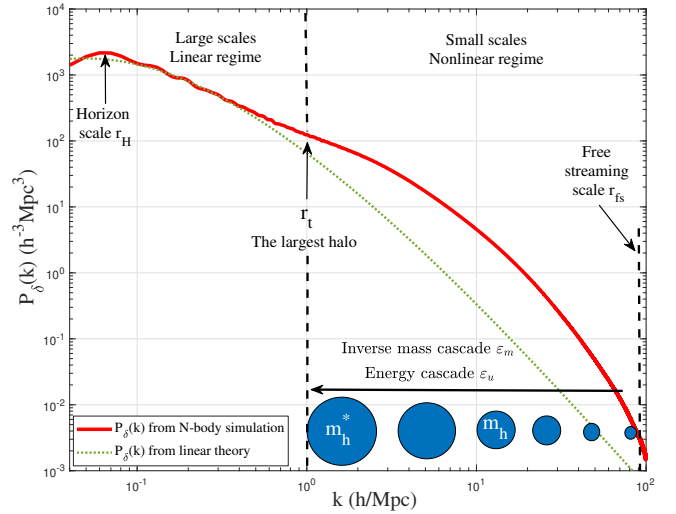


**Figure 1.** The variation of density power spectrum  $P_\delta(k)$  with comoving wavenumber  $k$  at  $z=0$ . Three important scales are identified. The pivot wavenumber denotes the size of the horizon  $r_H$  at the matter-radiation equality. The scale  $r_t \approx 1 \text{ Mpc}/h$  is roughly the size of the largest halo  $m_h^*$  ( $z=0$ ). The free streaming scale  $r_{fs}$  represents the scale of the smallest nonlinear structure that can be formed as early as in the radiation era. The linear theory is in good agreement with N-body simulation on large scales  $r > r_t$  (linear regime). On small scales  $r < r_t$  (nonlinear regime), the linear theory does not apply and significantly underestimates the power spectrum. In this paper, we rely on analytical tools (spherical collapse model and halo-mediated mass and energy cascade) and numerical tools (N-body simulations) for nonlinear structure formation and evolution in both eras.

a promising candidate for dark radiation due to its small mass and weak interaction with standard-model particles [29, 30].

In this paper, we aim to new understandings of the nonlinear structure formation and evolution in both radiation and matter eras. Based on these new findings, we postulate the possible mass and properties of cold dark matter particles. Here, we do not exclude any other dark matter models beyond the  $\Lambda$ CDM. Instead, we focus on the self-gravitating, cold, and collisionless particle dark matter within the  $\Lambda$ CDM framework that is sufficiently smooth on large scales with a fluid-like behavior. With that in mind, a complete understanding of the dynamics of dark matter flow on different scales may provide key insights into the properties of cold dark matter particles by extending these dynamics consistently down to small scales. Compared to other dark matter models, a major advantage of this approach is the consistency between dark matter particle mass and properties on small scales and the dynamics of dark matter haloes on large scales (see Fig. 29).

To facilitate the discussion, we first identify three important scales in the density spectrum of dark matter. Figure 1 presents the variation of the power spectrum with the comoving wavenumber  $k$  from N-body simulations carried out by the Virgo consortium (SCDM) [31]. The pivot wavenumber denotes the size of the horizon  $r_H$  at the matter-radiation equality. The scale  $r_t$  roughly corresponds to the size of the largest halo that separates the small scales in a non-linear regime and the large scales in a linear regime. The free streaming scale  $r_{fs}$  represents the scale of the smallest nonlinear structure that can be formed. The linear theory predictions (green dotted line from [32]) are in good agreement with N-body simulations on large scales greater than  $r_t$ . Linear perturbations on large scales are suppressed during the radiation-dominated era (Meszaros effect) and grow  $\propto a$  during the matter-dominated era. However, the structure evolution

on small scales smaller than  $r_t$  is highly non-linear and can only be studied by N-body simulations with the Newtonian approximation or simplified analytical tools (spherical collapse model in Section 3). The mass and energy cascade theory in this paper provides another analytical approach for the nonlinear structure formation and evolution on small scales (Sections 7).

The paper is structured as follows. Sections 2 to 5 focus on a "bottom-up" approach to the nonlinear structure formation and evolution in the radiation and matter eras. Section 2 identifies a critical particle mass of  $10^{12}\text{GeV}$  that is comparable to the particle free streaming mass. Section 3 introduces the spherical collapse model for both the matter and the radiation eras. Since the energy density of radiation significantly counteracts gravity during the radiation era, Sections 4 and 5 present the nonlinear structure formation and evolution by direct collisions. Sections 7 to 12 focus on a "top-down" approach to structure evolution. Section 7 introduces the mass and energy cascades in dark matter flow, followed by quantitative descriptions and numerical results in Sections 8 to 11. Section 12 establishes the scaling laws associated with the energy cascade that results in a halo inner density slope of  $-4/3$ . By extending the established scaling laws to the smallest scale, section 13 provides the dark matter particle mass ( $10^{12}\text{GeV}$ ) and properties that are consistent with the structure formation and evolution in both eras. Section 14 discusses several potential candidates for this heavy dark matter, especially the superheavy sterile neutrinos. A dark radiation field is also identified to be associated with structure formation, which can be high-frequency gravitational waves or nano-eV axion. Their properties and abundance are inferred in Section 15. The theory is extended to self-interacting dark matter in Section 16.

## 2 FREE STREAMING AND CRITICAL PARTICLE MASS

The smallest scale of dark matter haloes is sometimes called the "free-streaming" scale (Fig. 1). The thermal velocities of dark matter particles (traditionally denoted as the "X" particles) tend to erase the primordial perturbations below that scale. There are no coherent structures on scales smaller than the free streaming scale, where dark matter particles form a smooth background. In this Section, we provide a brief analysis of the free-streaming scale  $M_{fs}$ . A critical particle mass  $m_{Xc}$  is then identified that exactly equals the free streaming mass, i.e.,  $M_{fs}(m_{Xc}) = m_{Xc}$ , which is relevant to the smallest possible dark matter structure.

The free streaming scale depends on both the mass of dark matter particles and the formation mechanism. It is usually quantified by the comoving length a particle travels before primordial perturbations start to grow significantly, which is around the time  $t_{eq}$  for matter-radiation equality. The comoving free streaming length  $\lambda_{fs}$  is

$$\begin{aligned} \lambda_{fs}(t) &= \int_0^{t_{eq}} \frac{\sigma_{DM}(t)}{a(t)} dt \\ &= \int_0^{t_1} \frac{\sigma_{DM}}{a} dt + \int_{t_1}^{t_2} \frac{\sigma_{DM}}{a} dt + \int_{t_2}^{t_{eq}} \frac{\sigma_{DM}}{a} dt, \end{aligned} \quad (1)$$

where  $\sigma_{DM}(t)$  is the particle thermal velocity, and  $a(t)$  is the scale factor. Two time scales,  $t_1$  and  $t_2$ , represent either the time when particles become non-relativistic ( $t_{NR}$ ) or the time when particles fall out of the thermal equilibrium and decouple (freeze-out) from the background ( $t_{dec}$ ), depending on the nature of dark matter. For hot relics (hot dark matter), particles become non-relativistic after decoupling ( $t_{NR} > t_{dec}$ ) and, therefore,  $t_1 = t_{dec}$  and  $t_2 = t_{NR}$ . For cold relics (cold dark matter), particles become non-relativistic before decoupling ( $t_{NR} < t_{dec}$ ), such that  $t_1 = t_{NR}$  and  $t_2 = t_{dec}$ .

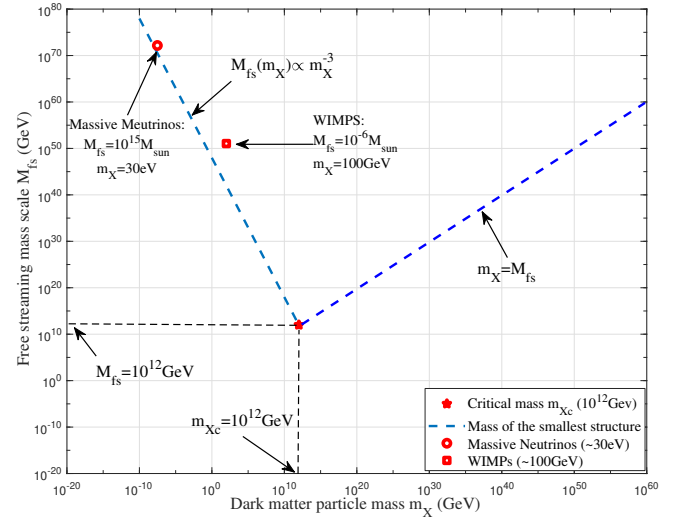


**Figure 2.** The free streaming mass  $M_{fs}$  decreases with the particle mass  $m_X$ . Hot massive neutrinos with a mass of 30eV can have a free streaming mass  $M_{fs} \approx 10^{15} M_\odot$  (circle). For WIMP particles with a mass of 100GeV,  $M_{fs} \approx 10^{-6} M_\odot$  (square). In this work, the calculated free streaming mass  $M_{fs}$  for dark matter particles of mass  $m_X$  follows the scaling  $M_{fs} \propto m_X^{-3}$  (Eq. (9)). A critical particle mass  $m_{Xc}$  can be identified where  $m_{Xc} = M_{fs}(m_{Xc}) \approx 10^{12}\text{GeV}$  (Eq. (10)). The dashed line plots the mass of the smallest structure ( $M_S$ ) that particles of mass  $m_X$  can form. For particles with mass  $m_X < m_{Xc}$ , the mass of the smallest structure  $M_S = M_{fs}$ . For particles with mass  $m_X > m_{Xc}$ ,  $M_S = m_X$  because the free streaming mass is smaller than the particle mass, and the structure cannot be smaller than the particle itself. Therefore,  $M_S = \max(M_{fs}, m_X)$ . The critical mass  $m_{Xc}$  represents the mass of the smallest structure that dark matter particles of all different masses can form. Since smaller structures were formed earlier, particles of critical mass  $m_{Xc}$  also form the earliest structure (Section 4).

For the radiation era before the matter-radiation equality, the scale factor  $a(t) \propto t^{1/2}$ . The free streaming mass  $M_{fs}$  reads

$$M_{fs} = \frac{\pi}{6} \rho_{DM0} \lambda_{fs}^3, \quad (2)$$

where  $\rho_{DM0}$  is the dark matter density at  $z = 0$ .

The thermal velocity  $\sigma_{DM}(t)$  also varies in different regimes: i)  $\sigma_{DM}(t) = c$  when the particles are still relativistic ( $t < t_{NR}$ ). During this stage, the free streaming length  $\lambda_{fs} \propto a$ ; ii)  $\sigma_{DM}(t) \propto a^{-1/2}$  when the particle becomes non-relativistic, but still coupled ( $t_{NR} < t < t_{dec}$ ). During this stage, the free streaming length  $\lambda_{fs} \propto a^{1/2}$ ; and iii)  $\sigma_{DM}(t) \propto a^{-1}$  when the particles become non-relativistic, but also decoupled ( $t > t_{dec}$  and  $t > t_{NR}$ ). During this stage,  $\lambda_{fs} \propto a^0$  is independent of time.

An alternative way of understanding the free streaming scale is via the comoving Jeans length:

$$\lambda_J(t) = \frac{\sigma_{DM}(t)}{a(t)} \sqrt{\frac{\pi}{G \bar{\rho}(t)}}, \quad (3)$$

where  $\bar{\rho}(t) \propto a^{-4}$  is the background density in the radiation era. Only perturbations greater than the Jeans length will gravitationally collapse into haloes. Perturbations smaller than the Jean's length will be damped out. The variation of  $\lambda_J(t)$  over time is similar to the variation of free streaming length  $\lambda_{fs}(t)$ .

Based on these calculations, we can estimate a free streaming mass  $M_{fs} \approx 10^{15} M_\odot$  for hot massive neutrinos with a mass around 30eV. This is more likely due to the smaller particle mass, so the particles become non-relativistic much later, leading to larger free streaming

length and mass. Therefore, for hot dark matter, the structure formation proceeds "top-down," which is inconsistent with observations. For WIMP particles with a much higher mass of 100 GeV, the free streaming mass is around  $M_{fs} \approx 10^{-6} M_\odot$  (the mass of the Earth) [33]. Cold dark matter like WIMPs takes hierarchical "bottom-up" structure formation that is in better agreement with observations. Thus, the smallest structure that can form by dark matter particles of a given mass is radically different. The larger the particle mass  $m_X$ , the smaller the free streaming mass  $M_{fs}$ .

Figure 2 plots the decreasing  $M_{fs}$  with the particle mass  $m_X$ . There should exist a critical particle mass  $m_{Xc}$  such that  $M_{fs}$  is exactly equal to the particle mass ( $M_{fs}(m_{Xc}) \equiv m_{Xc}$ ). Particles with a mass smaller than this critical mass  $m_{Xc}$  should form the smallest structure with a mass equal to their free streaming mass. For particles with a mass greater than  $m_{Xc}$ , its free streaming mass is smaller than the particle mass such that the smallest structure formed by these particles should have a mass equal to the particle mass. Therefore,  $m_{Xc}$  represents the mass of the smallest possible dark matter structure. Next, we will determine this critical mass  $m_{Xc}$ .

For cold dark matter particles, the non-relativistic time  $t_{NR} \leq t_{dec}$ . We consider the free streaming length from the first term in Eq. (1) (free streaming before  $t_{NR}$ ):

$$\lambda_{fs} = \int_0^{t_{NR}} \frac{c}{a(t)} dt = \frac{2ct_{NR}}{a_{NR}} = \frac{c}{H_0} \frac{a_{NR}}{\sqrt{\Omega_{rad}}}, \quad (4)$$

where  $a_{NR}$  is the scale factor when particles become non-relativistic. Here, we use the relation in the radiation era ( $t \propto a^2$ ),

$$t = \frac{a^2}{2H_0\sqrt{\Omega_{rad}}}, \quad (5)$$

where  $\Omega_{rad}$  is the mass fraction of radiation at  $z = 0$ . Now we determine the free streaming mass  $M_{fs}$  using Eqs. (4) and (2),

$$M_{fs} = \frac{\pi}{6} \Omega_{DM} \bar{\rho}_0 \left( \frac{c}{H_0} \frac{a_{NR}}{\sqrt{\Omega_{rad}}} \right)^3, \quad (6)$$

where  $\Omega_{DM}$  is the mass fraction of dark matter at  $z = 0$ . The critical density of the universe is  $\bar{\rho}_0 = 3H_0^2/8\pi G$ . The scale factor  $a_{NR}$  also depends on the mass of the particles  $m_X$ . Dark matter particles become non-relativistic when the radiation temperature  $T_\gamma$  is comparable to the particle mass,

$$3k_B T_\gamma(a_{NR}) = m_X c^2 \quad \text{and} \quad T_\gamma(a) = T_{\gamma 0} a^{-1}, \quad (7)$$

where the radiation temperature redshifts with time as  $T_\gamma \propto a^{-1}$ . Here,  $T_{\gamma 0} = 2.7K$  is the radiation temperature (CMB) at  $z = 0$ . Solve Eq. (7), the scale factor  $a_{NR}$  should read

$$a_{NR} = \frac{3k_B T_{\gamma 0}}{m_X c^2}. \quad (8)$$

Inserting  $a_{NR}$  into Eq. (6) leads to the free streaming mass

$$M_{fs} = \frac{1}{16} \left[ \frac{\Omega_{DM}}{\Omega_{rad}^{3/2}} \frac{(3k_B T_{\gamma 0})^3}{G H_0 c^3} \right] m_X^{-3} \propto m_X^{-3}. \quad (9)$$

Let  $M_{fs} = m_X$ , we found the critical particle mass  $m_{Xc}$ :

$$m_{Xc} = \frac{1}{2} \left[ \frac{\Omega_{DM}}{\Omega_{rad}^{3/2}} \frac{(3k_B T_{\gamma 0})^3}{G H_0 c^3} \right]^{\frac{1}{4}} \approx 1.5 \times 10^{-15} \text{ kg}. \quad (10)$$

This is a very important mass scale, as we will revisit it very often.

We may also relate the critical mass  $m_{Xc}$  to quantities at the Planck scale. Radiation density decreases as  $\propto a^{-4}$  such that

$$\Omega_{rad} \bar{\rho}_0 a_p^{-4} = \alpha_p \rho_p \quad \text{and} \quad \rho_p = c^5/(\hbar G^2), \quad (11)$$

$$T_{\gamma 0} a_p^{-1} = \beta_p T_p \quad \text{and} \quad T_p = \sqrt{\hbar c^5/(G k_B^2)},$$

where  $a_p$  is defined as the scale factor corresponding to the Planck time  $t_p = \sqrt{\hbar G/c^5} = 5.4 \times 10^{-44} \text{ s}$ . Here,  $\rho_p$  is the Planck density,  $T_p$  is the Planck temperature, and  $\alpha_p$  and  $\beta_p$  are two numerical factors. The scale factor  $a_p$  is related to the Planck time by Eq. (5),

$$a_p = \left( 2H_0 t_p \sqrt{\Omega_{rad}} \right)^{1/2} \approx 4.76 \times 10^{-32}. \quad (12)$$

Substituting Eq. (12) into Eq. (11), we have

$$T_{\gamma 0} = \beta_p T_p \left( \frac{\Omega_{rad} \bar{\rho}_0}{\alpha_p \rho_p} \right)^{1/4}, \quad \alpha_p = \frac{3}{32\pi}, \quad \beta_p \approx \frac{2}{5}. \quad (13)$$

Now, substitute Eq. (13) into Eqs. (8) and (6), the critical particle mass  $m_{Xc}$  can be obtained as

$$m_{Xc} = \frac{1}{2} (3\beta_p)^{\frac{3}{4}} \left( \frac{3}{8\pi\alpha_p} \right)^{\frac{3}{16}} \left( \frac{\Omega_{DM}^2}{\Omega_{rad}^{3/2}} \right)^{\frac{1}{8}} M_{pl} (H_0 t_p)^{\frac{1}{8}} \quad (14)$$

$$\approx 1.5 \times 10^{-15} \text{ kg} = 0.9 \times 10^{12} \text{ GeV}.$$

Here,  $M_{pl} = 2.2 \times 10^{-8} \text{ kg}$  is the Planck mass. The dark matter fraction  $\Omega_{DM} = 0.12/h^2$ , the radiation fraction  $\Omega_{rad} = 4.2 \times 10^{-5}/h^2$ , and  $h = H_0/(100 \text{ km/s/Mpc})$  is the dimensionless Hubble constant. The critical mass  $m_{Xc}$  is completely determined by the mass fractions of dark matter and radiation.

By introducing a new parameter  $\varepsilon_u$  (the rate of change of specific energy with a unit of  $m^2/s^3$ ), we can rewrite the particle mass as a simple function of three parameters  $\varepsilon_u$ ,  $\hbar$  and  $G$ :

$$\varepsilon_u = A \left( \frac{\Omega_{DM}^2}{\Omega_{rad}^{3/2}} H_0 \right)^{\frac{9}{8}} (c^{27} \hbar G)^{\frac{1}{16}} \approx 4 \times 10^{-7} \frac{m^2}{s^3}. \quad (15)$$

$$m_{Xc} = \left( 2^8 \varepsilon_u \hbar^5 G^{-4} \right)^{\frac{1}{5}},$$

where  $A \approx 2.7 \times 10^{-4}$  is a constant. As we will demonstrate (Sections 9 and 11),  $\varepsilon_u$  is a key parameter that represents the rate of energy cascade in dark matter flow and determines the halo density profile (Eq. (132)). The dynamics of large-scale haloes are dominated by  $\varepsilon_u$ , which has a microscopic origin in Eq. (15).

If the X particles have a mass of  $m_{Xc} = 10^{12} \text{ GeV}$ , then they are created at a time around  $t_{NR} = 10^{-29} \text{ s}$  (inflationary epoch) or  $a_{NR} = 10^{-24}$ . They can form the smallest structure among particles of any mass. Since smaller structures were formed earlier, they may also form the earliest structure. In the next section, we discuss the formation and evolution of nonlinear structures in the early universe, which can be highly dependent on the particle mass.

### 3 SPHERICAL COLLAPSE MODEL IN RADIATION ERA

The dark matter particle properties can be highly relevant to the nonlinear structure formation on small scales with overdensity  $\delta \gg 1$ , which is beyond the range of the linear perturbation theory. The structure evolution in the nonlinear regime is very complicated, and, in general, we have to use numerical approaches such as N-body simulations. Very few analytical tools are available. The spherical collapse model (SCM) is a useful approximate model [34], where



gravity is the only dominant force driving the nonlinear structure evolution. Therefore, in this section, it would be very instructive to follow the spherical collapse model and extend it to the radiation era to identify the necessary conditions for nonlinear structure formation and evolution on small scales.

For the spherical collapse model, we consider a spherical overdensity with a fixed given mass  $M$  and size  $R(t)$  that will first reach some maximum size  $R_{ta}$  at a turn-around moment and then collapse due to its self-gravity. We denote the scale factor  $a_{ta}$  at turn-around radius  $R_{ta}$  and introduce dimensionless variables:

$$\tau \equiv H_{ta} t, \quad x \equiv \frac{a}{a_{ta}}, \quad y \equiv \frac{R}{R_{ta}}, \quad (16)$$

where  $H_{ta}$  is the Hubble parameter at turn-around. The equation of motion for non-relativistic spherical overdensity reads [34]

$$\frac{d^2 R}{dt^2} = -\frac{GM}{R^2} = -\frac{4\pi}{3} \rho_{ta} R_{ta}^3 \frac{G}{R^2}, \quad (17)$$

$$\rho_{ta} = \xi_{ta} \bar{\rho}_{ta} = \xi_{ta} \frac{3H_{ta}^2}{8\pi G},$$

where  $\xi_{ta}$  is the ratio between sphere density at turnaround ( $\rho_{ta}$ ) to the background density  $\bar{\rho}_{ta}$  at that moment.

Integrating Eq. (17) leads to a negative constant  $E$  for the specific energy of the gravitationally bounded sphere

$$E = \frac{1}{2} \left( \frac{dR}{dt} \right)^2 - \frac{GM}{R} < 0. \quad (18)$$

Using the dimensionless coordinates in Eq. (16), the equation of motion can be rewritten as (along with the boundary conditions)

$$\frac{d^2 y}{d\tau^2} = -\frac{\xi_{ta}}{2y^2}, \quad (19)$$

$$y|_{x=0} = 0 \quad \text{and} \quad \frac{dy}{d\tau} \Big|_{x=1} = 0,$$

where the spherical overdensity has an initial size  $R(t=0) = 0$  and a vanishing velocity at its maximum size.

The relation between  $x$  and  $\tau$  or (scale factor  $a$  and physical time  $t$ ) depends on the cosmology, i.e. the content of matter  $\Omega_m$ , radiation  $\Omega_{rad}$ , dark energy  $\Omega_\Lambda$ , and the evolution of Hubble parameter  $H$  and background density  $\bar{\rho}$ , such that

$$H = H_0 \sqrt{\Omega_m a^{-3} + \Omega_{rad} a^{-4} + \Omega_\Lambda} \quad \text{and} \quad \bar{\rho} = \frac{3H^2}{8\pi G}. \quad (20)$$

In  $\Lambda$ CDM cosmology,  $x$  and  $\tau$  are related as

$$\frac{dx}{d\tau} = x \sqrt{\frac{\Omega_m a_{ta}^{-3} x^{-3} + \Omega_{rad} a_{ta}^{-4} x^{-4} + \Omega_\Lambda}{\Omega_m a_{ta}^{-3} + \Omega_{rad} a_{ta}^{-4} + \Omega_\Lambda}}. \quad (21)$$

The analytical solution of Eq. (19) can be obtained as

$$\tau = \frac{1}{\sqrt{\xi_{ta}}} \text{acot} \left( \sqrt{\frac{1}{y} - 1} \right) - \frac{y}{\sqrt{\xi_{ta}}} \sqrt{\frac{1}{y} - 1} \quad (22)$$

$$= \int_0^x \frac{1}{x} \sqrt{\frac{\Omega_m a_{ta}^{-3} + \Omega_{rad} a_{ta}^{-4} + \Omega_\Lambda}{\Omega_m a_{ta}^{-3} x^{-3} + \Omega_{rad} a_{ta}^{-4} x^{-4} + \Omega_\Lambda}} dx.$$

At turnaround  $y \equiv x \equiv 1$ , we should have the dimensionless time

$$\tau(y=1) = \frac{\pi}{2\sqrt{\xi_{ta}}} \equiv \tau(x=1). \quad (23)$$

From the analytical solution in Eq. (22), the time derivative (or the velocity term) can be obtained as

$$\frac{dy}{d\tau} = \sqrt{\xi_{ta}} \sqrt{\frac{1}{y} - 1}. \quad (24)$$

Substituting the time derivative into the equation for the specific energy  $E$  (Eq. (18)), the turn-around time and turn-around size are

$$t_{ta} = \pi \frac{GM}{(2|E|)^{3/2}} \quad \text{and} \quad R_{ta} = \frac{GM}{|E|}, \quad (25)$$

where both the turn-around time  $t_{ta}$  and sphere size  $R_{ta}$  are proportional to the shell mass  $M$ , i.e., the larger mass scales collapse at a later time that is consistent with the hierarchical structure formation.

We first consider the matter-dominant universe with  $\Omega_{rad} = \Omega_\Lambda = 0$ . From Eqs. (22) and (23), the critical density ratio at turn-around

$$\tau_{ta} = \tau(x=1) = \frac{2}{3} \quad \text{and} \quad \xi_{ta} = \left( \frac{3\pi}{4} \right)^2 \approx 5.55. \quad (26)$$

Now, we can find the corresponding linear overdensity  $\delta = \rho/\bar{\rho} - 1$ . The ratio between sphere density  $\rho(t)$  and turnaround density  $\rho_{ta}$  is (the evolution of background density  $\bar{\rho} \propto a^{-3}$ )

$$\frac{\rho}{\rho_{ta}} = \frac{1}{y^3}, \quad \frac{\bar{\rho}}{\bar{\rho}_{ta}} = \frac{1}{x^3}, \quad \frac{\rho/\bar{\rho}}{\rho_{ta}/\bar{\rho}_{ta}} = \frac{1+\delta}{\xi_{ta}} = \frac{x^3}{y^3}. \quad (27)$$

From this, the exact relation between variables  $y$  and  $x$  is:

$$y^3 = \left( \frac{3\pi}{4} \right)^2 \frac{x^3}{1+\delta}. \quad (28)$$

Taylor expansion of the solution in Eq. (22) leads to the linear approximation for small  $x$  and  $y$ :

$$\frac{2}{3} x^{3/2} \approx \frac{4}{3\pi} \left( \frac{2}{3} y^{3/2} + \frac{1}{5} y^{5/2} \right). \quad (29)$$

Substitute Eq. (28) into Eq. (29), we obtain the evolution of the linear overdensity  $\delta^{lin} \propto a$  and the linear overdensity  $\delta_{ta}^{lin}$  at turn-around,

$$\delta^{lin} = \frac{3}{5} \left( \frac{3}{4} \pi \right)^{2/3} \frac{a}{a_{ta}} \quad \text{and} \quad \delta_{ta}^{lin} = \frac{3}{5} \left( \frac{3}{4} \pi \right)^{2/3} \approx 1.06. \quad (30)$$

For fully collapsed overdensity that reaches virial equilibrium, the required time should be twice the turn-around time  $t_{vir} = 2t_{ta}$  ( $t \propto a^{3/2}$  in matter-dominant universe). Energy conservation requires the radius of virialized overdensity to be half the turnaround radius  $R_{vir} = R_{ta}/2$ , which leads to the density ratio

$$\frac{\rho_{vir}/\bar{\rho}_{vir}}{\rho_{ta}/\bar{\rho}_{ta}} = \frac{\xi_{vir}}{\xi_{ta}} = \frac{(2^{2/3})^3}{(1/2)^3} = 32. \quad (31)$$

The density ratio at virialization  $\xi_{vir}$  and the corresponding linear overdensity  $\delta_{vir}^{lin}$  are

$$\xi_{vir} = 32\xi_{ta} = 18\pi^2 \quad \text{and} \quad \delta_{vir}^{lin} = 2^{2/3} \delta_{ta}^{lin} \approx 1.69. \quad (32)$$

Figure 3 summarizes the evolution of a linear overdensity  $\delta^{lin}$  (solid red) in the matter era that starts from  $\delta = 0$ , evolves as  $\delta \propto a$  in the linear regime until it reaches a value of 1.06 at the turn-around (entering the nonlinear region), and a value of 1.69 when fully virialized. The actual nonlinear overdensity  $\delta$  (solid blue) can grow much faster and reach a much higher maximum ( $18\pi^2 - 1$ ).

Next, we will extend the same model to a radiation-dominant universe with  $\Omega_m = \Omega_\Lambda = 0$ . In the radiation era, the energy density of radiation significantly counteracts gravity, preventing large-scale structure formation. Gravitational collapse (Eq. (17)) is only possible on very small scales where gravity exceeds expansion. This might occur because of a special phase of universe evolution before the radiation era (early matter dominant era, etc. [35]) or because of some special mechanisms leading to gravitational collapse (Section 4). At this moment, we assume that the spherical collapse can occur and seek its corresponding solutions in the radiation era.

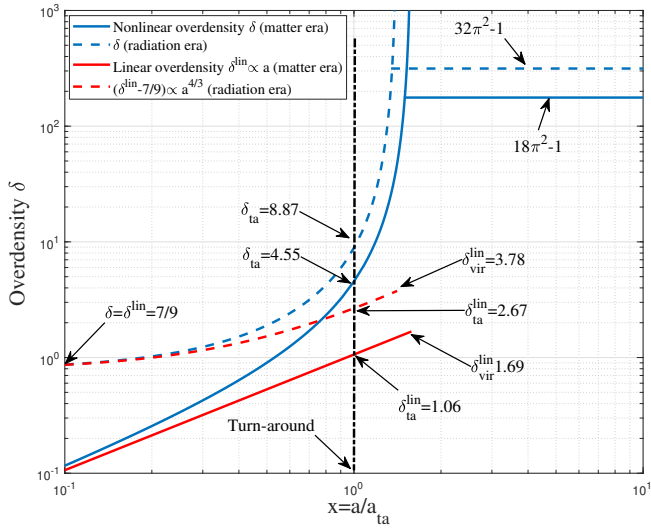


**Figure 3.** The evolution of overdensity (relative to the total background density) with scale factor  $x$  from a spherical collapse model for matter era and radiation era, respectively. The solid blue line plots the overdensity evolution in matter era that starts from  $\delta = 0$  and reaches a maximum value of  $18\pi^2 - 1$ . The corresponding linear density evolves as  $\delta^{lin} \propto a$  (Eq. (30)). The dashed blue line plots the overdensity evolution in the radiation era that starts from a nonzero  $\delta = 7/9$  and reaches a maximum of  $32\pi^2 - 1$ . The corresponding linear overdensity evolves as  $(\delta^{lin} - 7/9) \propto a^{4/3}$  (Eq. (37)). In the radiation era, overdensity requires a high initial overdensity of  $7/9$  and grows into a nonlinear region much later than the same overdensity in the matter era.

In the radiation era, the density ratio  $\xi_{ta}$  at the turnaround can be obtained from Eqs. (21) and (23)

$$\tau_{ta} = \tau(x = 1) = 1/2 \quad \text{and} \quad \xi_{ta} = \pi^2 \approx 9.87. \quad (33)$$

The ratio between sphere density  $\rho(t)$ , turnaround density  $\rho_{ta}$ , and background density  $\bar{\rho} \propto a^{-4}$  are

$$\frac{\rho}{\rho_{ta}} = \frac{1}{y^3}, \quad \frac{\bar{\rho}}{\rho_{ta}} = \frac{1}{x^4}, \quad \frac{\rho/\bar{\rho}}{\rho_{ta}/\bar{\rho}_{ta}} = \frac{1 + \delta}{\xi_{ta}} = \frac{x^4}{y^3}. \quad (34)$$

The exact relation between  $y$  and  $x$  now becomes

$$y^3 = \pi^2 x^4 / (1 + \delta). \quad (35)$$

Taylor expansion of Eq. (22) leads to the linear approximation:

$$\frac{1}{2}x^2 \approx \frac{1}{\pi} \left( \frac{2}{3}y^{3/2} + \frac{1}{5}y^{5/2} \right). \quad (36)$$

Using Eq. (36) and Eq. (35), we obtain the evolution of the linear overdensity and the linear overdensity at the turnaround,

$$\delta^{lin} = \frac{7}{9} + \frac{3}{5} \left( \frac{4}{3} \right)^{\frac{4}{3}} \pi^{\frac{2}{3}} \left( \frac{a}{a_{ta}} \right)^{\frac{4}{3}}, \quad (37)$$

$$\delta_{ta}^{lin} = \frac{7}{9} + \frac{3}{5} \left( \frac{4}{3} \right)^{\frac{4}{3}} \pi^{\frac{2}{3}} \approx 2.67.$$

For an over-density that is fully collapsed at time  $t_{vir} = 2t_{ta}$  ( $t \propto a^2$  for radiation era) with  $R_{vir} = R_{ta}/2$ , the overdensity becomes

$$\frac{\rho_{vir}/\bar{\rho}_{vir}}{\rho_{ta}/\bar{\rho}_{ta}} = \frac{\xi_{vir}}{\xi_{ta}} = \frac{(2^{1/2})^4}{(1/2)^3}, \quad (38)$$

$$\xi_{vir} = 32\xi_{ta} = 32\pi^2,$$

$$\delta_{vir}^{lin} = \frac{7}{9} + \frac{3}{5} \left( \frac{4}{3} \right)^{\frac{4}{3}} \pi^{\frac{2}{3}} 2^{2/3} \approx 3.78.$$

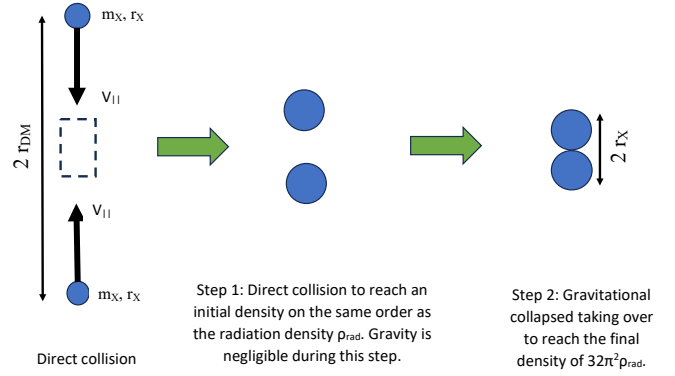


**Figure 4.** Two-step formation of nonlinear halo structures on small scales in the radiation era. Step 1: direct collision of two  $X$  particles of mass  $m_X$ , size  $r_X$  and a mean separation  $2r_{DM}$  to reach an initial overdensity on the same order as the radiation density  $\rho_{rad}$  (Fig. 3 and Eq. (37)). The gravity is relatively weak during this step. Step 2: the gravitational collapse starts to take over to reach the final density of  $32\pi^2\rho_{rad}$  (Fig. 3 and Eq. (38)).

Note that the density ratio  $\xi$  and the overdensity  $\delta$  in this section refer to the ratio of the sphere density to the background density (Eq. (17)). Figure 3 also presents the evolution of a linear overdensity  $\delta^{lin}$  in the radiation era that starts from an initial value  $\delta = 7/9$ , evolves as  $\delta - 7/9 \propto a^{4/3}$  in the linear regime (Eq. (37)), until it reaches a critical value of 2.67 at the turnaround (entering the nonlinear region), and a value of 3.78 for the fully collapsed overdensity. Compared with the evolution in the matter era, we found that:

- (i) Overdensity in the radiation era evolves into a nonlinear region much later than that in the matter era with higher linear overdensity at the turnaround ( $\delta_{ta}^{lin}$ ). Density ratio at turnaround  $\xi_{ta}$  and at virial equilibrium  $\xi_{vir}$  are also higher than those in the matter era.
- (ii) On small scales, the linear perturbation theory does not apply. Our solution suggests a linear overdensity  $\delta^{lin} \propto 7/9 + \text{Const} \cdot a^{4/3}$ .
- (iii) Since the universe expansion is extremely fast in the radiation era, if the gravitational collapse occurs, a special mechanism that does not involve gravity is required to give rise to the initial overdensity  $\delta = 7/9$  that is comparable to the density of the radiation background. The gravitational collapse can take over subsequently. In the next section, we discuss a possible mechanism via direct collisions.

#### 4 STRUCTURE FORMATION BY DIRECT COLLISIONS

In the radiation era, linear theory predicts a suppressed density perturbation on large scales due to fast expansion, i.e., the Meszaros effect. Perturbations on large scales are suppressed by the Hubble expansion. Therefore, large-scale structures smaller than the horizon ( $r_t < r < r_H$  in Fig. 1) remain essentially frozen as a result of radiation impeding growth. However, on small scales, nonlinear structure formation and evolution are still possible in the radiation era. In this section, we discuss halo structure formation on small scales in the radiation era, while structures on large scales are still suppressed.

We begin our discussion with Fig. 4. Consider a collection of  $X$  particles with mass  $m_X$ , size  $r_X$ , and a mean separation of  $2r_{DM}$ . The first step is direct collisions of dark matter particles to reach an initial matter density comparable to the radiation  $\rho_{rad}$ . Gravity is not involved during this step. The second step involves the gravitational collapse of the overdensity to form virialized haloes with a final density of  $32\pi^2\rho_{rad}$ , as described by the spherical collapse model. During the first step of direct collision, gravity is neglected, and we

focus on the collision time. For particles of size  $r_X$ , the cross-section is  $\sigma_d = \pi r_X^2$ . With the mean separation  $r_{DM} = (3m_X/4\pi\rho_{DM})^{1/3}$ , the mean free path  $\lambda_{DM}$  and the collision time  $\tau_{dc}$  are:

$$\lambda_{DM} = \frac{m_X}{\rho_{DM}\sigma_d} = \frac{4}{3} \left( \frac{r_{DM}}{r_X} \right)^2 r_{DM}, \quad (39)$$

$$\tau_{dc} = \frac{\lambda_{DM}}{V_{||}} = \frac{4}{3} \left( \frac{r_{DM}}{r_X} \right)^2 \frac{r_{DM}}{V_{||}}.$$

Obviously,  $\tau_{dc} \propto a^3$  rapidly increases with time due to the expansion  $r_{DM} \propto a$  for a fixed particle size  $r_X$  such that direct collision is only possible in radiation era. To calculate the time scale  $\tau_{dc}$ , we need to determine the velocity  $V_{||}$  and size  $r_X$ , respectively.

The peculiar velocity of the particle can be decomposed into a parallel component  $V_{||}$  due to the gravity of density perturbations on large scales and a perpendicular component  $V_{\perp}$  not induced by gravity. For the perpendicular component, the comoving velocity  $\mathbf{u}_{\perp} = V_{\perp}/a$  satisfies  $\dot{\mathbf{u}}_{\perp} + 2H\mathbf{u}_{\perp} = 0$ , so it decreases rapidly as  $\mathbf{u}_{\perp} \propto a^{-2}$  and  $V_{\perp} \propto a^{-1}$ . This is the thermal velocity that contributes to the vorticity and decreases rapidly over time compared to  $V_{||}$  (Fig. 5). Therefore, it is generally a good approximation to treat the large-scale velocity as being curl-free with vanishing vorticity [36]. For direct collisions, we need to compute  $V_{||}$  in the radiation era.

The parallel component of the comoving velocity  $\mathbf{u}_{||} = V_{||}/a$  is coupled to the density perturbations  $\delta$  in dark matter. The linearized perturbation equations reads

$$\dot{\delta} + \nabla \cdot \mathbf{u}_{||} = 0, \quad (\text{continuity equation})$$

$$\dot{\mathbf{u}}_{||} + 2H\mathbf{u}_{||} = -\frac{1}{a^2} \nabla \delta \Phi, \quad (\text{momentum conservation}) \quad (40)$$

$$\nabla^2 \delta \Phi = 4\pi G \rho_{DM} a^2 \delta. \quad (\text{Poisson equation})$$

The parallel component can be further expressed as the gradient of potential perturbation  $\delta \Phi$ , i.e.  $\mathbf{u}_{||} \propto -\nabla \delta \Phi$ . From Eq. (40), equations for perturbation  $\delta$  and comoving velocity  $\mathbf{u}_{||}$  are obtained as

$$\ddot{\delta} + 2H\dot{\delta} = 4\pi G \rho_{DM} \delta, \quad (41)$$

$$\dot{\mathbf{u}}_{||} + 2H\mathbf{u}_{||} = 4\pi G \rho_{DM} \frac{\delta}{\delta} \mathbf{u}_{||}.$$

This equation is valid in both radiation and matter eras, where the Hubble parameter satisfies

$$H^2 = \frac{8}{3} \pi G \rho_{DM} \left( 1 + \frac{a_{eq}}{a} \right), \quad \dot{H} = -\frac{H^2}{2} \frac{3 + 4a_{eq}/a}{1 + a_{eq}/a}. \quad (42)$$

If the gravity is neglected (right-hand-side term in Eq. (41)), we found the logarithmic growth for density perturbation  $\delta \propto \ln t$  in the radiation era. For both radiation and matter eras, the well-known exact solution for  $\delta$  considering the gravity reads [37]

$$\delta = 2B/3 + B(a/a_{eq}), \quad (43)$$

where  $B$  is a constant. We, therefore, find that in the radiation era with  $a \ll a_{eq}$ , the dark matter perturbations do not grow in the linear regime, i.e., the Meszaros effect. In the matter era with  $a \gg a_{eq}$ , linear perturbations grow as  $\propto a$ . Substitute this solution into the equation for  $\mathbf{u}_{||}$  in Eq. (41), we obtain an exact solution for  $\mathbf{u}_{||}$

$$\mathbf{u}_{||}^2 = C(1/a + 1/a_{eq})/a, \quad (44)$$

$$V_{||}^2 = \mathbf{u}_{||}^2 a^2 = C(1 + a/a_{eq}),$$

where  $C$  is a constant. Therefore, on large scales, there exists a nonzero constant velocity dispersion  $V_{||}^2 = C$  associated with the

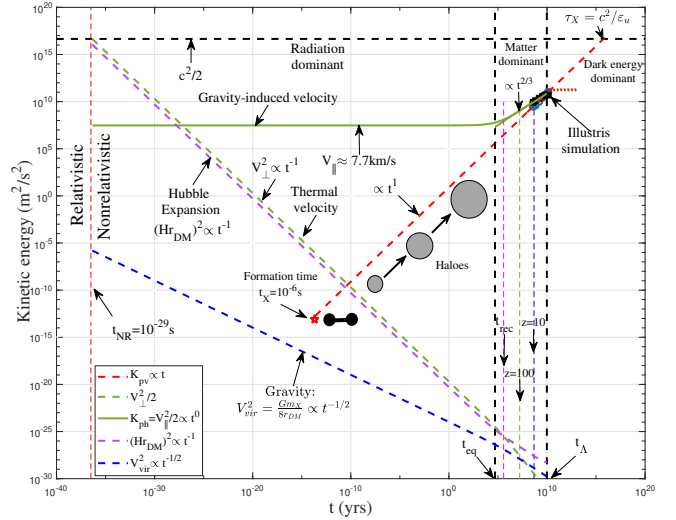


**Figure 5.** The evolution of kinetic energy of different velocities in the radiation era for  $X$  particles with a critical mass of  $m_{Xc} = 10^{12} \text{ GeV}$ . The effect of gravity is weak in the radiation era such that the virial velocity  $V_{vir}$  is much smaller than other velocities (dashed blue). The perpendicular component  $V_{\perp}$  (thermal velocity) and  $V_H$  (due to expansion) decreases rapidly with time (Eq. (45)). The large-scale parallel velocity  $K_{ph} = V_{||}^2/2$  is due to gravity on large scales and is independent of particle mass and time. Direct collision due to velocity  $V_{||}$  leads to the formation of the smallest two-particle halo at around  $10^{-6} \text{ s}$  (red star from Eq. (55)) and halo evolution in the radiation era (Section 5). The kinetic energy  $K_{pv} \propto t$  on small scales ( $< m_h^*$ ) is due to the virialization in haloes and plotted as a red dashed line (Eqs. (108) and (109)). The nature of  $K_{ph}$  and  $K_{pv}$  on large and small scales is discussed in Fig. 16. The evolution of kinetic energy in the matter era (symbols from Illustris simulation) is discussed in Fig. 22.

frozen density perturbations  $\delta$  in the radiation era. This gravity-induced velocity  $V_{||}$  leads to the direct collision of dark matter particles in the early universe. In the matter era, the velocity dispersion  $V_{||}^2 \propto a$  increases with time from Eq. (44). With  $V_{||}$  on the order of 450 km/s at the current epoch ( $a = 1$  from the Illustris simulations in Fig. 22), we estimate the constant  $C = 6 \times 10^7 \text{ m}^2/\text{s}^2$  such that  $V_{||} \approx 7.7 \text{ km/s}$  in the radiation era. The velocity  $V_{||}$  is independent of the particle mass  $m_X$  and time  $t$  (Fig. 5) and should also be independent of the exact model of dark matter particles.

For comparison, we also calculated the perpendicular velocity  $V_{\perp}$ , Hubble flow  $V_H$ , and virial velocity  $V_{vir}$  due to gravity,

$$V_{\perp} = \frac{a_{NR}}{a} c = \frac{3k_B T_{\gamma 0}}{cm_X} a^{-1} \propto m_X^{-1} a^{-1},$$

$$V_H = Hr_{DM} \propto m_X^{1/3} a^{-1}, \quad (45)$$

$$V_{vir}^2 = \frac{Gm_X}{8r_{DM}} \propto m_X^{2/3} a^{-1}.$$

All of these velocities depend on both particle mass and time. Figure 5 plots the variation of different velocities in the radiation era for  $X$  particles with a critical mass  $m_{Xc} = 10^{12} \text{ GeV}$ . The virial velocity  $V_{vir}$  due to gravity is small in the radiation era when compared to the Hubble flow from expansion. The parallel peculiar velocity on large scales ( $V_{||}$ ) is constant and independent of the particle mass  $m_X$  (solid green line). Direct collisions due to velocity  $V_{||}$  led to the formation of the first non-linear structure (red star) and the evolution of structures in the radiation era. The kinetic energy on small scales increases linearly with time  $K_{pv} \propto t$  due to the virialization in the haloes (red dashed line) (Eqs. (108) and (109)).

Next, we estimate the size of the particles  $r_X$  for a given particle mass  $m_X$ . Here, we consider the smallest halo structure with only two X particles. This is possible for particles with mass  $m_X \geq m_{Xc}$  such that the free streaming mass  $M_{fs}$  is smaller than the particle mass  $m_X$  (Fig. 2). For particles with mass  $m_X < m_{Xc}$ , the free streaming mass is greater than the particle mass. The size and formation time of the smallest structure is determined by the free streaming mass  $M_{fs}$ . This is discussed separately in Section 12 (Table 3).

Now consider the smallest haloes with two X particles of mass  $m_X$  and separation  $l_X$ , formed in virial equilibrium at time  $t_X$ ,

$$2v_X^2 = \frac{Gm_X}{l_X}, \rho_X = \frac{2m_X}{\frac{4}{3}\pi l_X^3} = \xi \bar{\rho}(t_X), H(t_X)^2 = \frac{8}{3}\pi G \bar{\rho}(t_X), \quad (46)$$

where  $\bar{\rho}(t_X)$  is the background density at the formation time  $t_X$ ,  $v_X$  is the virial velocity. According to the spherical collapse model, at the formation time  $t_X$ , the density of the smallest structure should be  $\rho_X(t_X) = \xi \bar{\rho}(t_X)$ . For the radiation era and the matter era, the density ratio  $\xi = 32\pi^2$  or  $18\pi^2$ , respectively. The formation time  $t_X$  can be obtained from Eq. (46) as

$$t_X = \pi \frac{l_X}{v_X}. \quad (47)$$

Next, we consider the smallest possible  $t_X$ , i.e., the earliest time the two-particle haloes can form. The density of the smallest structure ( $\rho_X$  of two-particle haloes) at the earliest time of formation (the smallest  $t_X$ ) should be the highest density that these structures can have. According to the "uncertainty principle," the two X particles cannot collapse to an infinite density, and there exists a maximum density due to the quantum pressure. For fermion dark matter, the degeneracy pressure from the uncertainty principle should balance the gravitational pressure. Therefore, we have

$$m_X v_X \cdot r_X = n\hbar, \quad (48)$$

where  $\hbar$  is Planck constant and  $n$  is the quantum number with  $n = 1$  for the ground state. Similarly, as electrons cannot be fully pulled into the nucleus due to the uncertainty principle, two X particles cannot be fully pulled into each other by gravity for the same reason, i.e., the size  $r_X = l_X/2$  cannot be zero. Therefore, the momentum  $m_X v_X$  and the position  $r_X$  should satisfy the uncertainty principle in Eq. (48). Combined with Eq. (46) for virial theorem, the particle size and the virial velocity are

$$r_X = l_X/2 = \frac{4\hbar^2}{G(m_X)^2} \quad \text{and} \quad v_X = \frac{G(m_X)^2}{4\hbar}. \quad (49)$$

The earliest formation time  $t_X$  that gives the highest density and also the right ratio ( $\xi = 32\pi^2$  for the radiation era) is (from Eq. (47))

$$t_X(m_X) = \pi \frac{l_X}{v_X} = \frac{32\pi\hbar^3}{G^2(m_X)^5} \quad \text{for} \quad m_X \geq m_{Xc} = 10^{12} \text{ GeV}. \quad (50)$$

This equation is only valid for particles with a mass greater than the critical mass  $m_{Xc}$  such that the free streaming mass is smaller than the particle mass to allow the formation of two-particle haloes. For particles with a mass smaller than  $m_{Xc}$ , the free streaming mass can be much greater than the particle mass (Fig. 2) such that the smallest structure (haloes) formed by these particles is much larger than particles themselves. For example, the smallest halo formed by WIMPs is around  $10^{-6} M_\odot$ , which is much larger than WIMPs. Therefore, WIMPs cannot form two-particle haloes (Table 3).

The formation time  $t_X$  strongly decreases with particle mass  $m_X$ . Heavier particles (larger  $m_X$ ) should form smaller structures (smaller  $r_X$ ) at an earlier time (smaller  $t_X$ ). However, this formation time  $t_X$  should also be comparable to the direct collision time scale  $\tau_{dc}$  to

allow a sufficient amount of time for direct collisions to occur to form these structures. With particle size  $r_X$  in Eq. (84) and velocity  $V_{||}$  in Eq. (44), we are able to calculate the direct collision time scale  $\tau_{dc}$  in Eq. (39) at the time of formation  $t_X$ ,

$$\tau_{dc}(m_X, t_X) = \frac{4}{3} \left( \frac{r_{DM}}{r_X} \right)^2 \frac{r_{DM}}{V_{||}}. \quad (51)$$

With all relevant quantities,

$$\begin{aligned} r_{DM}(m_X, t_X) &= \left( \frac{3m_X}{4\pi\rho_{DM}} \right)^{1/3}, \quad r_X(m_X) = \frac{4\hbar^2}{G(m_X)^3}, \\ \rho_{DM}(m_X, t_X) &= \frac{3H_0^2}{8\pi G} \Omega_{DM} a_X^{-3}, \quad t_X = \frac{a_X^2}{2H_0\sqrt{\Omega_{rad}}}. \end{aligned} \quad (52)$$

The direct collision time scale  $\tau_{dc}$  can be computed as a function of particle mass  $m_X$ ,

$$\tau_{dc}(m_X) = \frac{2^8 \pi^{3/2}}{3} \left( \frac{\Omega_{rad}^{3/2}}{H_0 \Omega_{DM}^2} \right)^{1/2} \left( \frac{\hbar}{m_X V_{||}^2} \right)^{1/2}, \quad (53)$$

With the formation time comparable to the direct collision time or  $t_X(m_X) = \tau_{dc}(m_X)$  (Eqs. (50) and (53)), the only possible particle mass  $m_X$  should read

$$m_X = \left( \frac{9}{64\pi} \frac{H_0 \Omega_{DM}^2}{\Omega_{rad}^{3/2}} \frac{V_{||}^2 \hbar^5}{G^4} \right)^{1/9} \approx 0.55 m_{Xc}. \quad (54)$$

Therefore, only for X particles with critical mass  $m_{Xc}$ , the direct collision time  $\tau_{dc}$  is comparable to the formation time  $t_X$ , which allows the formation of the smallest two-particle haloes in the radiation era. Particles heavier than  $m_{Xc}$  will have  $\tau_{dc} \gg t_X$  such that there is no sufficient time to form these structures. Particles lighter than  $m_{Xc}$  have  $\tau_{dc} \ll t_X$ , while the thermal velocity will prevent the formation of these two-particle haloes due to the free streaming mass greater than the particle mass (Fig. 2). Finally, only particles with a mass around  $m_{Xc}$  can form the smallest structure of two-particle haloes as described here. This is also the earliest possible structure that particles of any mass can form. The corresponding particle size, velocity, and time are as follows:

$$\begin{aligned} l_X = 2r_X &= \frac{8\hbar^2}{G(m_{Xc})^3} \approx 3 \times 10^{-13} \text{ m}, \\ v_X &= \frac{G(m_{Xc})^2}{4\hbar} \approx 4 \times 10^{-7} \text{ m/s}, \quad E_X = m_{Xc} v_X^2 = 10^{-9} \text{ eV}, \quad (55) \\ t_X &= \pi \frac{l_X}{v_X} = \frac{32\pi\hbar^3}{G^2(m_{Xc})^5} \approx 2 \times 10^{-6} \text{ s}. \end{aligned}$$

Therefore, the smallest structure formed by two X particles of mass  $m_{Xc} = 10^{12} \text{ GeV}$  has a size of  $10^{-13} \text{ m}$ , the velocity of  $10^{-7} \text{ m/s}$  and formed at around  $t = 10^{-6} \text{ s}$  or  $a \approx 2 \times 10^{-13}$  in the radiation era (red star in Fig. 5). We can also identify a critical energy scale  $E_X = 10^{-9} \text{ eV}$  that is the binding energy in the ground state, i.e., the amount of energy released when two X particles approach from infinity to form the smallest structure. We postulate that this is also the highest energy level (with quantum number  $n=1$  in Eq. (48)) of the dark radiation. The dark radiation, if exists, is produced during the formation of the earliest and smallest halo structures at the formation time  $10^{-6} \text{ s}$  (Section 15).

The key parameter  $\varepsilon_u$  that we introduced in Eq. (15) reads

$$\varepsilon_u = 2 \frac{v_X^3}{l_X} = \frac{G^4(m_{Xc}^9)}{256\hbar^5} \approx 4 \times 10^{-7} \text{ m}^2/\text{s}^3. \quad (56)$$



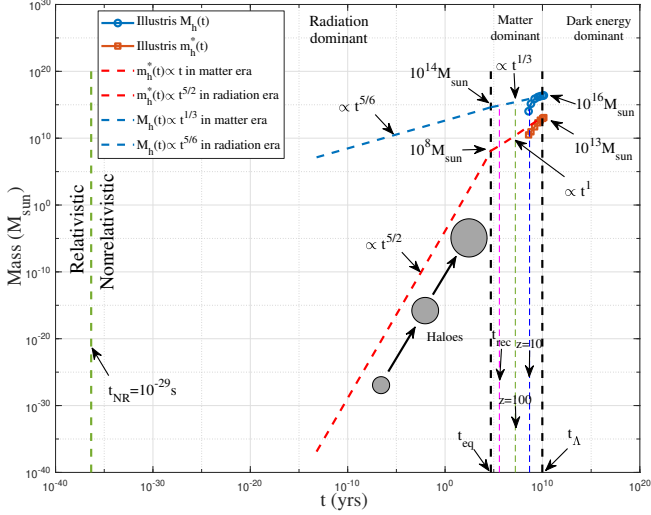


**Figure 6.** The evolution of the characteristic halo mass  $m_h^*(t)$  (red line) and total mass in all haloes  $M_h(t)$  (blue line) in the radiation and matter eras to match the blue and red symbols from Illustris simulations (Sections 7 to 11). Evolution in the matter era is also presented in Fig. 7. In the radiation era,  $m_h^* \propto t^{5/2}$  and  $M_h \propto t^{5/6}$ . The average waiting time between two successive merges decreases rapidly over time with  $\tau_g \propto t^{-3/2}$ . In the matter era,  $m_h^* \propto t^1$  and  $M_h \propto t^{1/3}$ , and a constant average waiting time  $\tau_g \approx 10^{-41} \text{ s} \approx 18\pi^2 t_P$ , where  $t_P = 5.4 \times 10^{-44} \text{ s}$  is the Planck time. Table 1 summarizes the evolution of structures in both eras. The halo mass  $m_h^*$  can reach around  $10^8 M_\odot$  at matter-radiation equality.

We now interpret the parameter  $\varepsilon_u$  as the rate of transfer of (specific) kinetic energy  $v_X^2$  in a turnaround time  $l_X/v_X$ . That kinetic energy is continuously transferred across haloes to larger and larger scales until the characteristic mass  $m_h^*$ , which determines the halo structure and dynamics (Fig. 12). The simulation and observational evidence involving the key parameter  $\varepsilon_u$  is discussed in Sections 7 to 11.

## 5 NONLINEAR HALO EVOLUTION IN RADIATION ERA

In the radiation era, density perturbations are suppressed on large scales (linear regime) greater than the characteristic mass  $m_h^*$ . On small scales (nonlinear regime) less than  $m_h^*$ , haloes can form by direct collision and gravitational collapse (Fig. 4). After the formation of the smallest two-particle haloes at  $t_X = 10^{-6} \text{ s}$ , the hierarchical structure formation takes over, and the characteristic halo mass  $m_h^*$  increases over time (Fig. 5). On small scales in the nonlinear regime, micro-haloes grow by merging with X particles to form larger and larger haloes. In this section, we discuss the evolution of nonlinear structures in the radiation era.

The hierarchical merging of structures is fundamental and complex. In a finite time interval  $\Delta t$ , hierarchical merging could involve multiple substructures merging into a single large structure. However, for an infinitesimal interval  $\Delta t \rightarrow 0$ , the most frequent merging should involve a single X particle and a halo, an elementary and fundamental step for hierarchical structure formation (two-body collapse [38]). Similarly to the formation of two-particle haloes, halo evolution in the radiation era involves a direct collision with a cross-section  $\sigma_d = \pi r_h^2$  that depends on the halo mass  $r_h \propto m_h^{1/3}$ . We consider the average waiting time  $\tau_g$  as the time between two successive merges between the halo and the particles. This waiting time

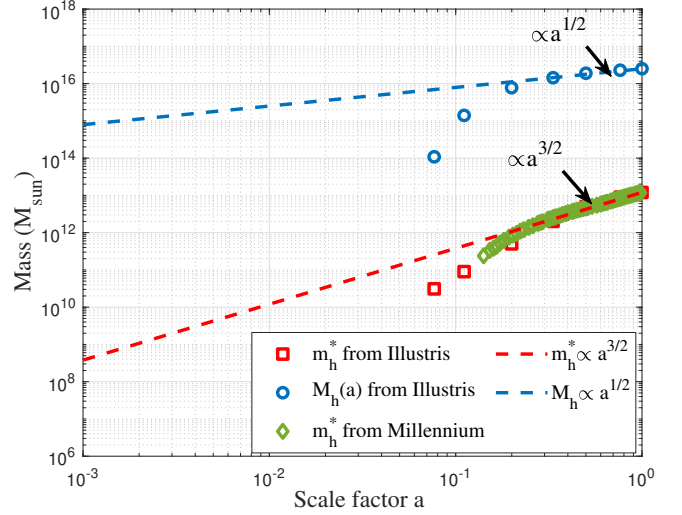


**Figure 7.** The evolution of the characteristic halo mass  $m_h^*(t)$  (red dashed) and total halo mass  $M_h$  (blue dashed) in the matter era, where  $m_h^* \propto a^{3/2} \propto t$  and  $M_h \propto a^{1/2} \propto t^{1/3}$ . Results from different cosmological N-body simulations (symbols) are also presented that are in agreement with the prediction of Eq. (61). The deviation at high redshift can be due to the limited mass resolution in N-body simulations.

is just the direct collision time in the radiation era ( $\tau_g \equiv \tau_{dc}$ ),

$$\tau_g = \tau_{dc} = \frac{4}{3} \left( \frac{r_{DM}}{r_h} \right)^2 \frac{r_{DM}}{V_{||}} \propto m_h^{-\lambda}, \quad (57)$$

where  $r_{DM} \propto a$  is the mean separation and  $\lambda = 2/3$  is a halo geometry parameter because of  $r_h \propto m_h^{1/3}$ . After every merge with a single particle, the halo mass increases by the particle mass  $m_X$ . Therefore, the evolution of the halo mass  $m_h$  and  $m_h^*$  now reads

$$\frac{dm_h}{dt} = \frac{m_X}{\tau_g} \quad \text{and} \quad \frac{dm_h^*}{dt} = \frac{m_h^*}{t} = \frac{m_X}{\tau_g^*}. \quad (58)$$

Since haloes should have a constant density ratio to the background density ( $32\pi^2$  from the spherical collapse model), we have

$$\rho_h = \frac{m_h}{\frac{4}{3}\pi r_h^3} = 32\pi^2 \rho_{rad} \propto a^{-4}. \quad (59)$$

Solving these equations leads to the scaling

$$\tau_g \propto m_h^{-2/3} a^{1/3} \quad \text{and} \quad r_h \propto m_h^{1/3} a^{4/3}. \quad (60)$$

For haloes with the characteristic mass  $m_h^*$  and size  $r_h^*$ , we have the scaling  $r_h^* \propto a^3 \propto t^{3/2}$ ,  $m_h^* \propto a^5 \propto t^{5/2}$  using Eqs. (58) and (60). The average waiting time for haloes of mass  $m_h^*$  follows  $\tau_g^* \propto a^{-3} \propto t^{-3/2}$ . The waiting time due to direct collision rapidly decreases due to the fast growth of the halo size  $r_h^*$  and the rapid increase in the cross-section. In addition, the total mass  $M_h(t)$  of dark matter contained in all haloes also increases with time. With the geometry parameter  $\lambda = 2/3$ , the total halo mass is  $M_h \propto m_h^{1-\lambda}$  [39] such that  $M_h \propto a^{5/3} \propto t^{5/6}$ .

For comparison, structure evolution in the matter era is dominated by gravity. The waiting time  $\tau_g$  is inversely proportional to the halo potential  $\tau_g \propto (Gm_h/r_h)^{-1}$  [39, 40]. To understand this, we consider a particle to merge with a halo of mass  $m_h$  and size  $r_h$ . The local velocity dispersion  $\sigma^2$  of that particle (or the local temperature  $T$ ) depends on the local gravitational potential, i.e.,  $T \propto \sigma^2 \propto Gm_h/r_h$ .

The probability  $P$  for a successful merge is  $P \propto e^{-1/T}$ . Therefore, the waiting time  $\tau_g \propto 1 - P \propto 1/T$  for high temperature  $T$ . A larger halo with higher potential means higher temperature and shorter waiting time  $\tau_g \propto T^{-1}$ . Larger haloes accrete mass more quickly with a shorter waiting time, where  $\tau_g \propto m_h^{-2/3}$  with  $r_h \propto m_h^{1/3}$  [39, 40]. Haloes of characteristic mass  $m_h^*$  have the shortest waiting time  $\tau_g^*$ .

Therefore, corresponding equations in the matter era are

$$\begin{aligned} \frac{dm_h}{dt} &= \frac{t_0}{10^{13}M_\odot} = \frac{m_X}{\tau_g}, \\ \tau_g &\propto (Gm_h/r_h)^{-1}, \\ \rho_h &= \frac{m_h}{\frac{4}{3}\pi r_h^3} = 18\pi^2 \rho_{DM} \propto a^{-3}. \end{aligned} \quad (61)$$

Solving these equations leads to the scalings in the matter era:

$$\tau_g \propto m_h^{-2/3} a \quad \text{and} \quad r_h \propto m_h^{1/3} a. \quad (62)$$

For haloes with the characteristic mass  $m_h^*$  and size  $r_h^*$ , we have the scaling  $r_h^* \propto t$ ,  $m_h^* \propto t$ , and the constant waiting time  $\tau_g^* \propto t^0$  in the matter era. The total mass in all haloes  $M_h \propto m_h^{*1/3} \propto t^{1/3}$ .

Table 1 summarizes the evolution of mass and energy in both the radiation and matter eras. Figure 6 presents the evolution of the characteristic halo mass  $m_h^*$  and the total halo mass  $M_h$  in both eras, while Fig. 7 presents the particular evolution in the matter era. Different cosmological N-body simulations confirm the evolution of the halo mass as predicted by Eq. (61). The characteristic halo mass  $m_h^* \propto t$  and the total halo mass  $M_h^* \propto t^{1/3}$  in the matter era. With  $m_h^*(z=0) \approx 10^{13}M_\odot$  and  $M_h(z=0) \approx 10^{16}M_\odot$  from Illustris simulation, the evolution of  $m_h^*$  and  $M_h$  can be fully determined for the radiation (left equations) and matter (right equations) eras as

$$\begin{aligned} m_h^* &= m_h^*(t_{eq}) \left( \frac{t}{t_{eq}} \right)^{5/2} \quad \text{and} \quad m_h^* = m_h^*(t_{eq}) \left( \frac{t}{t_{eq}} \right), \\ M_h &= M_h(t_{eq}) \left( \frac{t}{t_{eq}} \right)^{5/6} \quad \text{and} \quad M_h = M_h(t_{eq}) \left( \frac{t}{t_{eq}} \right)^{1/3}, \end{aligned} \quad (63)$$

where the characteristic halo mass and total halo mass at matter-radiation equality are  $m_h^*(t_{eq}) = 5 \times 10^7 M_\odot$  and  $M_h(t_{eq}) = 4.3 \times 10^{14} M_\odot$ , respectively, where  $t_{eq} = 50000$  yrs.

Using Eq. (58), the waiting time  $\tau_g^*$  for characteristic haloes is:

$$\begin{aligned} \tau_g^* &= \tau_g^*(t_{eq}) (t/t_{eq})^{-3/2}, \quad (\text{radiation era}), \\ \tau_g^* &= \tau_g^*(t_{eq}) = \frac{m_X t_{eq}}{m_h^*(t_{eq})}, \quad (\text{matter era}). \end{aligned} \quad (64)$$

The average waiting time decreases rapidly in the radiation era ( $\tau_g \propto t^{-3/2}$ ) and reaches a constant value in the matter era due to characteristic mass  $m_h^* \propto t$  (Eq. (61)). That constant value is dependent on the particle mass  $m_X$ ,

$$\tau_g^*(t > t_{eq}) = \frac{m_X}{m_h^*(t)} t = \frac{m_X}{m_h^*(t=t_0)} t_0. \quad (65)$$

With present characteristic halo mass of  $10^{13}M_\odot$  and  $t_0$  of the age of the universe, for particles of critical mass  $m_X = m_{Xc} = 10^{12}\text{GeV}$ , the waiting time is (from Eq. (65))

$$\tau_g^* \approx 10^{-41} \text{s} \approx 18\pi^2 t_p, \quad (66)$$

where  $t_p = 5.4 \times 10^{-44} \text{s}$  is the Planck time. Here,  $\xi = 18\pi^2$  is the critical density ratio in the matter era. For fixed mass density of dark matter haloes, a higher density ratio  $\xi$  means a lower background matter density and, of course, a longer waiting time for X particles

**Table 1.** Structure evolution in the radiation era and matter era

Quantity	Symbol	Radiation era	Matter era
Time	$t$	$\propto a^2$	$\propto a^{3/2}$
Hubble parameter	$Ht$	$1/2$	$2/3$
Large-scale overdensity	$\delta$	$a^0$	$a^1$
Large-scale KE	$K_{ph}$	$\propto a^0$	$\propto a^1$
Small-scale KE	$K_{pv}$	$\propto t$	$\propto t$
Total mass in all haloes	$M_h$	$t^{5/6}$	$t^{1/3}$
Characteristic halo mass	$m_h^*$	$t^{5/2}$	$t$
Characteristic halo size	$r_h^*$	$t^{3/2}$	$t$
Halo waiting time	$\tau_g$	$\propto m_h^{-2/3} a^{1/3}$	$\propto m_h^{-2/3} a^1$

to merge with haloes. Therefore,  $\tau_g^*$  is expected to be proportional to the density ratio  $\xi$  [40]. Since the Planck time is the smallest unit of time for any physical processes, particles with a critical mass  $m_{Xc}$  have the shortest possible waiting time  $18\pi^2 t_p$  [40]. This is another feature of the critical particle mass  $m_{Xc} = 10^{12}\text{GeV}$ .

Since Eq. (65) is independent of the dark matter particle model, for matter era, we write the waiting time for any particle mass  $m_X$

$$\frac{\tau_g^*}{18\pi^2 t_p} = \frac{m_X}{m_{Xc}} \quad \text{and} \quad \tau_g^* \propto m_X, \quad (67)$$

where the waiting time in the matter era is proportional to the particle mass. For particles with a mass  $m_X \ll m_{Xc}$ , the waiting time  $\tau_g^*$  can be much shorter than the Planck time, which seems unfavorable. Or equivalently, there is not enough time for particles with mass  $m_X \ll m_{Xc}$  to form haloes of  $10^{13}M_\odot$  as observed in the current epoch unless different mechanisms exist to accelerate the mass accretion in the matter era for particles with a mass smaller than  $m_{Xc}$ . However, any faster super-linear halo mass evolution ( $m_h^*(t) \propto t^\alpha$  with  $\alpha > 1$ ) will contradict the results of the N-body simulations in Fig. 7.

Due to rapid growth in the radiation era, the characteristic halo mass  $m_h^*$  can reach around  $10^8 M_\odot$  at the matter-radiation equality. This suggests that the dark matter haloes can reach an immense size earlier than we expected, which might be helpful to explain the JWST's recent discovery of big and bright galaxies as early as  $z = 15$  [41]. Table 1 summarizes the evolution of halo structures in both eras. The evolution of kinetic energy on large-scale and small-scale is discussed in Section 10 and presented in Fig. 16.

Up to this point, we have discussed the formation and evolution of nonlinear halo structures in the radiation era (Sections 2 to 5). We identified a critical mass scale  $m_{Xc}$  on the order of  $10^{12}\text{GeV}$ . Dark matter particles seem to prefer to have a mass of that critical mass because i) particles of this mass lead to the smallest possible structure (Fig. 2); ii) particles of this mass have a direct collision time scale  $\tau_{dc}$  comparable to the formation time  $t_X$  to allow the formation of the smallest and earliest two-particle haloes (Eq. (54)); and iii) particles of this mass have the shortest possible waiting time  $\tau_g^*$  to allow the formation of haloes observed today as large as  $10^{13}M_\odot$  (Eq. (67)). In particular, the last point is that particles of this mass give rise to the appropriate key parameter  $\varepsilon_u$  (Eq. (56)) that influence the halo dynamics and density profiles that can be observed. In the following, we will focus on this point with N-body simulations and observational evidence.

## 6 MODIFIED WIMP MIRACLE INVOLVING GRAVITY

The standard WIMP miracle, which assumes gravity is negligible on all scales, predicts weak-scale dark matter particles with a mass of approximately 100 GeV. In this Section, we begin with a brief review

of the standard WIMP miracle, followed by a modified WIMP miracle involving gravity that leads to much heavier dark matter particles of  $10^{12}$  GeV. Again, this particle mass is consistent with the critical particle mass  $m_{Xc} = 10^{12}$  GeV obtained from the formation of the smallest structure on the free streaming scale (Fig. 2).

In the early Universe, WIMP particles are in thermal equilibrium and annihilate into standard model particles ( $X + X \rightleftharpoons SM + SM$ ) [42]. This process can be quantitatively described by the Boltzmann equation that governs the evolution of particle number density  $n$ :

$$\frac{dn}{dt} = -3Hn - \langle\sigma_W v\rangle (n^2 - n_{eq}^2), \quad (68)$$

where  $\langle\sigma_W v\rangle$  represents the thermally averaged cross-section of WIMP particles. The first term on the right-hand side of Eq. (68) accounts for the dilution from universe expansion. The  $n^2$  term arises from the annihilation of WIMP particles, while the  $n_{eq}^2$  term comes from the reverse process to produce WIMP particles.

Due to the expansion of the Universe, at some point, the dark matter particles become too diluted to find each other and annihilate. At that moment, dark matter particles freeze out with their comoving relic density approaching a constant. We define the freeze-out time when the interaction rate is comparable to expansion  $H$ ,

$$n_f \langle\sigma_W v\rangle \sim H_f, \quad n_f = \frac{\bar{\rho}_0 \Omega_{DM}}{m_W a_f^3}, \quad (69)$$

where the subscript  $f$  denotes the quantity at freeze-out. Here,  $m_W$  is the mass of the WIMP particle, and  $a_f$  is the scale factor.

Equation (69) requires the cross section to be (with Hubble parameter  $H_f \propto a_f^{-2} \propto T_{\gamma f}^2$ )

$$\langle\sigma_W v\rangle \sim \frac{H_f}{n_f} \sim \frac{m_W a_f^3 H_f}{\bar{\rho}_0 \Omega_{DM}} \sim \frac{m_W}{\bar{\rho}_0 \Omega_{DM}} \frac{T_{\gamma 0}}{T_{\gamma f}} \frac{(k_B T_{\gamma 0})^2}{\hbar c^2 M_{pl}}, \quad (70)$$

where  $T_{\gamma 0}$  and  $T_{\gamma f}$  are the radiation temperature at present and freeze-out, respectively. Rearranging Eq. (70) leads to

$$\langle\sigma_W v\rangle \sim \underbrace{\frac{k_B T_{\gamma 0}}{c^2 M_{pl}}}_{1} \cdot x_f \cdot \underbrace{\frac{k_B T_{\gamma 0}}{c^2 \bar{\rho}_0 \Omega_{DM}} \cdot \frac{k_B T_{\gamma 0}}{\hbar}}_{2}, \quad (71)$$

$$x_f = \frac{m_W c^2}{k_B T_{\gamma f}} \approx 20,$$

where  $x_f$  is a dimensionless constant on the order of 20 [42]. WIMPs have a speed close to the speed of light before freeze-out. The equilibrium number density can be obtained by integrating the Boltzmann distribution over all possible momenta. The particle energy  $E$  and equilibrium number density  $n_{eq}$  can be approximated as

$$E = m_W c^2 + \frac{p^2}{2m_W}, \quad (72)$$

$$n_{eq} \propto \int \frac{d^3 p}{(2\pi)^3} \exp\left(-\frac{E}{T}\right) = g \left(\frac{m_W T}{2\pi}\right)^{3/2} \exp\left(-\frac{m_W c^2}{k_B T}\right),$$

where  $g \approx 2$  is a numerical factor. The equilibrium density is exponentially suppressed  $n_{eq} \propto e^{-x_f}$ .

With CMB temperature  $T_{\gamma 0} = 2.7$  K and Planck mass  $M_{pl} = 2.2 \times 10^8$  kg, the first term on the right-hand side of Eq. (71) is dimensionless and on the order of  $10^{-32}$  that sets the magnitude of  $\langle\sigma_W v\rangle$ . With critical density  $\bar{\rho}_0 = 10^{-26}$  kg/m<sup>3</sup> and the relic DM density  $\Omega_{DM} = 0.24$ , the second term is of order unity and sets the unit of  $m^3/s$ . The cross section  $\langle\sigma_W v\rangle$  finally reads

$$\langle\sigma_W v\rangle \approx 3 \times 10^{-32} \frac{m^3}{s}. \quad (73)$$

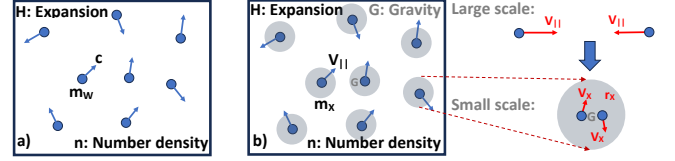


**Figure 8.** a) For the standard WIMP miracle, the gravitational interaction between dark matter particles is neglected on all scales. This is valid only for light particles (WIMPs, etc.) that become nonrelativistic much later with a speed close to  $c$  before freeze-out such that particle thermal velocity  $V_{\perp}$  is dominant over the gravity-induced velocity  $V_{\perp}$  at freeze-out; b) The modified WIMP miracle considers heavy particles involving gravity on both large and small scales. On large scales, these particles become nonrelativistic much earlier, with their thermal velocity  $V_{\perp}$  much smaller than the gravity-induced velocity  $V_{||}$  before freeze-out. On small scales, when two particles approach a scale comparable to the particle's size (de Broglie wavelength),  $r_X$ , both gravity and quantum effects can be important on that scale (Eq. (83)), leading to a different velocity,  $v_X \ll V_{||}$ . Figure 9 plots the difference in thermal history for WIMPs and heavy particles. Since velocity  $V_{||} \ll c$ , this difference in particle velocity before freeze-out enables a superheavy particle mass to evade the WIMPs' Unitarity bound.

This is the standard WIMP miracle: dark matter relic density requires a weak-scale cross section. In theory, for weak interaction, particle mass  $m_W$  determines the S-wave annihilation cross section

$$\langle\sigma_W v\rangle \propto \left(\frac{\hbar}{m_W c}\right)^2 \frac{g_w^4}{16\pi^2} c, \quad (74)$$

where  $g_w \approx 0.65$  is the weak interaction gauge coupling. For given cross section in Eq. (73), weak-scale particles of 100 GeV are an excellent candidate for dark matter.

However, the weak interaction and weak-scale particle mass may not be the only possible solution that satisfies the freeze-out condition (Eq. (69)). Since there is no fundamental theory that predicts the nature of particle interaction, the weak-scale WIMP particle might be just a coincidence. We should not exclude other possible interactions and masses that may also satisfy the same freeze-out condition (Eq. (69)). In the standard WIMP miracle (Fig. 8), the effect of gravity between dark matter particles is neglected on all scales. This assumption appears to be valid only i) on large scales, where the Universe is extremely homogeneous, and the impact of expansion exceeds that of gravity; 2) for relatively light particles (WIMPs, etc.) that become nonrelativistic much later with speed close to  $c$  before freeze-out (see  $x_f$  in Eq. (71)) such that thermal velocity is still dominant over the gravity-induced velocity  $V_{||}$  (Eq. (40)) at freeze-out. The "no gravity" assumption is valid in this scenario.

To relax this assumption, we need to consider much heavier particles that become nonrelativistic much earlier, with their speed far below the speed of light before freeze-out. For sufficiently heavier particles, the gravity-induced velocity  $V_{||}$  might be dominant over particle thermal velocity (Fig. 9). Both thermal velocity and gravity-induced velocity  $V_{||}$  can be well below the speed of light. For these heavy particles with velocity dominated by  $V_{||}$  on large scales, the particle energy can be approximated as the sum of contributions from  $V_{||}$  and thermal momentum  $p$ . The particle energy and the equilibrium number density read (different from WIMPs in Eq. (72))

$$E = \frac{1}{2} m_X V_{||}^2 + \frac{p^2}{2m}, \quad (75)$$

$$n_{eq} \propto \int \frac{d^3 p}{(2\pi)^3} \exp\left(-\frac{E}{T}\right) = g \left(\frac{m_X T}{2\pi}\right)^{3/2} \exp\left(-\frac{m_X V_{||}^2}{2k_B T}\right).$$

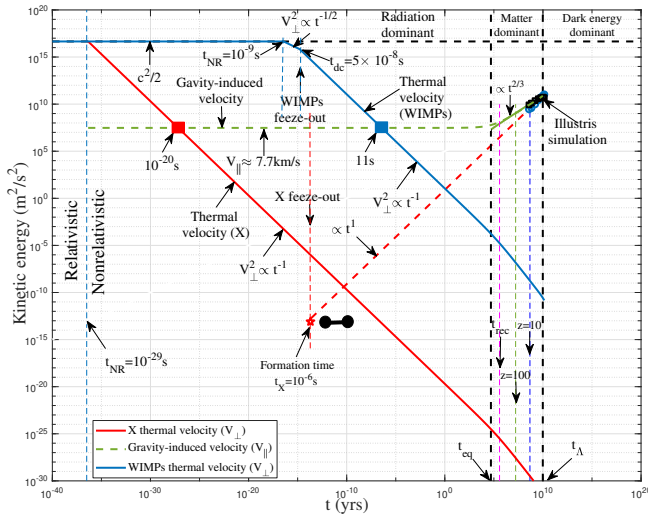


**Figure 9.** Different thermal history in the early Universe for WIMP particles (red) in the standard WIMP miracle and superheavy X particles (blue) in the modified WIMP miracle. WIMP particles of 100 GeV become nonrelativistic much later at  $10^{-9}$  s and are coupled to and in equilibrium with the thermal bath. They are decoupled and freeze out from the thermal bath at  $5 \times 10^{-8}$  s (temperature  $T_{\gamma f}$  of 4 GeV). WIMP particles have a speed close to the speed of light  $c$  before freeze-out, which is still dominated by their thermal velocity. Their speed becomes dominated by the gravity-induced velocity  $V_{||}$  of several km/s much later, only after 11 s (blue square). For comparison, superheavy X particles of  $10^{12}$  GeV become nonrelativistic much earlier at  $10^{-29}$  s, and remain decoupled because of their lower number density and gravitational interaction. Their speed becomes dominated by the gravity-induced velocity  $V_{||}$  at  $10^{-20}$  s (red square), much earlier than WIMPs. X particles remain decoupled at this low velocity until a time  $t_{Xeq}$  when they obtain equilibrium number density  $n_{eq}$ . Figure 11 plots the density evolution of WIMPs and X particles. These particles freeze out at  $10^{-6}$  s (temperature  $T_{\gamma f}^X$  of 0.5 GeV) and form the smallest bound structure (red star).

In this scenario, the dimensionless parameter  $x_f$  is defined in terms of the velocity  $V_{||}$  with a value similar to that of WIMPs:

$$x_f = \frac{m_X V_{||}^2}{2k_B T_{\gamma f}^X} = \frac{m_W c^2}{k_B T_{\gamma f}} \quad \text{and} \quad \frac{m_X T_{\gamma f}}{m_W T_{\gamma f}^X} = \frac{2c^2}{V_{||}^2}, \quad (76)$$

where  $T_{\gamma f}^X$  is the temperature at freeze-out of X particles. If the two temperatures are on the same order,  $T_{\gamma f}^X \sim T_{\gamma f}$ , the superheavy particles should have a mass  $m_X \approx 10^{10} m_W = 10^{12}$  GeV.

Next, we will provide a more rigorous consideration. Following the same requirement at freeze-out (Eq. (69)), i.e., the interaction rate is comparable to the expansion at freeze-out,

$$\langle \sigma_X v \rangle \sim \frac{m_X}{\bar{\rho}_0 \Omega_{DM}} \frac{T_{\gamma 0}}{T_{\gamma f}^X} \frac{(k_B T_{\gamma 0})^2}{\hbar c^2 M_{pl}}, \quad (77)$$

Using Eq. (76) and rearranging Eq. (77) leads to the relation between cross section for superheavy X particles and the standard WIMP miracle cross section

$$\langle \sigma_X v \rangle \sim \langle \sigma_W v \rangle \frac{2c^2}{V_{||}^2} \sim \langle \sigma_W v \rangle \frac{m_X T_{\gamma f}}{m_W T_{\gamma f}^X}, \quad (78)$$

Since velocity  $V_{||}$  is on the order of km/s, the new cross section is

$$\langle \sigma_X v \rangle \sim 10^{10} \langle \sigma_W v \rangle \sim 3 \times 10^{-22} \frac{m^3}{s}, \quad (79)$$

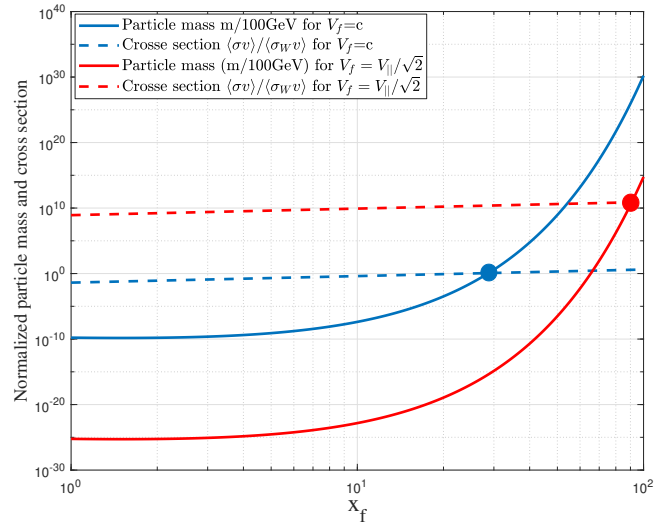


**Figure 10.** Particle mass and cross section varying with parameter  $x_f$  for two scenarios from solution (82): i) light particles (blue) with particle speed  $V_f = c$  dominated by the thermal velocity before freeze out; and ii) heavy particles (red) with particle speed  $V_f = V_{||}/\sqrt{2}$  dominated by the gravity-induced speed. Both mass and cross section are normalized by WIMP mass and cross section (blue circle), respectively. The red circle plots the mass and cross section of superheavy X particles  $10^{12}$  GeV. As expected, the cross section is relatively independent of  $x_f$ , while particle mass  $m$  is exponentially dependent on  $x_f$ . The cross sections for light particles and heavy particles are predicted in Eqs. (73) and (79). Exact particle mass can only be obtained by considering appropriate particle interactions.

Based on previous analysis, we provide a unified formulation and solution for the WIMPs miracle for both light and heavy particles. For any particle with a mass  $m$  and a speed  $V_f$  right before freeze-out, the equilibrium density reads

$$n_{eq} = g \left( \frac{mk_B T}{2\pi \hbar^2} \right)^{3/2} \exp(-x) \quad \text{and} \quad x = \frac{mV_f^2}{k_B T}. \quad (80)$$

By solvent equation (interaction rate comparable to the expansion),

$$n_{eq} = \frac{H_f}{\langle \sigma v \rangle} = \frac{\bar{\rho}_0 \Omega_{DM}}{ma^3}. \quad (81)$$

complete solutions of particle mass and cross section are

$$m = x_f^{-3/2} \exp(x_f) \frac{(2\pi)^{3/2}}{g} \left( \frac{\hbar V_f}{k_B T_{\gamma 0}} \right)^3 \bar{\rho}_0 \Omega_{DM}, \quad (82)$$

$$\langle \sigma v \rangle = \frac{(k_B T_{\gamma 0})^3 x_f}{c^2 V_f^2 \hbar M_{pl} \bar{\rho}_0 \Omega_{DM}}.$$

Figure 10 plots the respective solution for two scenarios. For particle speed dominated by the thermal speed,  $V_f = c$ , the standard WIMP miracle can be recovered for light particles like WIMPs. For particle speed dominated by the gravity-induced velocity,  $V_f = V_{||}/\sqrt{2}$ , the modified WIMP miracle can be recovered for heavy particles, where both mass and cross section depend on the gravity-induced velocity  $V_{||}$  of several km/s.

Respective cross sections are determined for two scenarios in Fig. 10. To determine the WIMPs particle mass, we assume the weak interaction between particles and the corresponding cross section in Eq. (74). Similarly, to determine the X particle mass, we need to introduce particle interaction and calculate the mass dependence of



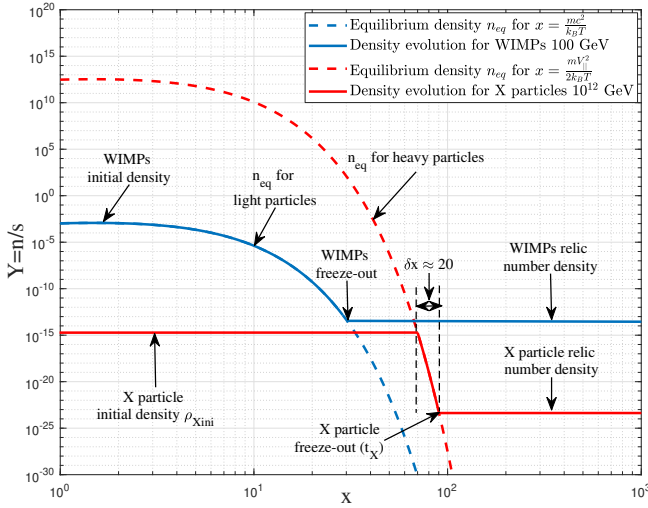


**Figure 11.** The evolution of particle number density (normalized by entropy density  $s$ ) with parameter  $x$  (or time) for WIMPs (blue) and superheavy X particles (red). WIMP particles are in equilibrium with the thermal bath. Their density follows the equilibrium density before freeze-out and reaches a constant relic density after freeze-out. Superheavy X particles with an initial density  $\rho_{Xini}$  remain decoupled and not in equilibrium with the thermal bath before the decoupling time  $t_X$ . This is because the effect of expansion is dominant over the gravitational interactions to prevent structure formation and particle annihilation. After time  $t_X$ , X particles become too dilute to find each other, and their density reaches a relic density.

cross section. Gravity is the most natural interaction between X particles on scales larger than particle size. When two heavy particles approach a scale comparable to the particle size (de Broglie wavelength  $r_X$ ), matter density is no longer homogeneous on that scale. The gravity and quantum effects may be sufficiently significant to impact the calculation (Fig. 8). On the particle size scale, we consider two equations based on the virial equilibrium and the balance between gravitational and quantum pressure:

$$2v_X^2 = \frac{Gm_X}{2r_X} \quad \text{and} \quad m_X v_X \cdot r_X = \hbar, \quad (83)$$

The particle size and velocity can be obtained from Eq. (83):

$$r_X = \frac{4\hbar^2}{G(m_X)^3} \quad \text{and} \quad v_X = \frac{G(m_X)^2}{4\hbar}. \quad (84)$$

This formulation assumes the gravitational interaction is the only particle interaction on all scales  $r \geq r_X$ , resulting in different velocities on large and small scales. On large scales, velocity  $V_{||}$  is of several km/s that is induced by gravity from large-scale density fluctuations (Eq. (41)). The small-scale velocity  $v_X$  is a result of gravity and quantum effect on the particle scale  $r_X$  (Eq. (84)).

The cross section for gravitational interaction should be  $\langle \sigma_X v \rangle = \pi r_X^2 V_{||}$ . Substituting Eq. (84) for  $r_X$  and Eq. (78) for  $\langle \sigma_X v \rangle$ , the particle mass can be obtained

$$m_X = \left( \frac{16\pi\hbar^4 V_{||}^3}{G^2 c^2 \langle \sigma_W v \rangle} \right)^{1/6} \approx 10^{12} \text{ GeV}, \quad (85)$$

which is in a surprising coincidence with the critical particle mass  $m_{Xc}$  obtained from the free streaming calculation in Section 2.

With this mass, the particle size  $r_X \approx 10^{-13} \text{ m}$  and the velocity  $v_X \approx 10^{-7} \text{ m/s}$  (Eq. (??)). Fig. 11 presents the evolution of particle number density  $n$  with parameter  $x$  (or equivalently time). The

number density was normalized by the entropy density  $s \propto a^3$

$$s = \frac{2\pi^2}{45} g_* T^3 \quad (g_* \approx 100). \quad (86)$$

For WIMP particles in equilibrium with the thermal bath, their density tracks the equilibrium density before freeze-out and reaches a constant relic density after freeze-out with  $x > x_f \approx 20$ . For superheavy X particles with an initial density  $\rho_{Xini}$ , these particles are not in equilibrium with the thermal bath before freeze-out. Different from WIMPs, this is because the effect of expansion is dominant over the gravitational interaction on particle size scale to prevent structure formation and particle annihilation ( $H \gg v_X/r_X$ ). After time  $t_X$ , X particles become too dilute to find each other, and their density reaches a relic density. The transition period between an initial density  $\rho_{Xini}$  and freeze-out might be approximated by  $\delta x \approx 20$ , similar to that of WIMPs. The initial density can be estimated as  $\rho_{Xini} \approx \bar{\rho}_0 \Omega_{DM} \cdot \exp(x)$ .

For X particle mass of  $m_X = 10^{12} \text{ GeV}$ , we can confirm that the same cross section (Eq. (73)) such that

$$m_W V_{||} = m_X v_X$$

$$\langle \sigma_X v_X \rangle = \pi r_X^2 v_X = \pi \left( \frac{\hbar}{m_X v_X} \right)^2 v_X = \frac{4\pi\hbar^3}{Gm_X^4} = \langle \sigma_W v \rangle. \quad (87)$$

Finally, due to the Boltzmann suppression, the number density of X particles after freeze-out should decrease exponentially to a level  $\propto \exp(-\delta x) \approx 10^{-9}$  of the initial number density  $\rho_{Xini}$ . For Majorana fermion dark matter, such as sterile neutrinos in Section 14, the annihilation of dark matter during freeze-out produces an equal number of SM and anti-SM particles, which subsequently annihilate into radiation. In this scenario, a substantial amount of radiation is expected to be produced when X particles freeze out (around  $t_X = 10^{-6} \text{ s}$ ). The fraction of radiation produced relative to the standard  $\Lambda\text{CDM}$  model reads

$$\delta_r = e^{\delta x} \frac{\Omega_{DM} a_X^{-3}}{\Omega_{rad} a_X^{-4}}, \quad \Delta N_{eff} = \frac{8}{7} \left( \frac{11}{4} \right)^{\frac{4}{3}} \delta_r \approx 0.4. \quad (88)$$

Depending on the exact value of parameter  $\delta x$  and scale factor at freeze-out  $a_X \approx 10^{-13}$ , this extra radiation corresponds to an increase in the relativistic degree of freedom parametrized by  $\Delta N_{eff} \approx 0.4$  for a fraction  $\delta_r$  of 5% of the total radiation. Extra radiation was proposed to alleviate disagreements about the current expansion rate  $H_0$  between  $\Lambda\text{CDM}$  prediction and direct measurements in the local universe, namely the Hubble tension [43, 44]. However, the amount of extra radiation in the early Universe is unavoidably constrained by BBN, CMB, and the large-scale structure of the Universe. Recent study shows that the Hubble tension can be ameliorated for  $0.2 \leq \Delta N_{eff} \leq 0.5$  [45]. With  $\Delta N_{eff} = 0.4$  in Eq. (88), the annihilation of superheavy dark matter at freeze-out may provide a possible mechanism to alleviate the Hubble tension problem. However, further study is still required to understand underlying annihilation mechanisms.

Similarly, we can also estimate the amount of radiation released due to the formation of the smallest bound structure at freeze-out (Section 15), which is much smaller compared to the extra radiation from dark matter annihilation. If axion exists as the radiation from structure formation, the axion fraction can be estimated as

$$\delta_a = \frac{\Omega_a}{\Omega_{DM}} = e^{\delta x} \frac{m_a}{m_X} \approx 10^{-21}. \quad (89)$$

In this scenario, the mass fraction of axion is significantly smaller than the fraction of dark matter. Here,  $m_a = 10^{-9} \text{ eV}$  is the mass of

radiation (Eq. (??)), and  $m_\chi = 10^{12}\text{GeV}$  is the mass of dark matter particles. This motivates probing the parameter space of axions at nano-eV masses at a much lower axion abundance than expected.

To summarize, the standard WIMP miracle yields a weak-scale particle of 100 GeV when gravity is neglected on all scales. The modified WIMP miracle, considering the effect of gravity, yields a superheavy particle of  $10^{12}\text{GeV}$ . This is consistent with the critical particle mass  $m_{\chi_c}$  that was obtained from the formation of the smallest structure on the free streaming scale (Section 2). The modified WIMP miracle supports a superheavy, thermal, and fermionic form of dark matter that can form the smallest two-particle bound structure and potentially annihilate into Standard Model (SM) particles due to the self-interaction on scales  $r < r_\chi$ . These superheavy dark matter particles become non-relativistic around  $t_{NR} = 10^{-29}\text{s}$ , followed by the particle freeze-out and the formation of the first structure. The exact formation time is governed by the competition between expansion  $H$ , interaction rate  $n\langle\sigma v\rangle$  ( $n$  is the particle number density), and collision frequency  $v_\chi/r_\chi$ . The collision frequency represents the minimum time required to form bound structures, which depends on the nature of the interaction between dark matter particles. Here,  $r_\chi$  and  $v_\chi$  represent the characteristic particle size and speed. The first structure can only be formed to enable subsequent annihilation when the expansion is slower with  $H < v_\chi/r_\chi$ .

For WIMPs involving weak interaction (much stronger than gravity), the collision frequency is on the order of  $10^{22}\text{Hz}$  with  $v_\chi=10\text{km/s}$  and  $r_\chi = 10^{-18}m$ , which allows WIMP particles to annihilate with each other and be in equilibrium with the thermal bath, much before the freeze-out of WIMPs when  $H \sim n\langle\sigma v\rangle$ . For the superheavy dark matter of  $10^{12}\text{GeV}$  involving only gravitational interaction on scales larger than the particle size  $r_\chi$ , the collision frequency is roughly on the order of  $10^5\text{Hz}$  (Eq. (??)). The competition of three factors determines the formation of the first structure at  $t_\chi = 10^{-6}\text{s}$  when they are comparable, i.e.,  $H \sim v_\chi/r_\chi \sim n\langle\sigma v\rangle$ . Before  $t_\chi$ , the fast expansion prevents the formation of structure and suppresses the particle annihilation such that this superheavy dark matter is never in equilibrium with the thermal bath before  $t_\chi$ . This permits the free streaming calculation for dark matter particles as they are decoupled from the thermal bath before  $t_\chi$  (Eq. (4)). Only at the formation time  $t_\chi$ , superheavy dark matter is in equilibrium with the thermal bath. The expansion, interaction rate, and collision frequency were comparable at that time, allowing the formation of the smallest structures and their subsequent annihilation. The annihilation due to particle self-interaction may be mediated by a MeV scale force mediator. A form of radiation (axion or GW) was also produced due to the binding energy from structure formation. After the formation time  $t_\chi$ , the interaction rate drops below the expansion or  $v_\chi/r_\chi > H > n\langle\sigma v\rangle$ , and dark matter particles freeze out with a constant relic density. Particle annihilation mostly occurs around the formation tie  $t_\chi$ , producing significant extra radiation that may alleviate the Hubble tension problem. Particles may continuously annihilate after  $t_\chi$  at a much lower probability and may produce ultra-high energy cosmic rays (UHECRs) as indirect signatures of dark matter.

## 7 MASS AND ENERGY CASCADE IN DARK MATTER

While the spherical collapse model is a powerful tool for nonlinear structure evolution on small scales (Section 3), it models the evolution of overdensity on a single fixed mass scale. It neglects the interactions between different scales (or haloes of different masses). In this section, we introduce a new type of analytical tool that focuses

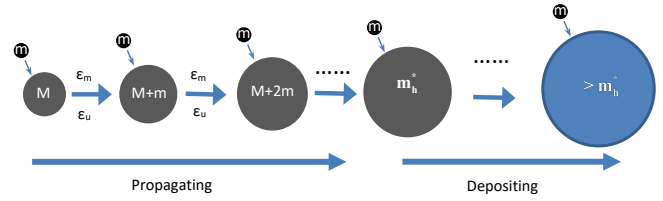


**Figure 12.** Schematic plot for the inverse mass and energy cascade for hierarchical structure formation of dark matter haloes. Individual haloes accrete mass irregularly on short time scales with discrete jumps through minor and major mergers. However, by averaging over time and the halo ensemble, the equivalent description can be: haloes of mass  $M$  merging with a single merger (free DM particles of mass  $m$ ) leads to a mass and energy flux to a larger scale  $M + m$ , that is, the halo of mass  $M$  moving into the next mass sale  $M + m$  after merging. Because haloes have finite mass and kinetic energy, this facilitates a continuous mass and energy cascade from small to large scales across haloes of different masses. Scale-independent mass and energy flux ( $\epsilon_m$  and  $\epsilon_u$  are independent of mass scale  $M$ ) are expected in the propagation range ( $M < m_h^*$ ). The potential energy is directly cascaded from large to small scales at a rate of  $-7/5\epsilon_u$  (see Eq. (110)). The cascade rate becomes scale-dependent in the deposition range ( $M > m_h^*$ ). This concept is quantitatively demonstrated by Illustris simulations in Figs. 14 and 19.

on the mass and energy flow across various scales, i.e., the mass and energy cascade in dark matter flow [40]. This provides a "top-down" approach to postulate dark matter properties from the large-scale behavior of dark matter haloes. We will first introduce the concepts of mass and energy cascade, which can be directly demonstrated and confirmed by N-body simulation results in Sections 8, 9, and 10.

First, long-range gravity requires the formation of a broad spectrum of haloes to maximize the entropy of the self-gravitating collisionless system [46]. We note that highly localized haloes are a major manifestation of non-linear gravitational collapse [47, 48]. As the building blocks of dark matter flow (counterpart to the "eddies" in turbulence), haloes facilitate an inverse mass cascade from small to large mass scales that are absent in turbulence. The "inverse" stands for the direction of cascade from small to large scales, in contrast to the "direct" cascade from large to small scales. The halo-mediated inverse mass cascade is fully consistent with hierarchical structure formation, where haloes grow by a series of sequential merging. In a more realistic picture, individual haloes accrete mass irregularly on short-time scales with discrete jumps through minor and major mergers. However, if we focus on the averaged mass accretion for an ensemble of haloes of the same mass, the averaged halo growth can be much smoother on a larger time scale. On average, this can be equivalently described by continuous merging with minor mergers.

The averaged formation of the halo structure is shown in Fig. 12. Haloes pass their mass onto larger and larger haloes until the growth of the halo mass becomes dominant over the propagation of the mass through haloes of different scales. Consequently, there is a continuous cascade of mass from the smaller to the larger mass scales with mass flux  $\epsilon_m$  independent of the mass scale in a certain range of scales (the propagation range). In that range, the mass flux into any mass scale balances the mass flux out of the same scales so that the total mass of haloes at that scale does not vary with time; i.e., these haloes propagate mass to large scales (small-scale permanence in Fig. 15). The mass cascaded from small scales is finally consumed to grow haloes in the deposition range at scales with  $M > m_h^*$ . From this description, the mass cascade can be described as follows.

"Little haloes have big haloes, That feed on their mass;  
And big haloes have greater haloes, And so on to growth."

Second, haloes have finite kinetic and potential energy. Therefore,

accompanied by the mass cascade, there exists also a simultaneous energy flux (energy cascade at a rate of  $\varepsilon_u$ ) across haloes on different scales. The kinetic energy is also cascaded from small to large scales (the same as the mass cascade), whereas the potential energy is cascaded in the opposite direction. This happens because the potential energy is defined to be negative, while the kinetic energy is positive. When dark matter flow reaches a statistically steady state, the rate of mass and energy cascade must be scale-independent (i.e.,  $\varepsilon_m$  and  $\varepsilon_u$  in Fig. 12 are independent of mass scale  $M$ ). If this is not the case, there would be a net accumulation of mass and energy on some intermediate-mass scale below  $m_h^*$ . We exclude this possibility and require that the statistical structures of haloes be self-similar and scale-free for haloes smaller than  $m_h^*$ . This leads to a scale-independent cascade up to a critical mass  $m_h^*$ . The entire concept can be demonstrated by Illustris simulations in Section 8 (see Figs. 14 and 19). The value of  $\varepsilon_u \approx 10^{-7} m^2/s^3$  for the energy cascade is estimated in Eq. (111). The scaling laws associated with the energy cascade will be derived in Section 12.

Finally, the mass and energy cascades are only relevant on small scales in the nonlinear regime, where haloes of different sizes are the dominant structures ( $r_{fs} < r < r_t$  in Fig. 1). The structure evolution on small scales is highly nonlinear. It can only be studied by N-body simulations with the Newtonian approximation and simplified analytical tools (spherical collapse model, etc., in Section 3). The mass and energy cascade in this section provides another useful approach to understanding the nonlinear structure evolution.

## 8 INVERSE MASS CASCADE IN HALO MASS SPACE

In this section, we present a quantitative description of the mass cascade. To validate the concepts, we used results from the large-scale cosmological Illustris simulation (Illustris-1-Dark) [49]. Illustris is a suite of large-volume cosmological dark matter only and hydrodynamical simulations. The selected Illustris-1-Dark is a dark matter only simulation of a  $106.5 \text{ Mpc}^3$  cosmological volume with  $1820^3$  DM particles for the highest resolution. Each DM particle has a mass around  $m_p = 7.6 \times 10^6 M_\odot$ . The gravitational softening length is around 1.4 kpc. The simulation has cosmological parameters of dark matter density  $\Omega_{DM} = 0.2726$ , dark energy density  $\Omega_{DE} = 0.7274$  at  $z = 0$ , and Hubble constant  $h = 0.704$ . The haloes in the simulation were identified using a standard Friends of Friends (FoF) algorithm with a link length parameter  $b = 0.2$ . Then, all dark matter particles were divided into halo particles with a total mass  $M_h$  and out-of-halo particles that do not belong to any halo. Therefore,  $M_h$  is the total mass of all haloes. We will focus on the evolution of mass and energy in haloes of different mass  $m_h$ .

First, we can mathematically express the mass flux ( $\Pi_m$ ) across haloes of different sizes as

$$\begin{aligned} \Pi_m(m_h, a) &= - \int_{m_h}^{\infty} \frac{\partial}{\partial t} [M_h(a) f_M(m, m_h^*)] dm, \\ &= - \frac{\partial}{\partial t} \left[ \int_{m_h}^{\infty} M_h(a) f_M(m, m_h^*) dm \right] = - \frac{\partial \Lambda_m}{\partial t}, \end{aligned} \quad (90)$$

where  $a$  is the scale factor and  $M_h$  is the total mass in all haloes of all sizes. Here  $f_M(m_h, m_h^*)$  is the halo mass function, that is, the probability distribution of the total mass  $M_h$  in all haloes of different mass  $m_h$ . The total mass of all haloes with a mass between  $m_h$  and  $m_h + dm$  should be  $M_h f_M(m_h, m_h^*) dm$ . The cumulative mass function  $\Lambda_m(m_h, a)$  represents the total mass in all haloes greater

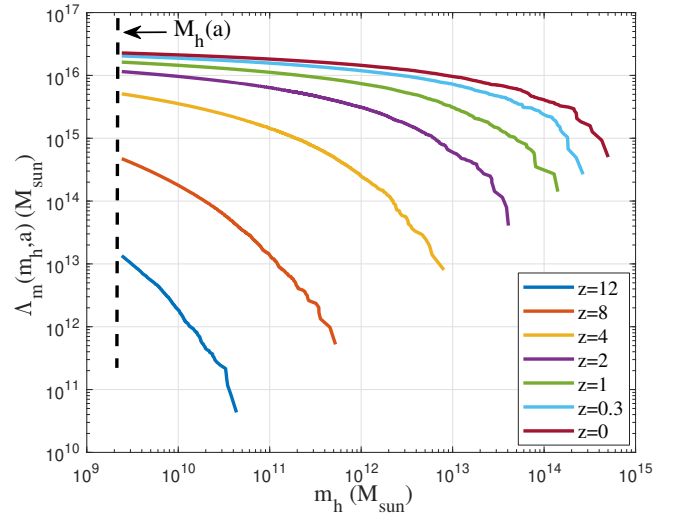


**Figure 13.** The variation of cumulative mass function  $\Lambda_m(m_h, a)$  with halo mass scale  $m_h$  at different redshifts  $z$  from Illustris-1-Dark simulation. The total mass  $M_h(a)$  in all haloes of all sizes is computed with  $m_h \rightarrow 0$ , i.e.  $M_h(a) = \Lambda_m(m_h = 0, a)$ . Using function  $\Lambda(m_h, a)$ , the rate of mass cascade  $\Pi_m(m_h, a)$  in Eq. (90) was computed and presented in Fig. 14.

than the scale  $m_h$ , that is,

$$\Lambda_m(m_h, a) = \int_{m_h}^{\infty} M_h(a) f_M(m, m_h^*) dm. \quad (91)$$

Figure 13 plots the variation of the cumulative mass function  $\Lambda_m(m_h, a)$  with mass scale  $m_h$  and redshifts  $z$  from the Illustris-1-Dark simulation. The total halo mass can be obtained by setting  $m_h \rightarrow 0$  in Eq. (91), i.e.  $M_h(a) = \Lambda_m(m_h \rightarrow 0, a)$ .

The time derivative of  $\Lambda_m$  describes the mass flux from all haloes below the scale  $m_h$  to all haloes above the scale  $m_h$ , i.e., the rate of mass cascade  $\Pi_m$  in Eq. (90). In N-body simulations, we use the difference of  $\Lambda_m$  at two different redshifts  $z_1$  (or  $t_1$ ) and  $z_2$  (or  $t_2$ ) to compute the time derivative and obtain the mass cascade rate  $\Pi_m$ . For Illustris cosmology, the time  $t$  at redshift  $z$  is computed from

$$a(t) = \frac{1}{1+z(t)} = \left( \frac{\Omega_m}{\Omega_\Lambda} \right)^{1/3} \sinh^{2/3} \left( \frac{t}{2/(3H_0\sqrt{\Omega_\Lambda})} \right). \quad (92)$$

Figure 14 presents the variation of the rate of the mass cascade  $\Pi_m(m_h, a)$  with the mass scale  $m_h$  using the values of the cumulative mass function  $\Lambda_m$  at two different redshifts  $z_1$  and  $z_2$  in Fig. 13. In the schematic diagram in Fig. 12, we propose the concept that the rate of cascade  $\Pi_m(m_h, a)$  is independent of the scale  $m_h$  for  $m_h < m_h^*$  in the propagation range since we require that the statistical structures of the haloes be self-similar and scale-free for haloes smaller than  $m_h^*$ . The simulation results confirm this concept, that is, the existence of a propagation range with a scale-independent cascade rate  $\varepsilon_m(a) \equiv \Pi_m(m_h, a)$  for scales  $m_h$  below a critical mass scale  $m_h^*$ . After reaching a statistically steady state, that scale-independent rate  $\varepsilon_m(a) \propto a^{-1}$ , that is, decreases with time and is about  $-0.02 M_\odot/s$  at  $z = 0$  from the Illustris simulation. The time dependence of  $\varepsilon_m(a) \propto a^{-1}$  due to background expansion means a decreasing mass flux in the halo mass space.

As described in the schematic plot in Fig. 12, all masses cascaded from the smallest scale are propagated through the propagation range and are consumed mainly to grow haloes greater than  $m_h^*$  in the deposition range. To explain this, we write the scale-independent  $\varepsilon_m$

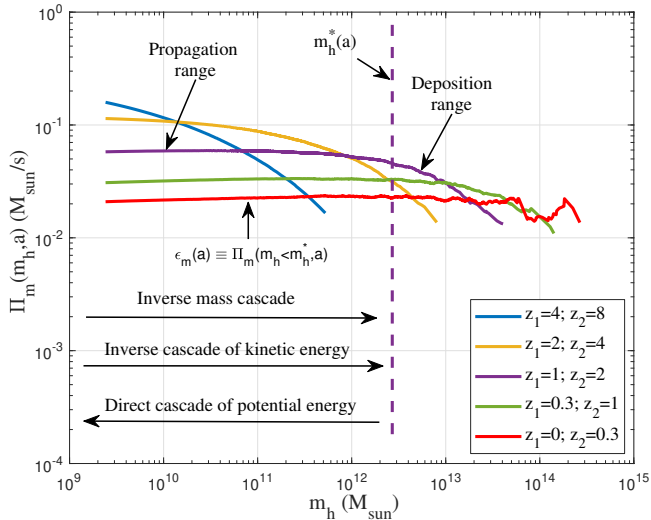


**Figure 14.** Variation of the rate of inverse mass cascade  $\Pi_m(m_h, a)$  (Eq. (90),  $< 0$  for 'inverse'), calculated by the values of the cumulative mass function  $\Lambda_m$  (Eq. (91)) at two different redshifts  $z_1$  and  $z_2$  from Fig. 13. After reaching a statistically steady state, the simulation confirms the existence of a propagation range for the scales  $m_h < m_h^*(a)$ , a characteristic mass scale that increases with time. A scale-independent rate of the mass cascade  $\epsilon_m(a) \equiv \Pi_m(m_h, a)$  can be identified in the propagation range, which decreases with time ( $\epsilon_m(a) \propto a^{-1}$ ) and is around  $-0.02 M_\odot/\text{s}$  at  $z = 0$ . Haloes in the propagation range pass their mass to larger haloes, where the group mass  $m_g$  (total mass of all haloes with the same mass  $m_h$ ) reaches a steady state (see Eq. (94) and Fig. 15). There also exists a simultaneous energy cascade discussed in Section 9.

in the propagation range as

$$\epsilon_m(a) \equiv \Pi_m(m_h, a) = -\frac{\partial M_h}{\partial t} \propto a^{-1} \quad \text{for } m_h < m_h^*, \quad (93)$$

which further requires (from Eq. (90))

$$\frac{\partial \Pi_m}{\partial m_h} = \frac{\partial \epsilon_m}{\partial m_h} = \frac{\partial}{\partial t} [M_h(a) f_M(m_h, m_h^*)] = \frac{1}{m_p} \frac{\partial m_g}{\partial t} = 0. \quad (94)$$

From this, we found that the total mass  $m_g$  for a group of haloes with the same mass  $m_h$  reaches a steady state and does not vary over time for  $m_h < m_h^*$ . Here, the halo group mass  $m_g$  is written as

$$m_g(m_h) = M_h(a) f_M(m_h, m_h^*) m_p = N_h m_h, \quad (95)$$

where  $m_p$  is the mass resolution, and  $N_h$  is the number of haloes in that group. Due to the steady-state group mass  $m_g$ , these haloes propagate the mass from small scales to grow haloes greater than  $m_h^*$ , that is, the "propagation range." This concept can be clearly demonstrated by the Illustris simulations in Fig. 15 such that the halo number density follows  $N_h \propto m_h^{-\lambda-1}$  in that range and is actually independent of the redshift. The mass of the halo group,  $m_g$  of different redshifts, collapses onto the same time-independent power law  $m_g \propto m_h^{-\lambda}$  ( $\lambda = 0.88$  from the Illustris simulation). This is the "so-called" small-scale permanence for the halo group mass ( $m_g$ ) due to the scale-independent mass cascade in Fig. 14, i.e., the mass flux into low-mass halo group balances the mass flux out of the same group. This is also in agreement with the slow decline of the number density of low-mass haloes at low redshift [50]. The small-scale permanence also exists for halo density profiles due to the scale-independent energy cascade (Fig. 28). The halo mass function and density profile can also be analytically derived based on the mass and energy cascade [39].

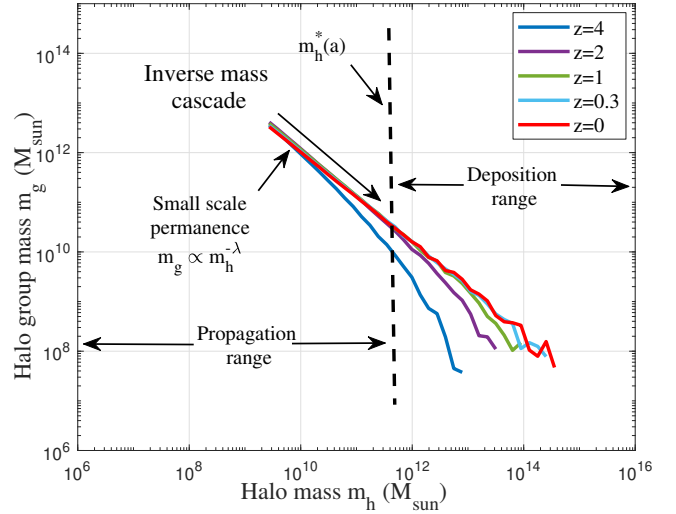


**Figure 15.** The variation of halo group mass  $m_g(m_h)$  for all haloes of the same mass  $m_h$  at different redshifts  $z$  from Illustris-1-Dark simulation. The figure demonstrates the small-scale permanence of the group mass  $m_g$ . Once the statistically steady state is established ( $z \leq 4$ ), the rate of the inverse mass cascade  $\epsilon_m$  becomes scale independent (Eq. (94)) such that the mass of the halo group  $m_g$  at different redshifts  $z$  collapses into a time-independent power law  $m_g \propto m_h^{-\lambda}$  on small mass scales with the halo geometry parameter  $\lambda \approx 0.88$  [39]. This is the so-called "propagation range," where the mass cascaded from the smallest (DM particle) scale is propagated to larger scales, that is, a constant group mass  $m_g$ . The cascaded mass is eventually consumed to grow haloes greater than  $m_h^*$  (the "deposition range"). The propagation range gradually extends to large scales ( $m_h^*(a)$  increases over time) due to the continuous inverse mass cascade.

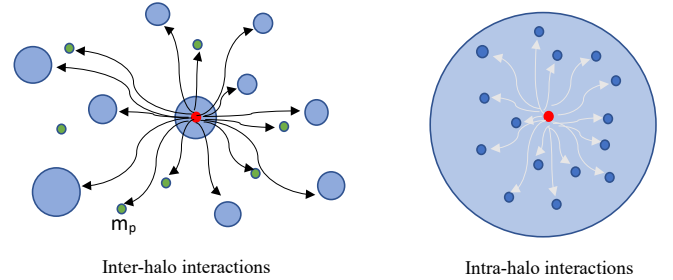


**Figure 16.** Decomposition of kinetic energy into the contributions due to inter-halo interactions on a longer distance and intra-halo interactions on a shorter distance. The inter-halo interactions with all other particles in different haloes and all out-of-halo particles (green) are weaker on larger scales and in the linear regime ( $K_{ph}$ ). The intra-halo interactions with all other particles in the same halo are stronger, on smaller scales, and in the nonlinear regime ( $K_{pv}$ ). The evolution of two KEs is also presented in Fig. 5 and Table 1.

## 9 ENERGY CASCADE IN HALO MASS SPACE

Since haloes have finite energy, there is also a simultaneous energy cascade associated with the mass cascade (Fig. 14). This section presents a quantitative description of the energy cascade in the halo mass space.

To better describe the energy cascade, we start by decomposing the particle kinetic energy into two parts of different nature. In N-body simulations, every halo particle, characterized by a mass  $m_p$ , and a velocity vector  $\mathbf{v}_p$ , should belong to one and only one parent halo. The particle velocity  $\mathbf{v}_p$  can be decomposed as [46]

$$\mathbf{v}_p = \mathbf{v}_h + \mathbf{v}'_p, \quad (96)$$



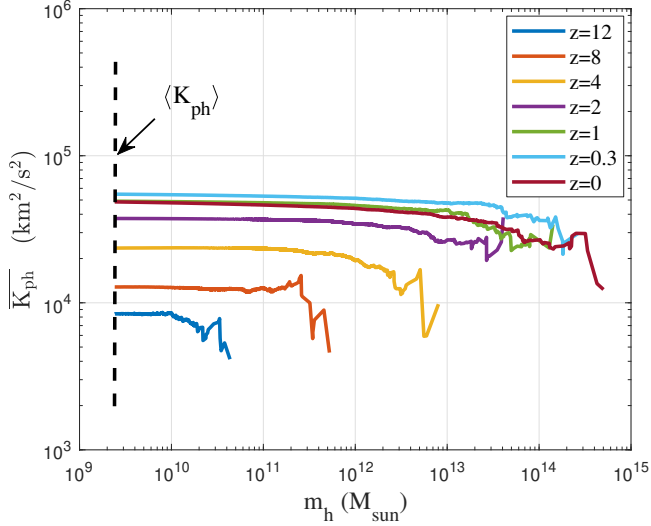


**Figure 17.** The variation of mean halo kinetic energy  $\overline{K_{ph}}$  with halo mass scale  $m_h$  at different redshifts  $z$  from Illustris-1-Dark simulation. The mean halo kinetic energy in all haloes of all sizes is denoted as the black dashed line with  $m_h \rightarrow 0$ , i.e.  $\langle K_{ph} \rangle = \overline{K_{ph}}(m_h \rightarrow 0, a)$ . This figure will be used to compute the evolution of mean halo kinetic energy  $\langle K_{ph} \rangle$  for all halo particles in Fig. 22. Due to the long-range interaction with particles from different haloes, halo kinetic energy increases with time in early matter dominant universe (i.e., the linear regime with  $\langle K_{ph} \rangle \propto t^{2/3}$  shown in Fig. 22). It slightly decreases at low redshift in the dark energy dominant universe due to the accelerated expansion.

namely, the halo mean velocity,  $\mathbf{v}_h = \langle \mathbf{v}_p \rangle_h$ , and the velocity fluctuation,  $\mathbf{v}'_p$ . Here,  $\langle \rangle_h$  represents the average of all particles in the same halo, and  $\mathbf{v}_h$  represents the velocity of that halo.

Consequently, the total kinetic energy  $K_p$  of a given halo particle can be divided into  $K_p = K_{ph} + K_{pv}$ . As shown in Fig. 16, here  $K_{ph} = \mathbf{v}_h^2/2$  (halo kinetic energy) is the contribution from the motion of entire haloes  $\mathbf{v}_h$  due to the inter-halo interaction of that particle with all other particles in different haloes and all out-of-halo particles (green). This part of the kinetic energy is related to interactions on large scales in the linear regime. While  $K_{pv} = \mathbf{v}'_p^2/2$  (virial kinetic energy) is the contribution of the velocity fluctuation  $\mathbf{v}'_p$  due to the intra-halo interaction of that particle with all other particles in the same halo. This part of the kinetic energy is from halo virialization and is due to interactions on a shorter distance and smaller scales in the non-linear regime. Like the energy cascade associated with nonlinear interactions in turbulence, the energy cascade in this work is focused on the cascade of the virial kinetic energy  $K_{pv}$  across different scales in the deeply non-linear regime.

Similar to the cumulative mass function  $\Lambda_m$  in Eq. (91), the cumulative kinetic energies ( $\Lambda_{ph}$  and  $\Lambda_{pv}$ ) represent the total kinetic energies  $K_{ph}$  and  $K_{pv}$  in all haloes greater than  $m_h$ , such that

$$\begin{aligned} \Lambda_{ph}(m_h, a) &= \int_{m_h}^{\infty} M_h(a) f_M(m, m_h^*) K_{ph} dm, \\ \Lambda_{pv}(m_h, a) &= \int_{m_h}^{\infty} M_h(a) f_M(m, m_h^*) K_{pv} dm, \\ K_{ph} &= \frac{3}{2} \sigma_h^2(m, a) \quad \text{and} \quad K_{pv} = \frac{3}{2} \sigma_v^2(m, a). \end{aligned} \quad (97)$$

Here,  $\sigma_h^2$  and  $\sigma_v^2$  are the dispersion of the one-dimensional velocity for the halo velocity  $\mathbf{v}_h$  and the velocity fluctuation  $\mathbf{v}'_p$  [39].

Next, we will use the cumulative kinetic energy and cumulative

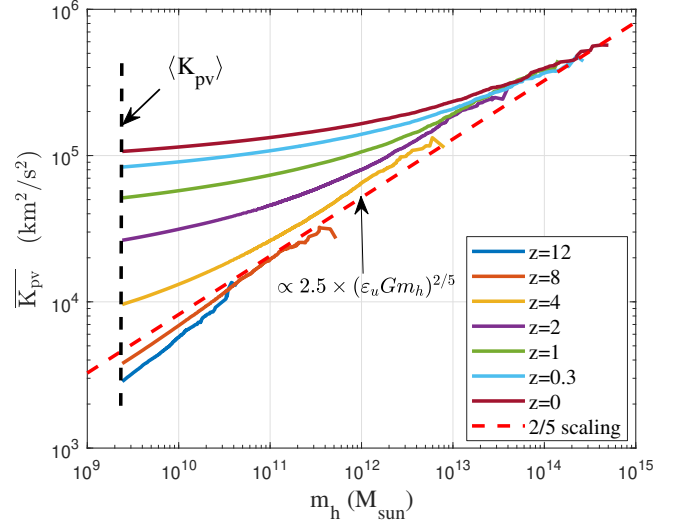


**Figure 18.** The variation of mean virial kinetic energy  $\overline{K_{pv}}$  with halo mass scale  $m_h$  at different redshifts  $z$  from Illustris-1-Dark simulation. The mean virial kinetic energy in all haloes of all sizes is denoted as the black dashed line with  $m_h \rightarrow 0$ , that is,  $\langle K_{pv} \rangle = \overline{K_{pv}}(m_h \rightarrow 0, a)$  in Fig. 22. This figure is used to calculate the rate of the energy cascade  $\epsilon_u$  in Fig. 19. Due to the virialization of the halo and the interaction with particles in the same halo, the virial kinetic energy  $K_{pv}$  increases with time (the non-linear regime with  $\langle K_{pv} \rangle \propto t^1$  shown in Fig. 22). The dark energy has negligible effects on the virial kinetic energy due to the bounded halo structure. The 2/5 scaling ( $\overline{K_{pv}} \propto m_h^{2/5}$  for  $m_h \rightarrow \infty$ ) is also presented for comparison (Eq. (126)).

mass  $\Lambda_m$  to calculate the mean specific halo kinetic energy (energy per unit mass)  $\overline{K_{ph}}$  and the virial kinetic energy  $\overline{K_{pv}}$  in all haloes above any mass scale  $m_h$ , that is,

$$\overline{K_{ph}} = \frac{\Lambda_{ph}}{\Lambda_m} \quad \text{and} \quad \overline{K_{pv}} = \frac{\Lambda_{pv}}{\Lambda_m}. \quad (98)$$

Figures 17 and 18 plot the variation of the (specific) halo kinetic energy  $\overline{K_{ph}}$  and the virial kinetic energy  $\overline{K_{pv}}$  with the halo mass  $m_h$  from Illustris simulations. The halo kinetic energy is relatively independent of  $m_h$ . The virial kinetic energy increases with the mass of the halo  $m_h$  with  $\overline{K_{pv}} \propto m_h^{2/5}$  for larger haloes. This can be explained by the scaling laws in Eq. (126). Both kinetic energies increase with time but with different scaling behavior due to the nature of interactions in the linear and nonlinear regimes (Fig. 22).

Next, we will focus on the energy cascade of the specific virial kinetic energy  $K_{pv}$  due to nonlinear interactions on small scales. For the inverse mass cascade in Eq. (90), the change in total halo mass above the scale  $m_h$ , that is, the cumulative mass function  $\Lambda_m(m_h, a)$ , comes entirely from the mass cascade or the interactions between all haloes below the scale  $m_h$  and all haloes above  $m_h$ . Similarly, the change in the (specific) virial kinetic energy  $\overline{K_{pv}}$  for all haloes above the scale  $m_h$  comes entirely from the energy cascade due to interactions between haloes below and above the scale  $m_h$ . This is because, without an energy cascade, haloes above the scale  $m_h$  should be in virial equilibrium, where the specific kinetic energy  $\overline{K_{pv}}$  is constant and conserved with time (see Eq. (106) for an explanation), just as the total halo mass above the scale  $m_h$  is conserved without a mass cascade. Therefore, similar to the mass cascade  $\Pi_m$  in Eq.

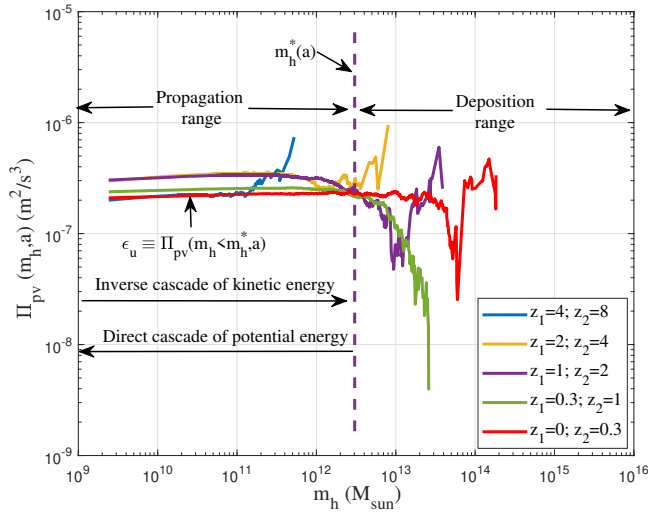


**Figure 19.** The variation of the rate of energy cascade  $\Pi_{pv}(m_h, a)$  (Eq. (99)) with halo mass scale  $m_h$  at different redshifts  $z$  from Illustris-1-Dark simulation. A scale-independent constant rate of  $\epsilon_u$  can be identified in the propagation range for an inverse cascade of virial kinetic energy  $K_{pv}$  from the smallest scale (single DM particle) to larger scales. That rate is also relatively independent of time and is around  $\epsilon_u = -2.5 \times 10^{-7} \text{m}^2/\text{s}^3$  (also see Fig. 22). There also exists a simultaneous direct cascade of potential energy from large to the smallest scale at a rate of  $-7/5 \epsilon_u$  (see Eq. (110)).

(90), the rate of cascade for the virial kinetic energy  $K_{pv}$  reads

$$\begin{aligned} \Pi_{pv}(m_h, a) &= -\frac{\partial}{\partial t} \left( \overline{K_{pv}} \right) = -\frac{\partial}{\partial t} \left( \frac{\Lambda_{pv}}{\Lambda_m} \right) \\ &= -\frac{\partial}{\partial t} \int_{m_h}^{\infty} \frac{M_h(a) f_M(m, m_h^*) K_{pv}}{\int_{m_h}^{\infty} M_h(a) f_M(m, m_h^*) dm} dm, \end{aligned} \quad (99)$$

where  $\overline{K_{pv}}$  is defined in Eq. (98), i.e. the specific virial kinetic energy in all haloes greater than  $m_h$ . Similar to Eq. (90), Eq. (99) describes the rate of transfer of specific virial kinetic energy ( $K_{pv}$ ) from haloes below the scale  $m_h$  to haloes above the scale  $m_h$  at a rate of  $\Pi_{pv}$ .

Figure 19 plots the variation of  $\Pi_{pv}$  with the halo mass  $m_h$  and the redshifts  $z$ . The mean (specific) virial kinetic energy  $\overline{K_{pv}}$  at two different redshifts  $z_1$  and  $z_2$  in Fig. 18 was used to calculate  $\Pi_{pv}$  in this figure. Similarly to the mass cascade in Fig. 12, if the statistical structures of the haloes are self-similar and scale-free for haloes smaller than the characteristic mass  $m_h^*$ , the rate of the energy cascade  $\epsilon_u$  should also be independent of the scale  $m_h$  for  $m_h < m_h^*$ , i.e. the energy flux into a given group of haloes should balance the energy flux out of the same group. The simulation results confirm a scale- and time-independent rate of cascade  $\epsilon_u$ . Therefore, in the propagation range ( $m_h < m_h^*$ ),

$$\epsilon_u \equiv \Pi_{pv}(m_h, a) = -\frac{\partial \langle K_{pv} \rangle}{\partial t} \propto \epsilon_m \frac{\langle K_{pv} \rangle}{M_h}, \quad (100)$$

where the rate of energy cascade  $\epsilon_u$  can be directly related to the rate of mass cascade  $\epsilon_m$ . Since  $\epsilon_u$  is scale independent, with continuous injection of virial kinetic energy  $K_{pv}$  at a constant rate of  $\epsilon_u$  on the smallest scale, we should expect the total  $K_{pv}$  in all haloes of all sizes to be proportional to time  $t$  or  $\langle K_{pv} \rangle \propto t$ . This is consistent with the solutions of the cosmic energy equation in the next section (Eq. (110) and Fig. 22).

Up to this point, we have discussed the mass and energy cascade in halo mass space. The rate of the energy cascade  $\epsilon_u \approx -10^{-7} \text{m}^2/\text{s}^3$

can be estimated for galactic haloes from cosmological simulations (Fig. 19). This is consistent with  $\epsilon_u$  obtained on the smallest scale for particles of critical mass  $m_{Xc}$  in Eqs. (56). This is, of course, not a mere coincidence as the key parameter  $\epsilon_u$  is a constant independent of both scale and time, as shown in Fig. 19. The value of  $\epsilon_u$  estimated for small and large haloes should be the same.

## 10 COSMIC ENERGY EVOLUTION

To better understand the energy cascade, we provide an analysis based on the energy evolution in self-gravitating collisionless dark matter flow. The equations of motion for  $N$  collisionless particles in comoving coordinates  $\mathbf{x}$  and physical time  $t$  read [51]:

$$\frac{d^2 \mathbf{x}_i}{dt^2} + 2H \frac{d\mathbf{x}_i}{dt} = -\frac{Gm_p}{a^3} \sum_{j \neq i}^N \frac{\mathbf{x}_i - \mathbf{x}_j}{|\mathbf{x}_i - \mathbf{x}_j|^3}, \quad (101)$$

where  $N$  particles have equal mass  $m_p$ . The Hubble parameter  $H(t) = \dot{a}/a$ . Here,  $H$  has a "damping" effect, which leads to the decrease in total energy of the  $N$ -body system (Eq. (106) and Fig. 21). In the radiation and matter eras, the Hubble parameter satisfies  $Ht = 1/2$  and  $Ht = 2/3$ , respectively (Table 1). In the dark energy era, the Hubble parameter  $H$  approaches a constant value  $H_0^* = H_0 \sqrt{\Omega_\Lambda}$ , where  $\Omega_\Lambda$  is the fraction of dark energy.

Next, we will derive the energy evolution based on equations of motion (Eq. (101)). We first introduce a transformed time variable  $s$  as  $ds/dt = a^p$ , where  $p$  is an arbitrary exponent. In terms of the new time variable  $s$ , the original Eq. (101) can be transformed to

$$\begin{aligned} \frac{d^2 \mathbf{x}_i}{ds^2} + \frac{d\mathbf{x}_i}{ds} (p+2) a^{-p} H &\equiv a^{-(3+2p)} \frac{\mathbf{F}_i}{m_p}, \\ \frac{\mathbf{F}_i}{m_p} &= -Gm_p \sum_{j \neq i}^N \frac{\mathbf{x}_i - \mathbf{x}_j}{|\mathbf{x}_i - \mathbf{x}_j|^3} = -\frac{\partial P_s}{\partial \mathbf{x}_i}, \end{aligned} \quad (102)$$

where  $\mathbf{F}_i$  is the resultant force on particle  $i$  from all other particles, while  $P_s$  is the total specific potential energy in comoving coordinates. Equation (102) reduces to the original Eq. (101) when  $p = 0$ . With  $p = -2$ , the first-order derivative vanishes in Eq. (102) and  $s$  is the time variable for integration in  $N$ -body simulations. By setting  $p = -1$ ,  $s$  is the conformal time. By setting  $p = -3/2$  along with  $H_0^2 = H^2 a^3$  for the matter era, the equation of motion becomes

$$\frac{d^2 \mathbf{x}_i}{ds^2} + \frac{1}{2} H_0 \frac{d\mathbf{x}_i}{ds} = \frac{\mathbf{F}_i}{m_p}. \quad (103)$$

In this transformed equation for the matter era, the scale factor  $a$  is not explicitly involved. The time-dependent Hubble parameter  $H$  is replaced by a Hubble constant  $H_0$  (or a constant "damping"), which can offer significant convenience in analytically solving the equations of motion.

We first identify the transformation between velocity  $\mathbf{v}_i$  in time variable  $s$  and the peculiar velocity  $\mathbf{u}_i$ ,

$$\begin{aligned} \mathbf{v}_i &= \frac{d\mathbf{x}_i}{ds} = a^{-p} \frac{d\mathbf{x}_i}{dt} = a^{-p-1} \mathbf{u}_i, \quad \mathbf{u}_i = a \frac{d\mathbf{x}_i}{dt}, \\ K_s &= K_p a^{-2p-2}, \quad P_s = a P_y, \end{aligned} \quad (104)$$

where the kinetic energy  $K_s$  and the potential  $P_s$  in the transformed equation can now be related to the peculiar kinetic energy  $K_p$  and the potential  $P_y$  in the physical coordinates.

The energy evolution of the  $N$ -body system can be obtained by multiplying  $\mathbf{v}_i = d\mathbf{x}_i/ds$  on both sides of Eq. (102) and adding the equation of motion for all particles together [52]. An exact and simple

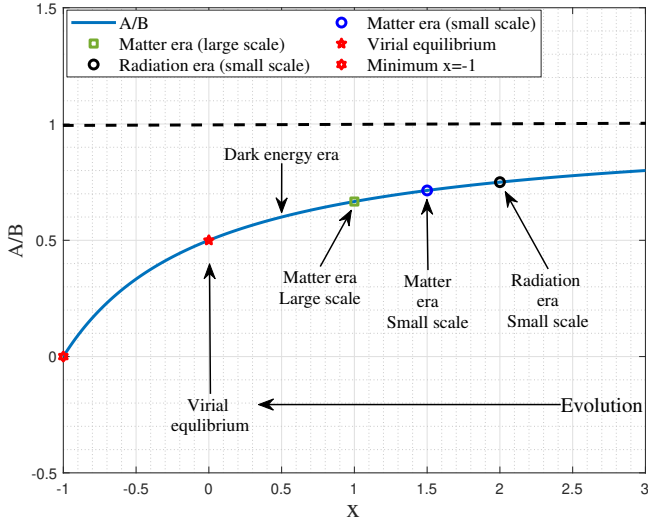


**Figure 20.** The evolution of  $A/B$  for N-body system in different eras. The solid line represents the analytical solution in Eq. (107). Symbols represent the solution for different eras. The initial state  $x = \infty$  should have a total energy  $E_y = 0$  or  $A = B$ . In the radiation era, the kinetic energy on small scales evolves as  $K_{pv} \propto a^2 \propto t$  such that  $A/B = 3/4$  (black circle). In the matter era, the kinetic energy on large scales evolves as  $K_{ph} \propto a$  such that  $A/B = 2/3$  (green circle), while the kinetic energy on small scales follows  $K_{pv} \propto a^{3/2} \propto t$  such that  $A/B = 5/7$  (blue circle). For the dark energy era,  $x$  decreases to 0 and  $A/B \rightarrow 1/2$  so that the system approaches the limiting virial equilibrium (red star). The minimum possible  $x = -1$  is also denoted as the limiting state for the dissipative gas in the bulge where the kinetic energy of gases decreases with time as  $K_p \propto a^{-1}$  [55].

equation (in time variable  $s$ ) for the specific kinetic energy  $K_s$  and the potential energy  $P_s$  can be obtained as

$$\frac{dK_s}{ds} + 2HK_s(p+2)a^{-p} + a^{-(3+2p)}\frac{dP_s}{ds} = 0. \quad (105)$$

By setting  $p = 0$  and using the relations in Eq. (104), the exact cosmic energy equation for energy evolution of the N-body system reads

$$\frac{\partial E_y}{\partial t} + H(2K_p + P_y) = 0, \quad (106)$$

which describes the energy evolution in an expanding background. Here  $K_p$  is the peculiar kinetic energy,  $P_y$  is the potential energy in physical coordinates and  $E_y = K_p + P_y$  is the total specific energy. This is also known as the Layzer-Irvine equation [53, 54]. Here, we derive it using a different approach.

Next, we will focus on the solutions of the cosmic energy equation in different eras. Without loss of generality, we can assume that  $K_p = Aa^x$  and  $P_y = -Ba^x$  and substitute them into Eq. (106), the general solution to the cosmic energy equation reads

$$\frac{A}{B} = \frac{1+x}{2+x}. \quad (107)$$

Solutions at different stages are identified and presented in Fig. 20. First, the case of  $x = \infty$  corresponds to an initial state with vanishing total energy  $E_y = 0$  or  $A = B$ . Next, we focus on the evolution in different eras.

(i) For the radiation era, the kinetic energy on large scales (halo kinetic energy  $K_{ph}$ ) is suppressed and constant over time, similarly to the overdensity  $\delta$  on large scales (Eq. (44)). However, kinetic energy on small scales increases linearly with time due to the energy cascade across haloes, i.e.,

$$K_{pv} = -\varepsilon u t \propto a^2 \quad \text{and} \quad K_{ph} = V_{||}^2/2 \propto a^0. \quad (108)$$

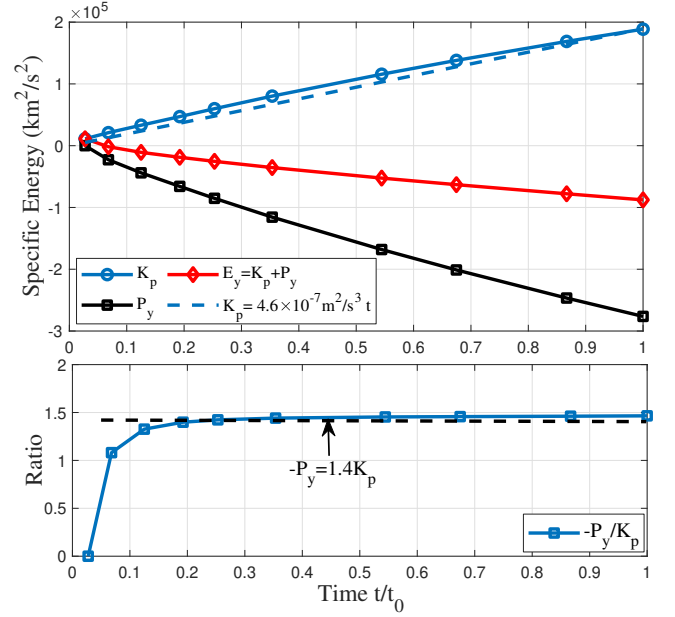


**Figure 21.** The variation of specific (energy per unit mass) kinetic energy  $K_p$ , potential energy  $P_y$ , and total energy  $E_y = K_p + P_y$  (unit:  $\text{km}^2/\text{s}^2$ ) with time  $t$  from Virgo SCDM simulation. Solution in Eq. (110) is also presented for comparison with  $\varepsilon_u = -4.6 \times 10^{-7} \text{m}^2/\text{s}^3$ . Simulation confirms a linear increase of  $K_p = -\varepsilon u t$  with time and negative potential energy  $P_y = -1.4K_p$ . The total energy  $E_y = -0.4K_p$  also decreases with time, which requires a viable mechanism to dissipate the total energy  $E_y$ . Similar to the kinetic energy, the Figure reveals a direct cascade of potential energy at a rate of  $-1.4\varepsilon_u$  from large to the smallest scale.

The exact solution is, therefore,  $A/B = 3/4$  with  $x = 2$  from Eq. (107) (the black circle in Fig. 20) for the ratio between kinetic and potential energies on small scales. The evolution of  $K_{ph}$  and  $K_{pv}$  in the radiation era is also presented in Figs. 5 and 22.

(ii) For the matter era, the kinetic energy on large scales follows  $K_{ph} \propto a$  (Eq. (44)), and the exact solution is  $A/B = 2/3$  with  $x = 1$  (green square in Fig. 20). The kinetic energy on small scales increases linearly with time. The corresponding solution is  $A/B = 5/7$  with  $x = 3/2$  from Eq. (107) (blue circle in Fig. 20). We have solutions:

$$K_{pv} = -\varepsilon u t \quad \text{and} \quad K_{ph} = -\varepsilon_u (a/a_\Lambda)^{-1/2} t. \quad (109)$$

Therefore, when most dark matter mass resides in haloes, the kinetic and potential energies of the entire N-body system are dominated by energy on small scales and should be

$$K_p = At = -\varepsilon u t, \quad P_y = -Bt = \frac{7}{5}\varepsilon u t. \quad (110)$$

This solution can be directly validated by N-body simulations. Figure 21 was generated from the matter-dominant Virgo simulation (SCDM) with a matter density  $\Omega_{DM} = 1$  and dark energy  $\Omega_{DE} = 0$ . A comprehensive description of this simulation can be found in [31, 32]. The kinetic energy  $K_p$  and the potential energy  $P_y$  were calculated as the mean energy of all dark matter particles in the N-body system. Figure 21 confirms the solution in Eq. (110), i.e. a linear increase of  $K_p$  with time and a negative potential energy  $P_y = -1.4K_p$ . The total cosmic energy  $E_y = -0.4K_p$  also decreases with time, as if "dissipated", even though there is no viscous force in the collisionless dark matter. This energy "dissipation" is balanced by a steady energy cascade from large to small scales when a statistically steady state is established for collisionless dark matter

flow [40]. Therefore, the rate of energy cascade ( $\varepsilon_u < 0$  for "inverse") equals the rate of energy "dissipation" and reads

$$\varepsilon_u = -\frac{K_p}{t} = -\frac{3}{2} \frac{u^2}{t} = -\frac{3}{2} \frac{u_0^2}{t_0} \approx -4.6 \times 10^{-7} \frac{m^2}{s^3}, \quad (111)$$

where  $u_0 \equiv u(t=t_0) \approx 350 \text{ km/s}$  is the one-dimensional velocity dispersion of all dark matter particles, and  $t_0 \approx 13.7$  billion years is the physical time at present epoch or the age of the universe. Different simulations may have slightly different values of  $u_0$  due to different cosmological parameters. However, the rate of cascade  $\varepsilon_u \sim -10^{-7} m^2/s^3$  should be a good estimate. This value is also consistent with Eq. (15) for particles with a critical mass of  $m_{Xc} = 10^{12} \text{ GeV}$ .

(iii) For dark energy era,  $A/B$  monotonically decreases with  $x$  and approaches the limiting virial equilibrium with  $A/B = 1/2$  (red star in Fig. 20). In the matter era, the total halo mass  $M_h$  and the characteristic halo mass  $m_h^*$  increase rapidly over time (Table 2). In the dark energy era, this increase slows down due to the accelerated expansion. Their evolution can be written as (Eqs. (93) and (61))

$$\frac{dM_h}{dt} = -\varepsilon_m \propto a^{-1} \quad \text{and} \quad \frac{dm_h^*}{dt} = \frac{m_X}{\tau_g} \propto m_h^{2/3} a^{-1}. \quad (112)$$

The solutions for halo mass evolution in the dark energy era are

$$M_h(t) = M_h(t_\Lambda) \frac{1 - C_1 \exp(-H_0^* t)}{1 - C_1 \exp(-H_0^* t_\Lambda)}, \quad (113)$$

$$m_h^*(t) = m_h^*(t_\Lambda) \left( \frac{1 - C_2 \exp(-H_0^* t)}{1 - C_2 \exp(-H_0^* t_\Lambda)} \right)^3,$$

where  $C_1$  and  $C_2$  are two constants that can be obtained from boundary conditions at  $t_\Lambda$ . Here,  $t_\Lambda$  and  $a_\Lambda$  are the time and scale factor at the equality of matter and dark energy,

$$a_\Lambda = \left( \frac{\Omega_m}{\Omega_\Lambda} \right)^{1/3}, \quad t_\Lambda = \frac{2 \text{asinh}(1)}{3H_0 \sqrt{\Omega_\Lambda}}, \quad \text{and} \quad H_0^* = H_0 \sqrt{\Omega_\Lambda}. \quad (114)$$

The virial kinetic energy on small scales increases linearly with time in both the radiation and matter eras, i.e.  $K_{pv} = -\varepsilon_u t$  (see Table 2 for relevant quantities). In the dark energy era, the rate of the energy cascade  $\varepsilon_u$  slows down. Kinetic energies on both large and small scales level off as a result of the accelerated expansion. The evolution of kinetic energy follows (from Eq. (100)):

$$\frac{dK_{pv}}{dt} = -\varepsilon_u \propto -\frac{\varepsilon_m}{M_h} K_{pv} \propto a^{-1} \quad \text{and} \quad \frac{dK_{ph}}{dt} \propto a^{-1}, \quad (115)$$

with corresponding solutions (dotted lines in Fig. 22):

$$K_{pv} = -\varepsilon_u t_\Lambda - \varepsilon_u a_\Lambda \int_{t_\Lambda}^t a^{-1} dt, \quad (116)$$

$$K_{ph} = -\varepsilon_u t_\Lambda - \frac{2}{3} \varepsilon_u a_\Lambda \int_{t_\Lambda}^t a^{-1} dt.$$

The energy evolution of the N-body system is, of course, fully consistent with the picture of the energy cascade. With the virial kinetic energy  $K_{pv}$  continuously cascaded from the smallest scale to the larger scales at a constant rate  $\varepsilon_u$ ,  $K_{pv}$  increases linearly with time  $t$ . Fig. 22 presents the evolution of kinetic energy on large scales ( $K_{ph}$ ) and small scales ( $K_{pv}$ ) in different eras. The simulation data in Figs. 17 and 18 were used to plot the time evolution in Fig. 22 (symbols). The solution in Eq. (110) is also presented for comparison with a constant rate of the cascade  $\varepsilon_u = -2.5 \times 10^{-7} m^2/s^3$ . As expected, the halo kinetic energy

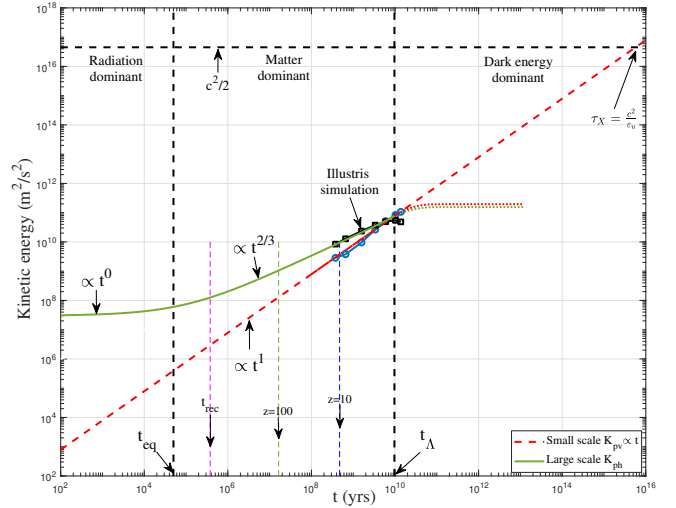


**Figure 22.** The variation of the specific kinetic energy (energy per unit mass)  $K_{ph}$  on large scales and  $K_{pv}$  for haloes on small scales with time  $t$  (yrs) from Illustris-1-Dark simulation. Solution in Eq. (110) is also presented for comparison with  $\varepsilon_u = -2.5 \times 10^{-7} m^2/s^3$ . The large-scale kinetic energy  $K_{ph}$  is constant in the radiation era and increases in the matter era (i.e., the linear regime with  $K_{ph} \propto t^{2/3}$ ). It slightly decreases at low redshift in the dark energy dominant universe due to the accelerated expansion. Due to intra-halo interactions on small scales (the non-linear regime), the small-scale kinetic energy  $K_{pv} = -\varepsilon_u t$  in both radiation and matter eras. In the dark energy era, both kinetic energies level off because of the accelerated expansion and self-limiting effects of dark energy (dotted lines). By assuming that virial velocity cannot exceed the speed of light, a characteristic time  $\tau_X = c^2/\varepsilon_u = 10^{16} \text{ yrs}$  can be obtained. The true lifetime of dark matter can be greater than  $\tau_X$ .

$K_{ph}$  scales as  $\propto t^{2/3}$  due to inter-halo interactions in the linear regime and levels off at low redshift  $z$ . In the nonlinear regime, the virial kinetic energy  $K_{pv}$  scales as  $\propto \varepsilon_u t$  due to the inverse cascade of kinetic energy. This is true for at least up to  $z = 0$ , as shown in the figure. Now, let us consider the following two scenarios:

i) Dark matter can exist independently of dark energy such that we can consider a matter-dominant universe without dark energy. In this case, the scalings for the halo mass  $m_h^* \propto t$  and the kinetic energy  $K_{pv} \propto -\varepsilon_u t$  can extend up to a characteristic time  $\tau_X$  (red dashed line in Fig. 22). By assuming that the speed of particles cannot exceed the speed of light, the characteristic time should be  $\tau_X \propto -c^2/\varepsilon_u = 10^{16} \text{ yrs}$ . Relativistic corrections might be required for a more accurate result. This scenario leads to continuous halo growth, even in the dark energy era, which is not plausible. Dark energy is required to limit and slow down the halo growth.

ii) Dark matter and dark energy have a related and dependent origin. In this case, dark matter must coexist with dark energy. The linear relation  $K_{pv} \propto -\varepsilon_u t$  breaks down much earlier than the time  $\tau_X$ , as dark energy prevents the formation of large haloes. Therefore, virial velocities might level off and never reach the speed of light (dotted lines in Fig. 22). If this is the case, the true lifetime of dark matter can be much greater than  $\tau_X = 10^{16} \text{ yrs}$ . In this scenario, dark energy provides a self-limiting mechanism to slow down the growth of characteristic halo mass  $m_h^*$  and the kinetic energy  $K_{pv}$ .

In summary, three important observations can be obtained from the energy evolution (Table 2) and the picture of the energy cascade in Figs. 12, 14, 19, 21, and 22, .

(i) Due to the energy cascade in halo mass space, linear evolution



**Table 2.** Cosmic mass and energy evolution in different eras

Quantity	Symbol	Radiation era	Matter era	Dark energy era
Time	$t$	$a^2$	$a^{3/2}$	$\ln a/H_0^*$
Hubble parameter	$H_t$	$1/2$	$2/3$	$H_0^* t$
Large-scale overdensity	$\delta$	$a^0$	$a^1$	$a^0$
Large-scale KE	$K_{ph}$	$a^0$	$a^1$	$a^0$
Small-scale KE	$K_{pv}$	$t^1$	$t^1$	$t^0$
Ratio of A to B (Eq. (107))	$A/B$	$3/4$	$5/7$	$1/2$
Characteristic halo mass	$m_h^*$	$a^5$	$a^{3/2}$	$a^0$
Total halo mass	$M_h$	$a^{5/3}$	$a^{1/2}$	$a^0$
Rate of mass cascade	$\varepsilon_m$	$a^{-1/3}$	$a^{-1}$	$a^{-1}$
Rate of energy cascade	$\varepsilon_u$	$a^0$	$a^0$	$a^{-1}$

of kinetic energy  $K_{pv} = -\varepsilon_u t$  on small scales can be obtained for both radiation era and matter era. This is also consistent with the cosmic energy equation (Eq. (106)) and the N-body simulations. This is important such that the scaling laws involving  $\varepsilon_u$  that we will develop in Section 12 are valid in both eras.

(ii) Without dark energy, our universe will stuck in a statistically steady state (matter era of blue circle in Fig. 20), which involves an energy cascade at a constant rate  $\varepsilon_u$  and a mass cascade at a decreasing rate  $\varepsilon_m$ . Without dark energy, the kinetic energy  $K_{pv}$  and halo mass  $m_h^*$  will continuously increase until a characteristic time  $\tau_X$  in Fig. 22. Since the total amount of dark matter in the universe is fixed, a mechanism is required to limit the growth of  $m_h^*$  and  $K_{pv}$ . From this perspective, dark energy and dark matter must coexist with each other. Dark energy provides a self-limiting mechanism to limit the growth of dark matter structures.

(iii) Only with the help of dark energy is our universe able to evolve toward the limiting virial equilibrium with a decreasing rate of cascade. The mass and energy cascade only completely vanishes for the system exactly in the limiting virial equilibrium (red star in Fig. 20). Similarly, haloes evolve toward the limiting virial equilibrium with a decreasing rate of cascade. The energy cascade only vanishes in completely virialized haloes. Haloes in their early stage of evolution have a higher rate of cascade than haloes in their late stage of evolution. However, both real and simulated haloes should always have a finite rate of energy cascade (next section).

## 11 ENERGY CASCADE IN SPHERICAL HALOES

The mass and energy cascade in halo mass space describes the interactions between haloes of different masses. In the radiation and matter eras, the mass and energy cascade established a statistically steady state to continuously release the system energy and maximize the entropy [46]. In the dark energy era, the system approaches the limiting virial equilibrium with a slower mass and energy cascade (Fig. 20). Similarly, there also exists an energy cascade in haloes, while these haloes evolve toward limiting equilibrium. The energy cascade only vanishes for completely virialized haloes. This section quantifies the energy cascade in haloes. The same theory can also be applied to the energy flow in dissipative gases and the associated scaling laws for bulge mass, size, and dynamics [55].

To infer the internal structure of dark matter haloes, we examine the energy cascade in haloes at a given mass  $m_h$ . Similarly to the mass and energy cascade in the halo mass space (Sections 8 and 9),

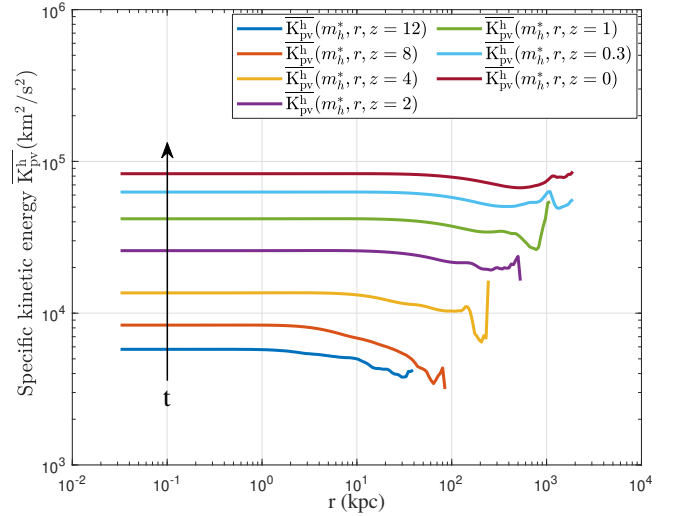


**Figure 23.** The variation of mean specific kinetic energy  $\overline{K_{pv}^h}$  with radial scale  $r$  for all haloes of characteristic mass  $m_h^*(z)$  at different redshift  $z$ . Data is calculated by Eq. (119) and used to compute the rate of energy cascade  $\varepsilon(m_h, z)$  in haloes in Fig. 24.

we start by introducing the cumulative functions along the halo radial direction  $r$ . The cumulative mass function  $\Lambda_m^h(m_h, r, z)$  (similar to  $\Lambda_m$  in Eq. (91)) represents the total mass enclosed above the scale  $r$ . This quantity is averaged for all haloes of the same mass  $m_h$

$$\Lambda_m^h(m_h, r, z) = \int_r^\infty \rho_h(m_h, r', z) 4\pi r'^2 dr'. \quad (117)$$

where  $\rho_h$  is the mean mass density for all haloes of the same mass.

As usual (see Eq. (96)), next, we decompose the halo particle velocity  $\mathbf{v}_p$  into the halo mean velocity,  $\mathbf{v}_h = \langle \mathbf{v}_p \rangle_h$ , and the velocity fluctuation,  $\mathbf{v}_p' = \mathbf{v}_p - \mathbf{v}_h$ . Here,  $\mathbf{v}_h$  represents the velocity of that halo, that is, the average velocity of all particles in the same halo. Consequently, the total kinetic energy  $K_p$  of a given particle can be divided into  $K_p = K_{ph} + K_{pv}$ . The virial kinetic energy,  $K_{pv} = \mathbf{v}_p'^2/2$ , is the contribution from the velocity fluctuation due to the intra-halo interactions on small scales in the nonlinear regime (Fig. 16). Only this part of the kinetic energy is relevant for the energy cascade in haloes. We will focus on  $K_{pv}$  and introduce a cumulative kinetic energy function  $\Lambda_{pv}^h$  for  $K_{pv}$

$$\Lambda_{pv}^h(m_h, r, z) = \int_r^\infty K_{pv} \rho_h(m_h, r', z) 4\pi r'^2 dr'. \quad (118)$$

Next, similarly to the energy cascade in the mass space (Eq. (98)), we introduce the specific kinetic energy on scale  $r$  for all haloes of the same mass  $m_h$  that reads

$$\overline{K_{pv}^h}(m_h, r, z) = \frac{\Lambda_{pv}^h}{\Lambda_m^h} = \frac{\int_r^\infty K_{pv} \rho_h(m_h, r', z) 4\pi r'^2 dr'}{\int_r^\infty \rho_h(m_h, r', z) 4\pi r'^2 dr'}. \quad (119)$$

Here,  $\overline{K_{pv}^h}$  is the specific energy (energy per unit mass) contained on scales above  $r$ . Figure 23 plots the variation of the specific kinetic energy  $\overline{K_{pv}^h}$  with the scale  $r$  at different redshifts for haloes of characteristic mass  $m_h = m_h^*$ . With  $\overline{K_{pv}^h}$  increasing with time, the rate of the energy cascade  $\Pi_{pv}^h$  along the halo radial direction is defined as

$$\Pi_{pv}^h(m_h, r, z) = -\frac{\partial}{\partial t} \left( \overline{K_{pv}^h} \right) = -\frac{\partial}{\partial t} \left( \frac{\Lambda_{pv}^h}{\Lambda_m^h} \right). \quad (120)$$

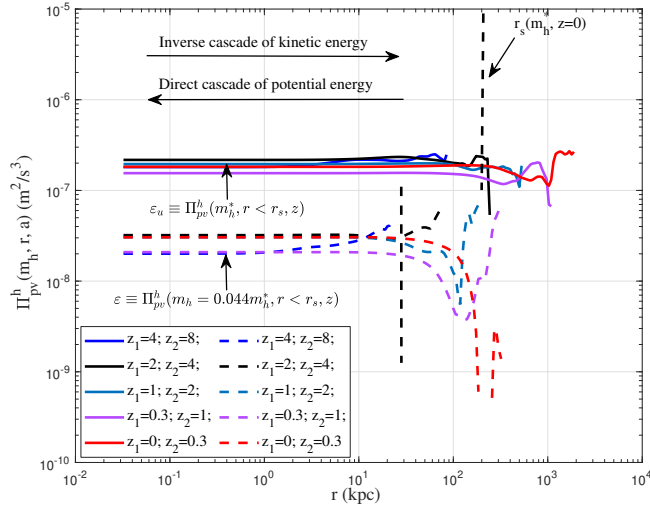


**Figure 24.** The variation of the rate of energy cascade  $\Pi_{pv}^h(m_h, r, z)$  (Eq. (99)) with radial scale  $r$  at different redshifts  $z$  for haloes of characteristic mass  $m_h^*(z)$  and  $m_h = 0.044m_h^*(z)$ . A scale-independent (independent of  $r$ ) constant rate of  $\epsilon \equiv \Pi_{pv}^h(r < r_s)$  can be identified for an inverse cascade of virial kinetic energy  $K_{pv}$  from halo center to larger scales. There also exists a simultaneous direct cascade of potential energy from large to the smallest scale at a rate of  $-7/5\epsilon$  (see Eq. (110)). For haloes with characteristic mass  $m_h^*$ , the rate of energy cascade  $\epsilon(m_h^*, z) \equiv \epsilon_u \approx 10^{-7} \text{m}^2/\text{s}^3$ .

In a certain range of scales  $r < r_s^*$  (inner haloes), the characteristic time scale on the small scale is very fast compared to the time scale on the large scale. The small-scale motion does not feel the slow large-scale motion directly, except through the rate of energy flux  $\epsilon$ . Therefore, when a statistical equilibrium is established, similarly to the energy cascade in the halo mass space, we expect a constant  $\epsilon(m_h, z)$  that is independent of scale  $r$  in the range  $r < r_s^*$ , i.e.,

$$\epsilon(m_h, z) \equiv \Pi_{pv}^h(m_h, r, z) = -\frac{\partial K_{pv}^h}{\partial t} \quad \text{for } r < r_s^*. \quad (121)$$

Figure 24 plots the variation of the parameter  $\epsilon(m_h, z)$  using Eq. (119) and the kinetic energy  $K_{pv}^h$  in Fig. 23. In this figure, a scale-independent parameter  $\epsilon$  can be clearly observed below a characteristic size  $r_s^*$ , usually the scale radius. The key parameter  $\epsilon$  increases with the halo mass  $m_h$  and the redshift  $z$ . For haloes with characteristic mass  $m_h^*$ , the rate of energy cascade  $\epsilon(m_h^*, z) \equiv \epsilon_u$ .

Similarly, we can calculate the rate of the energy cascade for haloes of different masses. Using the data in Fig. 24, Fig. 25 plots the variation of  $\epsilon(m_h, z)$  with the halo mass  $m_h$  and the redshift  $z$ . The figure shows that  $\epsilon \propto m_h^{2/3}$  and increases with redshift  $z$ ,

$$\epsilon(m_h, z) = \epsilon_u \nu = \epsilon_u (m_h/m_h^*)^{2/3} \propto m_h^{2/3} a^{-1}, \quad (122)$$

where  $\epsilon_u \equiv \epsilon(m_h^*, z)$  is the rate of energy flow in haloes of characteristic mass  $m_h^*$ . The peak height parameter of dark matter haloes is defined as  $\nu = (m_h/m_h^*)^{2/3}$  [39]. The rate of energy cascade decreases with the halo mass and time as  $\epsilon \propto m_h^{2/3} a^{-1}$  while evolving towards the limiting equilibrium. We have  $\epsilon = 0$  only in fully virialized haloes, a limiting state that real haloes can never reach.

## 12 SCALING LAWS AND HALO DENSITY PROFILES

Scaling laws are well known to be associated with the energy cascade phenomenon in turbulence [56, 57]. In this section, we focus on the

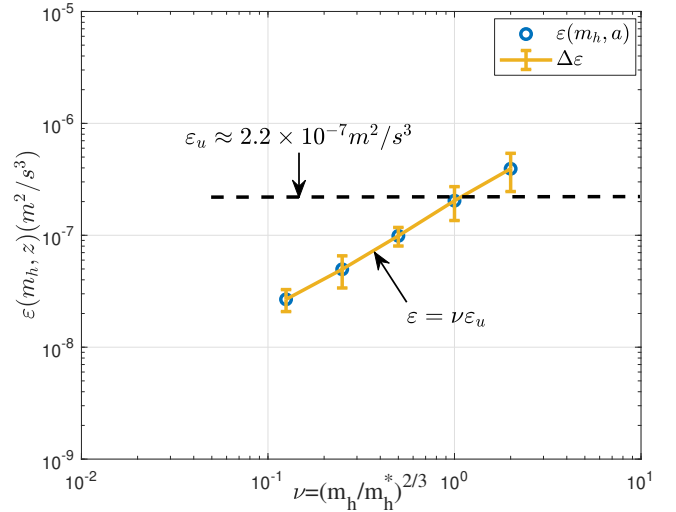


**Figure 25.** The variation of the rate of energy cascade  $\epsilon(m_h, z)$  (Eq. (99)) with halo mass  $m_h$  at different redshifts  $z$  in terms of the dimensionless peak height parameter  $\nu = (m_h/m_h^*)^{2/3}$ . A scale-independent constant rate of  $\epsilon_u$  can be identified at  $\nu = 1$  or  $m_h = m_h^*$ . That rate is also relatively independent of time and is around  $2.5 \times 10^{-7} \text{m}^2/\text{s}^3$  (also see Fig. 22).

scaling laws related to the energy cascade in spherical haloes and their effects on halo density profiles, which can be used to infer the dark matter mass and properties.

We first consider the relevant scaling laws. Here, two perspectives are presented that may lead to these scaling laws. In the first perspective, similar to the smallest two-particle haloes (Eq. (56)), the rate of the energy cascade in haloes of mass  $m_h^*$  can be written as:

$$-\epsilon_u \propto v_r^3/r = v_r^2/(r/v_r) \quad \text{or} \quad v_r^2 \propto (\epsilon_u r)^{2/3}, \quad (123)$$

where  $\epsilon_u$  is the rate of cascade in these haloes (Fig. 24),  $v_r$  is the characteristic velocity on scale  $r$ , and  $t_r = r/v_r$  is the time scale. This states that the kinetic energy  $v_r^2$  on the scale  $r$  is cascaded to large scales during a turnaround time  $t_r$ . The two-thirds law ( $v_r^2 \propto (\epsilon_u r)^{2/3}$ ) can be directly validated by N-body simulations [58]. On scale  $r$ , the virial theorem reads

$$v_r^2 \propto \frac{Gm_r}{r}, \quad (124)$$

where  $m_r$  is the mass enclosed within the scale  $r$ . Combining Eq. (123) with the virial theorem in Eq. (124), we obtain a five-thirds law for halo mass  $m_r \propto \epsilon_u^{2/3} G^{-1} r^{5/3}$  that can also be confirmed by Illustris simulations [58]. Similarly, the density enclosed within scale  $r$  should follow  $\rho_r \propto m_r/r^3 \propto \epsilon_u^{2/3} G^{-1} r^{-4/3}$ , that is, a four-thirds law for the halo density. We start with the two-thirds law,

$$-\lambda_u \epsilon_u = \frac{2v_r^2}{r} v_r = \frac{2v_r^2}{r/v_r} = \frac{2v_r^2}{t_r}, \quad (125)$$

where  $\lambda_u$  is just a dimensionless numerical constant on the order of unity. Combining Eq. (125) with the virial theorem in Eq. (124), we can easily obtain the scaling laws for mass scale  $m_r$  (mass enclosed within  $r$ ), the density scale  $\rho_r$  (mean density of the halo enclosed within  $r$ ), velocity scale  $v_r$  (circular velocity at  $r$ ), time  $t_r$ , and kinetic energy  $v_r^2$ , all determined by  $\epsilon_u$ ,  $G$  and scale  $r$ :

$$\begin{aligned} m_r &= \alpha_r \epsilon_u^{2/3} G^{-1} r^{5/3}, \quad \rho_r = \beta_r \epsilon_u^{2/3} G^{-1} r^{-4/3}, \\ v_r &\propto (-\epsilon_u r)^{1/3}, \quad t_r \propto (-\epsilon_u)^{-1/3} r^{2/3}, \\ v_r^2 &\propto (\epsilon_u G m_r)^{2/5}, \end{aligned} \quad (126)$$

where  $\alpha_r \approx 5.28$  and  $\beta_r \approx 1.26$  are two constants that can be determined by data fitting. The 2/5 scaling between kinetic energy  $v_r^2$  and halo mass  $m_r$  was also plotted in Fig. 18 and is in good agreement with the Illustris simulation. These scaling laws are for haloes with characteristic mass  $m_h^*$  and constant rate of cascade  $\varepsilon_u$ . For haloes with other masses, we replace  $\varepsilon_u$  by a mass-dependent rate of the cascade  $\varepsilon$  in Eq. (122). For example, the inner density for the haloes of mass  $m_h$  should read (-4/3 law)

$$\rho_r(r, m_h, z) = \beta_r \varepsilon^{2/3} G^{-1} r^{-4/3} = \beta_r \varepsilon_u^{2/3} G^{-1} r^{-4/3} \left( \frac{m_h}{m_h^*(z)} \right)^{4/9}. \quad (127)$$

The model predicts the halo density  $\rho_h(r) \propto m_h^{4/9} a^{-2/3}$  for halos of different masses with  $m_h^* \propto a^{3/2}$  (Table 2). In addition, scaling laws in Eq. (126) predicts a limiting density slope of  $\gamma = -4/3$  in the halo core region. Therefore, the inner structure of the haloes can be determined by the energy cascade in the haloes.

We next focus on the halo density profile. The well-known core-cusp problem describes the discrepancy between cuspy halo density predicted by cosmological CDM-only simulations and core density from observations. The predicted halo density exhibits a cuspy inner density  $\rho \propto r^\gamma$  with a wide range of  $\gamma$  between -1.0 and -1.5. The NFW profile is a very popular model with a density slope of  $\gamma = -1.0$  [59]. The density slopes of the simulated haloes are also found to be  $\gamma > -1.0$  [60],  $\gamma = -1.2$  [61], and  $\gamma = -1.3$  [62, 63]. There seems to be no consensus on the exact value of the asymptotic slope  $\gamma$  and no solid theory for the density slope  $\gamma$ .

From the mass continuity equation for a spherical halo [58], we can demonstrate that the density slope  $\gamma$  is highly dependent on the mean radial flow  $u_r(r, t)$  (flow along the radial direction) as

$$\gamma \approx \frac{\nu}{1-\mu} - 3, \quad \nu = \frac{\partial \ln m_r(r_s)}{\partial \ln r_s}, \quad \mu = \frac{u_r t}{r} \left/ \frac{\partial \ln r_s}{\partial \ln t} \right. \quad (128)$$

Here,  $r_s$  is the scale radius where the logarithmic slope is -2, and  $m_r(r_s)$  is the total mass enclosed within the scale radius  $r_s$ . The parameter  $\mu$  represents the effect of the radial flow ( $u_r$ ). A higher radial flow  $u_r$  or greater  $\mu$  leads to a smaller  $\gamma$  and a flatter density. The parameter  $\nu = 5/3$  represents the effect of the energy cascade, as we can find from the 5/3 law between  $m_r$  and  $r$  in Eq. (126).

Based on the effects of radial flow and energy cascade, we will consider the following scenarios:

(i) Individual haloes with both non-zero radial flow and non-vanishing energy cascade ( $u_r \neq 0$ ,  $\varepsilon \neq 0$ ). Most simulated haloes are non-equilibrium dynamic objects that have both a nonzero radial flow and a non-vanishing energy cascade. The density slopes of individual haloes depend on both the radial flow and the mass accretion of each halo, as shown in Eq. (128). This may be the reason for the wide variety of density slopes  $\gamma$  for simulated haloes. In previous work, we have analytically derived the halo density profiles based on the concept of a mass and energy cascade [39]. Simulated haloes with different density slopes can generally be modeled by a double- $\gamma$  density profile

$$\rho_h(r, t) = \rho_s(t) \left( \frac{r}{r_s} \right)^{\frac{\alpha}{\beta}-2} \exp \left( \frac{1}{\beta} \left( 1 - \left( \frac{r}{r_s} \right)^\alpha \right) \right), \quad (129)$$

where  $\rho_s(t)$  is the density at scale radius  $r_s(t)$ . This four-parameter double- $\gamma$  density profile ( $\rho_s$ ,  $r_s$ ,  $\alpha$ , and  $\beta$  in Eq. (129)) reduces to the standard three-parameter Einasto profile with  $\alpha = 2\beta$ .

(ii) Haloes with vanishing radial flow and non-vanishing energy cascade ( $u_r = 0$  and  $\varepsilon \neq 0$ ). Individual haloes have random radial

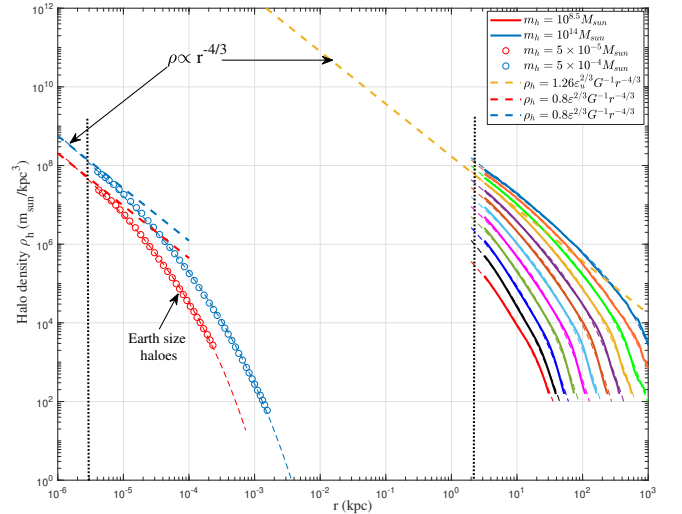


**Figure 26.** The density profiles from cosmological simulations for haloes of different mass at  $z = 0$ . The solid lines present the average density profiles for all haloes with a mass between  $10^{\pm 0.1} m_h$  from the Illustris simulation for galactic haloes of mass  $m_h = [10^{8.5} 10^{14}] M_\odot$ . The symbols present two Earth-size simulated haloes [64]. The thin dashed lines present the double- $\lambda$  density profile from Eq. (130). The thick dashed (straight) lines represent the -4/3 scaling law for haloes of mass  $m_h$  with the rate of energy cascade  $\varepsilon \propto m_h^{2/3}$  (Eq. (131)), and for haloes of characteristic mass  $m_h^*(z = 0)$  (Eq. (132)). The dotted lines indicate the softening length. The figure demonstrates the -4/3 law from the concept of energy cascade for the density profiles of haloes of different sizes over 20 orders of magnitude. The density profiles of haloes with mass  $m_h^*(z)$  at different redshifts  $z$  are presented in Fig. 28.

flow. However, in N-body simulations, we can average out radial flow by constructing composite haloes of a given mass  $m_h$  from all haloes of the same mass. This is what we did in Section 11, where relevant quantities are averaged for all haloes with the same mass. For these composite haloes, the radial flow vanishes, and we only have the effect of the energy cascade ( $\mu = 0$  and  $\nu = 5/3$  in Eq. (128)) such that the inner density slope  $\gamma = -4/3$ . The inner halo region with vanishing radial flow or  $u_r = 0$  is also expected from the stable clustering hypothesis; that is, there is no net stream motion in physical coordinate along the radial direction [65, 36]. For haloes with no radial flow, we would expect an inner density with a slope of -4/3. The corresponding double-density profile (let  $\alpha/\beta = 2/3$  in Eq. (129)) should read [39]

$$\rho_h(r, m_h, z) = \beta_r \varepsilon^{2/3} G^{-1} r_s^{-4/3} \left( \frac{r}{r_s} \right)^{-4/3} \exp \left[ -\frac{1}{\beta} \left( \frac{r}{r_s} \right)^{2\beta/3} \right], \quad (130)$$

$$\varepsilon(m_h, z) = (m_h/m_h^*(z))^{2/3} \varepsilon_u,$$

where  $\beta_r \approx 1$  is an amplitude parameter,  $\beta$  is a shape parameter, and  $r_s$  is the scale radius. Here,  $\varepsilon_u = -4.6 \times 10^{-7} m^2/s^3$  is the rate of the energy cascade for haloes with characteristic mass  $m_h^*(z)$ . While  $\varepsilon(m_h, z)$  is the rate of the energy cascade in haloes of any mass  $m_h$  (Eq. (122)). For small  $r$ , the inner density reduces to (recovers the scaling law in Eq. (127))

$$\rho_h(r, m_h, z) = \beta_r \varepsilon^{2/3} G^{-1} r^{-4/3} \quad \text{for } r \rightarrow 0, \quad (131)$$

where the redshift dependence is incorporated into  $\varepsilon$ , which is dependent on the characteristic mass  $m_h^*(z)$  (Eq. (130)). For haloes of characteristic mass  $m_h^*(z)$ , there exists a small-scale permanence for the halo density, i.e., the density profiles at different redshifts  $z$

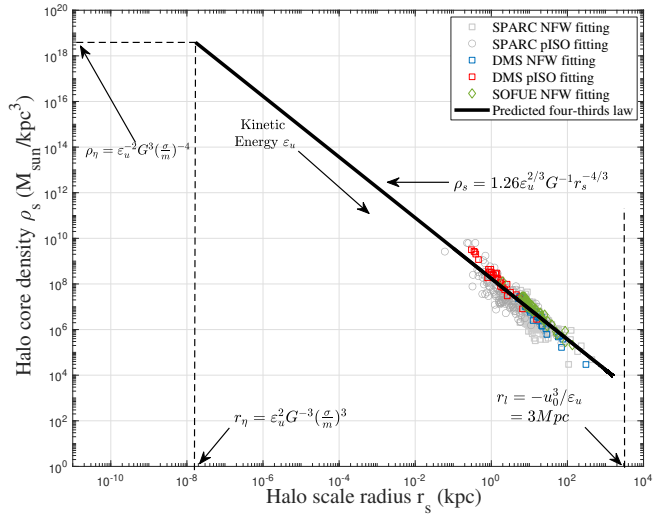


**Figure 27.** The variation of halo core density  $\rho_s$  with the halo scale radius  $r_s$  from galaxy rotation curves. Each data represents the result for a given galaxy. The predicted  $-4/3$  law in Eq. (126) is also plotted for comparison (solid black line). The good agreement confirms the predicted scaling laws from the energy cascade. For self-interacting dark matter model with a cross-section  $\sigma/m$ , there exists the smallest structure with a size  $r_\eta$  and a maximum density  $\rho_\eta$  determined by  $\varepsilon_u$ ,  $G$ , and  $\sigma/m$  (Table 5). The largest halo size  $r_l = -u_0^3/\varepsilon_u$  is determined by the velocity dispersion  $u_0$  and  $\varepsilon_u$ .

converge to a time-unvarying scaling,

$$\rho_h(r, m_h^*, z) \equiv \rho_h(r) = \beta_r \varepsilon_u^{2/3} G^{-1} r^{-4/3} \quad \text{for } r \rightarrow 0. \quad (132)$$

The small-scale permanence is shown and discussed in Fig. 28.

(iii) The last scenario is completely virialized haloes with both vanishing radial flow and vanishing energy cascade ( $u_r = 0$  and  $\varepsilon = 0$ ). This is the limiting virial equilibrium state (simulated or real) haloes evolve toward but can never reach. The  $-4/3$  density slope should still be good in this limiting state.

To validate the predicted scaling laws, we first present the density profiles from cosmological simulations for haloes of different masses  $m_h$  at  $z = 0$ . In Fig. 26, the solid lines present the average halo density profiles for all haloes with a mass between  $10^{8.1} M_\odot$  from the Illustris simulation, where  $10^8 M_\odot < m_h < 10^{14} M_\odot$ . The symbols present two Earth-size simulated haloes with a mass of  $5 \times 10^{-5} M_\odot$  and  $5 \times 10^{-4} M_\odot$ , respectively [64]. The thin dashed lines present the double- $\lambda$  density profile from Eq. (130). The thick dashed (straight) lines represent the  $-4/3$  scaling laws for haloes of mass  $m_h$  that involve the rate of cascade  $\varepsilon \propto m_h^{2/3}$  (Eq. (131)). Here,  $\varepsilon = \varepsilon_u$  for haloes of characteristic mass  $m_h^*$  (Eq. (132)). The figure demonstrates the  $-4/3$  law that we obtained from the concept of energy cascade. That scaling was in agreement with the density profiles of haloes of more than 20 orders of magnitude.

Observational evidence of the predicted scaling laws also exists. The four-thirds law  $\rho_r(r) \propto r^{-4/3}$  for the halo mass density enclosed within the scale  $r$  can also be directly compared against data from galaxy rotation curves (Fig. 27). Important information for dark matter haloes can be extracted from galaxy rotation curves by decomposing them into contributions from different mass components. Once the halo density model is selected, the scale radius  $r_s$  and the mean density  $\rho_s$  within  $r_s$  can be rigorously obtained by fitting the decomposed rotation curve. In this work, for pseudo-isothermal (pISO) models [66] and NFW density models [59], three different

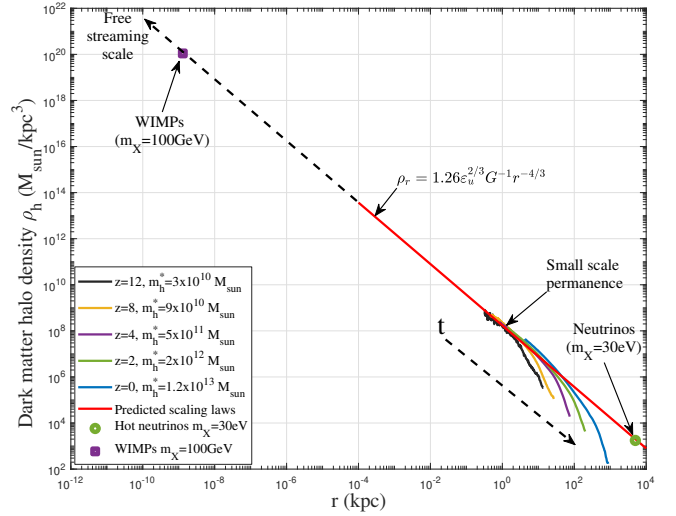


**Figure 28.** The redshift evolution of halo density profiles for haloes with a characteristic mass  $m_h^*(z)$ . Density profiles for haloes with other masses (from the galaxy cluster to the Earth size) are presented in Fig. 26. This figure demonstrates the small-scale permanence, i.e., the density profiles for haloes with a characteristic mass  $m_h^*(z)$  at different redshifts  $z$  all collapse at a small scale  $r$  onto the predicted time-unvarying scaling (solid red line from Eq. (132)). Due to the time and scale-independent rate of the cascade  $\varepsilon_u$ , the  $-4/3$  scaling should extend to smaller scales (or earlier time) until reaching the smallest scale (or the formation time of the smallest structures) that depends on the nature of dark matter (Sections 2). The halo mass, density, size, and formation time at the smallest scale are calculated in Eq. (133). Two examples, hot neutrinos ( $m_X=30\text{eV}$ ) and WIMPs ( $m_X=100\text{GeV}$ ) are plotted in the same figure and listed in Table 3.

sources of rotation curves are used to extract  $r_s$  and density  $\rho_s$  within  $r_s$ ,

- (i) SPARC (Spitzer Photometry & Accurate Rotation Curves) including 175 late-type galaxies [67, 68];
- (ii) DMS (DiskMass Survey) including 30 spiral galaxies [69];
- (iii) SOFUE (compiled by Sofue) with 43 galaxies [70].

Figure 27 presents the variation of the halo core density  $\rho_s$  with the scale radius  $r_s$  obtained from the galaxy rotation curves (square and circle symbols). Each symbol represents data from a single galaxy. The four-thirds law (Eq. (126)) is also plotted (black line) with constants  $\beta_r = 1.26$  (equivalent to  $\alpha_r = 5.28$ ) obtained from these data. From this figure, dark matter haloes from galaxy rotation curves follow the  $-4/3$  law across six orders of halo mass.

Finally, we are especially interested in the redshift evolution of haloes with a characteristic mass  $m_h^*(z)$ , which is representative. Figure 28 shows the time evolution of the average density profiles for all haloes with characteristic masses  $m_h^*(z)$  from Illustris simulations. By averaging out the radial flow, the energy cascade should give rise to a slope of  $\gamma = -4/3$  (Eq. (128)). At higher redshifts, dark matter haloes tend to be smaller with higher density. The density profiles of all dark matter haloes converge to the predicted time-unvarying scaling (solid red line) from Eq. (132), i.e., the small-scale permanence that can be confirmed by N-body simulations.

The  $-4/3$  scaling law in Fig. 28 should extend to smaller and smaller scales until the scale of the smallest halo. That scale can be the free streaming scale, which is dependent on the nature and mass of dark matter particles (Sections 2). The heavier particles have a smaller free streaming scale. For sufficiently heavy DM particles of mass  $m_{Xc} \approx 10^{12} \text{GeV}$ , the free streaming mass can be comparable



**Table 3.** Dark matter particle candidates and the free streaming scale

Quantities	Symbol	Hot neutrinos	WIMPs	X particle
Particle mass	$m_X$	30eV	100GeV	$10^{12}$ GeV
Free streaming	$M_{fs}$	$10^{15}M_\odot$	$10^{-6}M_\odot$	$10^{12}$ GeV
Size	$r_{fs}$	5Mpc	$10^{-9}$ kpc	$10^{-13}$ m
Density	$\rho_{fs}$	$10^{-25}$ kg/m <sup>3</sup>	$10^{-8}$ kg/m <sup>3</sup>	$10^{23}$ kg/m <sup>3</sup>
Formation time	$t_{fs}$	$10^{11}$ yrs	300yrs	$10^{-6}$ s

to the particle mass (Fig. 2) such that the  $-4/3$  scaling can extend to the scale of the smallest structure (two-particle haloes). Since smaller structures were formed earlier (as early as the radiation era in Section 4), extending to smaller scales is equivalent to extending to an earlier time. For dark matter candidates with known free streaming mass  $M_{fs}$ , scaling laws in Eq. (126) can be used to calculate the relevant quantities for the smallest structure of the free streaming scale,

$$\begin{aligned} r_{fs} &= \alpha_r^{-3/5} \varepsilon_u^{-2/5} G^{3/5} M_{fs}^{3/5}, \\ \rho_{fs} &= \beta_r \alpha_r^{4/5} \varepsilon_u^{6/5} G^{-9/5} M_{fs}^{-4/5}, \\ t_{fs} &= \varepsilon_u^{-3/5} G^{2/5} M_{fs}^{2/5}, \end{aligned} \quad (133)$$

where  $r_{fs}$ ,  $\rho_{fs}$ , and  $t_{fs}$  are the size, density, and formation time of the smallest haloes with a free streaming mass  $M_{fs}$ .

In Fig. 28, two examples are presented, that is, the hot neutrinos with  $M_{fs} = 10^{15}M_\odot$  (green dot) and standard WIMPs with  $M_{fs} = 10^{-6}M_\odot$  (purple square). Table 3 lists the relevant quantities calculated for the smallest halo structure formed by three dark matter candidates. The particle  $X$  with critical mass  $m_X = M_{fs} = 10^{12}$  GeV was also listed, which has been extensively discussed in Sections 2 and 4 (Eq. (55)). Obviously, the cold dark matter (WIMPs and  $X$ ) leads to much smaller structures formed in the earlier universe. Finally, at what scale should the  $-4/3$  scaling stop operating strongly suggests the nature of dark matter particles (Section 13).

### 13 DARK MATTER PARTICLE MASS AND PROPERTIES

In this section, we attempt to estimate the mass and properties of the cold dark matter particles from the established scaling laws in Section 12. Since the rate of the energy cascade  $\varepsilon_u$  in Eq. (111) is both scale- and time-independent, the scaling laws should extend to the smallest scale (Fig. 28) and the earliest time when the smallest structure was formed, as early as in the radiation era (Section 4). Here, we consider  $X$  particles with a mass  $m_X \geq m_{Xc}$ , or the free streaming mass is less than the particle mass (Fig. 2). In this case, the free streaming scale is not relevant, and the smallest structures formed can be two-particle haloes. The highest possible density of the two-particle haloes cannot be infinite and is limited by the uncertainty principle such that the scaling laws may extend to a scale where quantum effects become important. For particles with a mass  $m_X \ll m_{Xc}$ , the smallest haloes are determined by the free streaming mass (Eq. (133)).

Assuming that gravity is the only interaction between unknown dark matter particles (traditionally denoted by  $X$ ), the only dominant physical constants on the smallest scale are the reduced Planck constant  $\hbar$  (the quantum effect), the gravitational constant  $G$  (the gravitational interactions) and the rate of energy cascade  $\varepsilon_u$ . Without involving complex quantum field theory for a more rigorous treatment, a formal dimensional analysis often provides significant insights. Any physical quantities  $Q$  on that scale can be expressed as  $Q = \varepsilon_u^x G^y \hbar^z$ , where  $x$ ,  $y$ , and  $z$  can be uniquely determined by

dimensional analysis. Examples are the mass and length scales,

$$m_X = \left( -\varepsilon_u \hbar^5 G^{-4} \right)^{\frac{1}{9}} \quad (134)$$

and

$$l_X = \left( -\varepsilon_u^{-1} G \hbar \right)^{\frac{1}{3}}. \quad (135)$$

Alternatively, the same results can be obtained from a refined treatment to couple relevant physical laws on the smallest scale. This may offer a complete view than a simple dimensional analysis. Let us consider two  $X$  particles on the smallest scale with separation  $2r_X = l_X$  in the rest of the center of mass of two particles. On that scale, three relevant physics are as follows:

$$m_X V_X \cdot l_X / 2 = \hbar, \quad (136)$$

$$G m_X / l_X = 2V_X^2, \quad (137)$$

$$2V_X^3 / l_X = a_X \cdot v_X = -\lambda_u \varepsilon_u, \quad (138)$$

where Eq. (136) is from the uncertainty principle for momentum and position if  $X$  particles exhibit wave-particle duality. Equivalently, we can also treat  $l_X/2$  as the de Broglie wavelength of the matter wave of  $X$  particle. Equation (137) is from the virial theorem for the potential energy ( $V$ ) and the kinetic energy ( $T$ ), that is,  $2T = -V$ . Here,  $V_X$  is the relative velocity between two particles due to their interactions and contributes to the small-scale virial kinetic energy  $K_{pv}$ . The last equation (138) is from the two-thirds (2/3) law in Eq. (125) associated with the energy cascade in dark matter reflecting the "uncertainty" principle between particle acceleration and velocity [58]. Since the energy cascade rate  $\varepsilon_u$  is both scale- and time-independent, we may extend the 2/3 law down to the smallest scale for dark matter particle properties. By this approach, the dark matter particle properties on small scales are consistent with the established scaling laws for dynamics of dark matter haloes on large scales. With the following values for three constants,

$$\begin{aligned} \varepsilon_u &= -4.6 \times 10^{-7} m^2/s^3, \\ \hbar &= 1.05 \times 10^{-34} kg \cdot m^2/s, \\ G &= 6.67 \times 10^{-11} m^3/(kg \cdot s^2), \end{aligned} \quad (139)$$

Complete solutions of Eqs. (136), (137), and (138) can be obtained (with  $\lambda_u = 1$ ), relevant quantities on the  $X$  scale are (Fig. 29),

$$m_X = \left( -\frac{256 \lambda_u \varepsilon_u \hbar^5}{G^4} \right)^{\frac{1}{9}} = 1.62 \times 10^{-15} kg \approx 10^{12} GeV, \quad (140)$$

$$l_X = \left( -\frac{2G\hbar}{\lambda_u \varepsilon_u} \right)^{\frac{1}{3}} = 3.12 \times 10^{-13} m, \quad (141)$$

$$t_X = \frac{l_X}{V_X} = \left( -\frac{32G^2\hbar^2}{\lambda_u^5 \varepsilon_u^5} \right)^{\frac{1}{9}} = 7.51 \times 10^{-7} s,$$

$$V_X = \left( \frac{\lambda_u^2 \varepsilon_u^2 \hbar G}{4} \right)^{\frac{1}{9}} = 4.16 \times 10^{-7} m/s, \quad (142)$$

$$a_X = \left( -\frac{4\lambda_u^7 \varepsilon_u^7}{\hbar G} \right)^{\frac{1}{9}} = 1.11 m/s^2.$$

Note that the solutions of mass  $m_X$  and length scale  $l_X$  agree with those obtained from a formal dimensional analysis in Eqs. (134) and (135). The predicted particle mass is much heavier than standard

WIMPs and is of the same order as the critical mass  $m_{Xc}$  in Eq. (14). Therefore, the corresponding free streaming mass for particles of this mass should be comparable to the particle mass, allowing us to extend the scaling laws to the particle mass scale.

The time scale  $t_X$  (formation time of the smallest structures) is close to the characteristic time for weak interactions ( $10^{-6} \sim 10^{-10}s$ ). In contrast, the length scale  $l_X$  is greater than the characteristic range of strong interactions ( $\sim 10^{-15}m$ ) and weak interactions ( $\sim 10^{-18}m$ ). The "thermally averaged cross section" of  $X$  particle is around  $l_X^2 V_X = 4 \times 10^{-32} m^3/s$ . This is on the same order as the cross-section required for the correct abundance of today via thermal production ("WIMP miracle"), where  $\langle\sigma v\rangle \approx 3 \times 10^{-32} m^3 s^{-1}$ . The "cross section  $\sigma/m$ " for  $X$  particle is extremely small, i.e.  $l_X^2/m_X = 6 \times 10^{-11} m^2/kg$ , i.e., a fully collisionless dark matter. In addition, a new constant  $\mu_X$  (the scale for the rate of energy dissipation) can be introduced,

$$\mu_X = m_X a_X \cdot V_X = F_X \cdot V_X = -m_X \varepsilon_u$$

$$= \left( -\frac{256 \varepsilon_u^{10} \hbar^5}{G^4} \right)^{\frac{1}{9}} = 7.44 \times 10^{-22} kg \cdot m^2/s^3 \quad (143)$$

which is a different representation of  $\varepsilon_u$ . In other words, the fundamental physical constants on the smallest scale can be  $\hbar$ ,  $G$ , and the constant  $\mu_X$ . Consequently, an important energy scale is set by

$$E_X = \mu_X t_X / 4 = \hbar / t_X = \sqrt{\hbar \mu_X} / 2 = 0.87 \times 10^{-9} \text{eV}. \quad (144)$$

This energy scale is the binding energy of two  $X$  particles in the ground state (Eq. (55)). It is equivalent to a Compton wavelength of 1.4 km or a frequency of 0.2 MHz. This can be relevant to the possible dark "radiation" (Section 15).

The relevant mass density is around  $m_X / l_X^3 \approx 5.33 \times 10^{22} kg/m^3$ , much higher than the nuclear density of the order of  $10^{17} kg/m^3$  (Fig. 30). This density is about  $32\pi^2$  times the background density of the universe at the formation time  $t_X$ , in agreement with the spherical collapse model. The relevant pressure scale is

$$P_X = \frac{m_X a_X}{l_X^2} = \frac{8\hbar^2}{m_X} \rho_{nX}^{5/3} = 1.84 \times 10^{10} Pa, \quad (145)$$

which sets the highest pressure or the possible "degeneracy" pressure of dark matter that stops further gravitational collapse. Equation (145) is an analog of the degeneracy pressure of the ideal Fermi gas, where  $\rho_{nX} = l_X^{-3}$  is the number density of the particle  $X$ . With today's dark matter density around  $2.2 \times 10^{-27} kg/m^3$  and local density  $7.2 \times 10^{-22} kg/m^3$ , the mean separation between  $X$  particles is about  $l_u \approx 10^4 m$  in the entire universe and  $l_c \approx 130 m$  locally.

In summary, Fig. 29 presents a detailed interpretation. Different combinations of three relevant physics leads to some interesting findings in Fig. 29. Combining Eq. (136) with Eq. (137) leads to the black dashed line in Fig. 29, a relation between the mass and size of the particles ( $m_r \propto r^{-1/3}$ ). A similar relation can also be obtained from the Schrödinger-Newton equation, a nonlinear modification of the Schrödinger equation with Newtonian gravity for self-interaction. This line represents the boundary below which quantum effects are important and dominant over gravity.

Combining Eq. (138) with Eq. (137) leads to the five-thirds ( $m_r \propto r^{3/5}$ ) law between the halo mass and the halo size (see Eq. (126) for the 5/3 law), the blue dashed line in Fig. 29. Dark matter haloes from galaxy rotation curves also fall on the same line. This line represents the dynamics of dark matter haloes on large scales. To find the dark matter particle properties that are consistent with the dynamics of dark matter haloes on large scales, extending the five-thirds law (blue

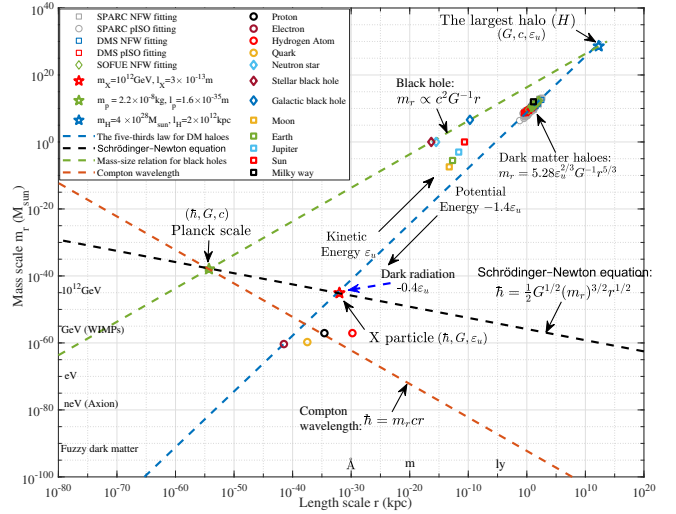


**Figure 29.** The variation of mass scale  $m_r$  and size scale  $r$  for cold dark matter particle properties. This figure estimates the cold dark matter particle properties on small scales that are consistent with the dynamics of dark matter haloes on large scales. Collisionless dark matter haloes follow the scaling  $m_r \propto r^{5/3}$  (the blue dashed line for the five-thirds law in Eq. (126)) due to the energy cascade at a constant rate  $\varepsilon_u$  for kinetic energy and  $-1.4\varepsilon_u$  for potential energy (Eq. (110) and Fig. 21). Dark matter haloes from different surveys of galaxy rotation curves in Fig. 27 follow the five-thirds law. The black dashed line represents the combined quantum and gravitational effects of Eqs. (136) and (137). The green dashed line gives the mass of black holes (BHs) at a given size  $r$  (Schwarzschild radius) from stellar to galactic BHs, i.e., the maximum mass at any given  $r$ . By extending the five-thirds law (blue dashed line) for dark matter haloes to the smallest scale (intersecting the black dashed line), the red star represents the cold dark matter particles ( $X$ ) with predicted mass  $m_X$  and size  $l_X$  from Eqs. (134) and (135) (also see Table 4). By extending the five-thirds law (blue dashed line) for dark matter haloes to the largest scale to intersect the green dashed line (the blue star), we will obtain the largest scales (the  $H$  scale) of halo size ( $l_H$ ), mass ( $m_H$ ), and time ( $t_H$  or DM lifetime  $\tau_X$  in Eq. (146)) (see table 4). The green star represents the Planck scale. For comparison, the mass and size of some particles and astronomical objects are also shown.

**Table 4.** Physical quantities on the  $X$  scale, the  $H$  scale and the Planck scale

Scales	The $X$ scale	The $H$ scale	The Planck scale
Length	$l_X = \left( -\frac{G\hbar}{\varepsilon_u} \right)^{1/3}$	$l_H = -\frac{c^3}{\varepsilon_u}$	$l_P = \sqrt{\frac{\hbar G}{c^3}}$
Time	$t_X = \left( -\frac{G^2 \hbar^2}{\varepsilon_u^5} \right)^{1/9}$	$t_H = -\frac{c^2}{\varepsilon_u}$	$t_P = \sqrt{\frac{\hbar G}{c^5}}$
Mass	$m_X = \left( -\frac{\varepsilon_u \hbar^5}{G^4} \right)^{1/9}$	$m_H = -\frac{c^5}{\varepsilon_u G}$	$m_P = \sqrt{\frac{\hbar c}{G}}$

dashed) to the smallest scale will intersect the black dashed line, i.e., the red star in Fig. 29, where quantum effect becomes relevant, and scaling laws might stop operating. This should be the scale of the  $X$  particle (the  $X$  scale). We show that the free streaming mass is comparable to the particle mass at this scale (Eq. (14)).

Finally, the mass of black holes at a given size  $r$  (Schwarzschild radius) is plotted as a green dashed line ( $m_r \propto r$ ). This is the maximum mass  $m_r$  on a given scale  $r$ . Extending the green dashed line to intersect the blue dashed line, i.e., the blue star leads to the largest scale (the  $H$  scale) of dark matter haloes. This is, of course, the largest possible scale of dark matter haloes that can be reached during the lifetime of dark matter. The black dashed line intersects the green dashed line on the Planck scale.

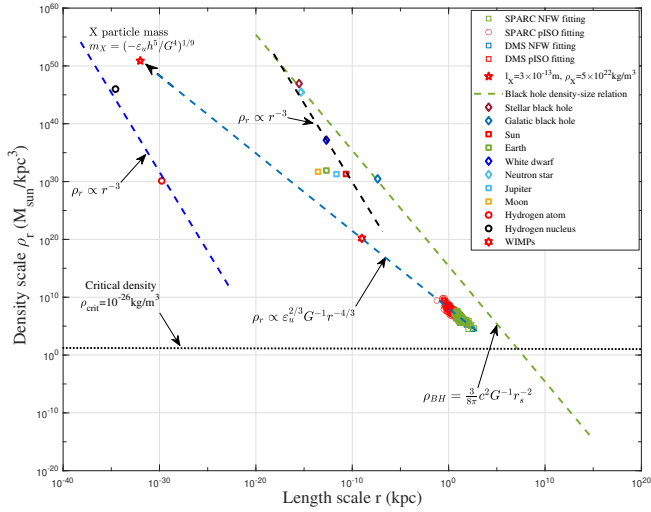


**Figure 30.** The variation of density scale  $\rho_r$  with size scale  $r$  for cold dark matter particle properties. By extending the four-thirds law in Fig. 27 for dark matter haloes to the smallest scale where quantum effects are dominant, the red star (the  $X$  scale) represents the cold DM particles with predicted density  $\rho_X$  and size  $l_X$  from Eqs. (134) and (135). Collisionless dark matter haloes follow the scaling  $\rho_r \propto r^{-4/3}$  due to the energy cascade at a constant rate  $\varepsilon_u$ . The densities of sun, dwarf, neutron star, and stellar black hole follow the scaling  $\rho_r \propto r^{-3}$  reflecting the formation of stellar black holes from the collapse of massive stars. The density of black holes ( $\rho_{BH}$ ) as a function of Schwarzschild radius ( $r_s$ ) follows  $\rho_{BH} \propto r_s^{-2}$ , extending from stellar to galactic black holes. WIMPs from Table 3 is also reported (red hexagram).

In this plot, three key scales (Table 4) are determined by different constants, i.e., the green star for the Planck scale ( $\hbar$ ,  $G$ , and  $c$ ), the red star for the smallest halo scale or the DM particle scale  $X$  ( $\hbar$ ,  $G$ , and  $\varepsilon_u$ ), and the blue star for the largest halo scale  $H$  ( $G$ ,  $c$ , and  $\varepsilon_u$ ). Table 4 provides relevant quantities on three key scales. For comparison, the mass and actual size of some typical particles and astronomical objects are also presented in the same figure.

Similarly, Figure 30 illustrates the variation of the density scale  $\rho_r$  with size  $r$ . By extending the four-thirds law in Fig. 27 to the smallest scale where the quantum effect becomes dominant, we obtain the red star in Fig. 30 for cold DM particles with predicted mass  $m_X$  and size  $l_X$  from Eqs. (134) and (135). The density and size of some typical particles and astronomical objects are also included for comparison. As expected, the density of the sun, dwarf, neutron star, and stellar black hole follows the scaling  $\rho_r \propto r^{-3}$ , while the density of black holes ( $\rho_{BH}$ ) computed using the Schwarzschild radius ( $r_s$ ) follows a simple scaling  $\rho_{BH} \propto r_s^{-2}$ . Thus, Fig. 30 displays three distinct scaling laws for density-size relations of different objects reflecting different operating physics, i.e.  $\rho_r \propto r^{-4/3}$  for dark matter haloes,  $\rho_r \propto r^{-3}$  for the formation of stellar black holes, and  $\rho_r \propto r^{-2}$  for black holes (BH) of different sizes from stellar to galactic.

## 14 THE NATURE OF COLD DARK MATTER

Previous analysis on the free streaming mass, the structure formation and evolution, energy cascade, and dark matter halo density profiles strongly suggests a critical particle mass of  $10^{12}$  GeV. This prediction is well beyond the mass range of standard thermal WIMPs but in the range of the so-called superheavy dark matter (SHDM). If gravity is the only interaction between the Standard Model and the dark sectors, these superheavy particles have also been dubbed

as Planckian-interacting massive particles (PIDM) [71]. Except for what we discussed in this work, there are other good motives for considering such superheavy dark matter particles. Since the instability of the electroweak Higgs vacuum can also be linked to an energy scale on the same order of  $10^{12}$  GeV [72, 73], our predicted mass scale approaches the energy scale at which new physics might emerge. Note that the prediction of such a superheavy DM mass does not rely on the details of the dark matter production mechanism. Though this scale is out of the reach of any current experiment, in this section, we can still briefly explore the possible options for the nature of the dark matter of this critical mass.

There is a wide range of possible candidates. One potential mechanism can be the production of gravitational particles in quintessential inflation [74, 75]. The nonthermal relics from gravitational production do not have to be in the local equilibrium in early universe or obey the unitarity bounds for thermal WIMPs. To have the right abundance generated during inflation, these nonthermal relics should also have a mass range between  $10^{12}$  and  $10^{16}$  GeV [76, 77]. The other possible superheavy dark matter candidate is the Crypton in string or M theory with a mass around  $10^{12}$  GeV to give the right abundance [78, 79]. Detection methods for superheavy dark matter have also been discussed in the literature [80, 81].

Another very interesting option can be superheavy sterile neutrinos (or heavy neutral leptons) [82]. Such right-handed neutrinos can have a “Majorana mass” term that is not related to the Higgs field. This seems like a very attractive option from “Occam’s razor” viewpoint: one tries to minimize the number of assumptions introduced but maximize the number of problems that can be addressed simultaneously. The minimal assumption we make is the existence of superheavy sterile neutrinos with a mass around  $10^{12}$  GeV. From the seesaw mechanism and without any fine-tuning, the Yukawa couplings of these superheavy sterile neutrinos should be of the order of one to obtain the correct active sub-eV (left-handed) neutrino mass [82]. In addition, the baryon asymmetry of the Universe can also be realized through thermal leptogenesis [83]. In principle, the existence of such superheavy sterile neutrinos of mass  $10^{12}$  GeV can account for neutrino oscillations, dark matter, and baryon asymmetry at the same time and potentially stabilizes the electroweak vacuum. In addition, axion dark radiation associated with the structure formation of these particles might also be helpful in solving the strong CP problem (Section 15).

Instead of decaying into SM particles such as (anti-) protons, neutrons, and photons, here we consider a slow instanton-induced decay process, where  $X$  particles decay into a dark radiation field with an energy on the order of  $E_X \approx 10^{-9}$  eV (Eq. (144)). In this scenario, the lifetime required for a complete decay of a single  $X$  particle can be estimated both from [71] and from this work as

$$\tau_X = \frac{\hbar e^{4\pi/\alpha_X}}{m_X c^2} \quad \text{and} \quad \tau_X = \frac{m_X c^2}{\mu_X} = -\frac{c^2}{\varepsilon_u}, \quad (146)$$

where the  $\alpha_X$  is the reduced coupling constant of the hidden gauge interaction and  $\varepsilon_u \approx -10^{-7} m^2/s^3$  is the rate of energy cascade. The lifetime  $\tau_X \approx 2 \times 10^{23} s = 6.2 \times 10^{15}$  yrs is much greater than the age of our universe. By equating two expressions, the coupling constant of this scenario is estimated to be  $\alpha_X \approx 4\pi/137 \approx 0.092$  from Eq. (146) that is in good agreement with the prediction of  $\alpha_X$  in [71].

## 15 AXION AND GRAVITATIONAL WAVE RADIATION

In this section, in analogy to the phonon radiation in superfluid turbulence with vanishingly small viscosity [84], dark radiation is

postulated for collisionless dark matter flow. As the binding energy of the smallest two-particle halo structures (Eq. (55)), the energy scale  $E_X \approx (\epsilon_u^5 \hbar^7 G^{-2})^{1/9} = 10^{-9} \text{eV}$  (Eq. (144)) strongly suggests the existence of a dark radiation field that is coupled to the  $X$  particles of mass  $10^{12} \text{GeV}$ . This dark "radiation" may originate from the non-relativistic dark matter particles migrating in a non-uniform gravitational potential in haloes [40], which is produced along with the halo structure formation and evolution. The rate of energy produced as dark radiation should balance the total energy cascaded to the smallest scale (the  $X$  scale in Fig. 29) at a rate of  $-0.4\epsilon_u$ . This is the sum of the rate of the energy cascade for the kinetic energy at a rate of  $\epsilon_u$  and the potential energy at a rate of  $-1.4\epsilon_u$  from the energy evolution of the  $N$ -body system (Eq. (110)).

Although the nature of this dark "radiation" is not yet clear, two possible options can be identified. Since gravity is the only interaction involved, the first and the most natural option is the gravitational waves (GW or gravitons in quantum field theory). Based on the binding energy of  $10^{-9} \text{eV}$ , the gravitational wave of 200 kHz or a wavelength of 1.4 km was produced due to the structure formation in the earlier universe (Eq. (55)). This high-frequency gravitational wave is potentially detectable by a Levitated Sensor Detector [85] or other approaches.

Axion is another interesting option. It is well known that axion with a Compton wavelength of the order of black hole size can be exponentially produced through superradiance, forming a "gravitational atom" and producing a coherent, monochromatic gravitational wave (GW) radiation. In our case, axion of mass  $10^{-9} \text{eV}$  has a Compton wavelength of 1.4 km that is comparable to the stellar black hole size. A coherent high-frequency GW radiation of 200 kHz may be produced through BH superradiance and potentially detected on Earth. In principle, axion can be produced by a dynamic gravitational field that introduces a time-dependent perturbation to the spacetime metric. For axion field in a dynamic gravitational field, the rapid varying spacetime metric acts as a driving force, exciting the field and producing axions. In our case, the rapid varying metric with a period of  $10^{-6} \text{s}$  induced by two superheavy dark matter particles approaching on a short distance of  $10^{-13} \text{m}$  (Eq. (55)) may be sufficient to excite the axion field and produce nano-eV axions of a 100 kHz frequency. These axions should be produced around the time  $t_X \approx 10^{-6} \text{s}$  (Eq. (141)), coincident with the QCD phase transition time, when the earliest and smallest structures (two-particle haloes) formed. The mass of axion is on the order of the energy scale  $E_X \sim 10^{-9} \text{eV}$  (Eq. (144)) and satisfies the uncertainty principle  $t_X E_X \approx \hbar$ . Or equivalently, the mass should only be obtained when the Hubble rate is sufficiently small and below that mass. The formation of halo structure at the predicted time  $t_X \approx 10^{-6} \text{s}$  might also hint at symmetry breaking and mass generation during the QCD phase transition [86]. These properties suggest that the axion may be a very promising candidate of our dark radiation with small mass and weak interaction with Standard Model particles [29, 30].

In this section, we will take the axion as a candidate and estimate its properties. If the axion is the candidate for dark "radiation," it should have a mass on the order of  $m_a \sim E_X = 10^{-9} \text{eV}$ . Since the axion mass is closely related to the decay constant  $f_a$  according to equation [86],

$$m_a = (5.70 \pm 0.007) \times 10^{-6} \text{eV} \left( \frac{10^{12} \text{GeV}}{f_a} \right). \quad (147)$$

This leads to a GUT (grand unification energy) energy scale at which the Peccei-Quinn (PQ) symmetry is spontaneously broken, i.e.,  $f_a \approx 6.5 \times 10^{15} \text{GeV}$ . The axion particle with these properties should gain its mass at a critical temperature of  $T_1 \approx 230 \text{ MeV}$  during the quark

**Table 5.** Physical scales for cold collisionless and self-interacting dark matter

Scales	Fully collisionless	Self-interacting
Length	$l_X = (-G\hbar/\epsilon_u)^{1/3}$	$r_\eta = \epsilon_u^2 G^{-3} (\sigma/m)^3$
Time	$t_X = (-G^2 \hbar^2 / \epsilon_u^5)^{1/9}$	$t_\eta = -\epsilon_u G^{-2} (\sigma/m)^2$
Mass	$m_X = (-\epsilon_u \hbar^5 / G^4)^{1/9}$	$m_\eta = \epsilon_u^4 G^{-6} (\sigma/m)^5$
Density	$\rho_X = (\epsilon_u^{10} \hbar^{-4} / G^{13})^{1/9}$	$\rho_\eta = \epsilon_u^{-2} G^3 (\sigma/m)^{-4}$

epoch, corresponding to the time of  $t_X = 10^{-6} \text{s}$ . The coupling of the QCD axion to SM particles is inversely proportional to  $f_a$ , leading to an extremely weak coupling to photons with an effective coupling constant  $g_{a\gamma\gamma} \sim 10^{-18} \text{GeV}^{-1}$ . This is beyond the range of the current direct search for the axion [87] but should be covered within the next decade.

## 16 SELF-INTERACTING DARK MATTER

Note that the particle mass  $m_X$  is only weakly dependent on  $\epsilon_u$  as  $m_X \propto \epsilon_u^{1/9}$  (Eq. (140)) such that the estimation of  $m_X$  should be fairly robust for a wide range of possible values of  $\epsilon_u$ . A small change in  $m_X$  requires a large change in  $\epsilon_u$ . Unless gravity is not the only interaction, the uncertainty in the predicted  $m_X$  should be small. In other words, if our estimate ( $\epsilon_u$  in Eq. (111)) is accurate and gravity is the only interaction on the smallest scale, it seems implausible for dark matter particles with any mass far above  $10^{12} \text{GeV}$  to produce the given value of the energy cascade rate  $\epsilon_u \approx 10^{-7} m^2/s^3$ . If the mass of dark matter particles has a different value, there might be some new interactions beyond gravity. This can be the self-interacting dark matter (SIDM) model as a potential solution for the "cusp-core" problem [22].

For self-interacting dark matter, a key parameter is the cross-section  $\sigma/m$  (in the unit:  $\text{m}^2/\text{kg}$ ) of self-interaction that can be constrained by various astrophysical observations. Self-interaction introduces an additional scale, below which self-interaction is dominant over gravity to suppress all small-scale structures, and the scaling laws for dark matter haloes in Section 12 are no longer valid. In this case, the dark matter particle properties can be obtained only if the nature and dominant constants of self-interaction are known. Three constants determine the smallest scale for the existence of a halo structure, that is, the rate of the energy cascade  $\epsilon_u$ , the gravitational constant  $G$ , and the cross-section  $\sigma/m$ . In other words, the cross-section might be estimated if the scale of the smallest structure is known. Table 5 lists the relevant scales for both collisionless and self-interacting dark matter. Taking the value of  $\sigma/m = 0.01 \text{m}^2/\text{kg}$  used for the cosmological SIDM simulation to reproduce the right halo core size and central density [88], these scales are also plotted in Fig. 27. More insights can be obtained by extending the current analysis to self-interacting dark matter simulations.

## 17 CONCLUSIONS

In this paper, we have discussed the nonlinear halo structures formation and evolution in different eras. A critical mass scale  $m_{Xc}$  is identified on the order of  $10^{12} \text{GeV}$ . Dark matter particles seem to prefer to have a mass of that critical mass because i) particles of this mass can form the smallest and earliest possible structure (Fig. 2); ii) particles of this mass can have a direct collision time comparable to the formation time. This allows for the formation of the smallest



and earliest two-particle haloes by direct collisions (Eq. (54)); iii) particles of this mass have the shortest possible waiting time to allow for the formation of haloes observed today as large as  $10^{13} M_{\odot}$  (Eq. (67)). Particles smaller than  $m_{Xc}$  will not have enough time to grow haloes of that size. In particular, iv) particles of this mass give rise to the key parameter  $\varepsilon_u$  (Eq. (56)) that influences the halo dynamics and density profiles, which is consistent with N-body simulations and observations. The rapid growth of halo structures in the radiation and matter eras eventually slows down due to the self-limiting effects in the dark energy era (Table 2).

We identified the mass and energy cascade for the cold and collisionless dark matter within the  $\Lambda$ CDM cosmology, which operates in all eras. The concept was demonstrated by Illustris simulations. The energy cascade leads to a two-thirds law for kinetic energy or, equivalently, to five-thirds and four-thirds laws for halo mass and halo density (Eq. (126)). All scaling laws can be confirmed by cosmological N-body simulations and galaxy rotation curves. For collisionless dark matter, viscosity is not present, and gravity is the only interaction such that the established scaling laws on halo scales can be extended to the smallest scale, where quantum effects become important. The dominant constants on that scale include the rate of the energy cascade  $\varepsilon_u$ , the Planck constant  $\hbar$ , and the gravitational constant  $G$ . Cold dark matter particles were proposed to have a mass  $m_X = (\varepsilon_u \hbar^5 G^{-4})^{1/9} = 0.9 \times 10^{12}$  GeV, a size  $l_X = (\varepsilon_u^{-1} \hbar G)^{1/3} = 3 \times 10^{-13}$  m, and a characteristic time of  $\tau_X = c^2/\varepsilon_u = 10^{16}$  years, along with other important properties. Heavy dark matter particles of this mass were shown to have a free streaming mass comparable to its particle mass. This allows us to extend the scaling laws to the mass scale of individual dark matter particles. The potential extension to self-interacting dark matter was also discussed, with relevant scales estimated for a given cross-section  $\sigma/m$  (see Table 5).

The binding energy  $E_X = (\varepsilon_u^5 \hbar^7 G^{-2})^{1/9} = 10^{-9}$  eV strongly suggests a dark radiation field associated with structure formation. This corresponds to either a high-frequency gravitational wave radiation of 200 kHz or a nano-eV axion radiation. If axion is the dark "radiation," it should have a mass  $10^{-9}$  eV with a GUT scale decay constant  $10^{16}$  GeV and an effective axion-photon coupling constant  $10^{-18}$  GeV $^{-1}$ . This work suggests a heavy dark matter scenario with a mass much larger than that of WIMPs and axion or GW dark radiation associated with structure formation and evolution.

## ACKNOWLEDGMENT

This research was supported by Laboratory Directed Research and Development at Pacific Northwest National Laboratory (PNNL). PNNL is a multiprogram national laboratory operated for the U.S. Department of Energy (DOE) by Battelle Memorial Institute under contract no. DE-AC05-76RL01830.

## DATA AVAILABILITY

Two datasets for this article, that is, halo-based and correlation-based statistics of dark matter flow, are available on Zenodo [89, 90] (<http://dx.doi.org/10.5281/zenodo.6541230>), along with the accompanying presentation "A comparative study of dark matter flow & hydrodynamic turbulence and its applications" [91] (<http://dx.doi.org/10.5281/zenodo.6569901>). All data are also available on GitHub [92] (<http://dx.doi.org/10.5281/zenodo.6586212>).

## References

- [1] V. C. Rubin and W. K. Ford, *Astrophysical Journal* **159**, 379 (1970).
- [2] V. C. Rubin, W. K. Ford, and N. Thonnard, *Astrophysical Journal* **238**, 471 (1980).
- [3] P. J. E. Peebles, *ApJ* **263**, L1 (1982).
- [4] N. Aghanim, Y. Akrami, M. Ashdown, J. Aumont, C. Baccigalupi, M. Ballardini, A. J. Banday, R. B. Barreiro, N. Bartolo, S. Basak, R. Battye, K. Benabed, J. P. Bernard, M. Bersanelli, P. Bielewicz, J. J. Bock, J. R. Bond, J. Borrill, F. R. Bouchet, F. Boulanger, M. Bucher, C. Burigana, R. C. Butler, E. Calabrese, J. F. Cardoso, J. Carron, A. Challinor, H. C. Chiang, J. Chluba, L. P. L. Colombo, C. Combet, D. Contreras, B. P. Crill, F. Cuttaia, P. de Bernardis, G. de Zotti, J. Delabrouille, J. M. Delouis, E. Di Valentino, J. M. Diego, O. Dore, M. Douspis, A. Ducout, X. Dupac, S. Dusini, G. Efstathiou, F. Elsner, T. A. Ensslin, H. K. Eriksen, Y. Fantaye, M. Farhang, J. Fergusson, R. Fernandez-Cobos, F. Finelli, F. Forastieri, M. Frailis, A. A. Fraisse, E. Franceschi, A. Frolov, S. Galeotta, S. Galli, K. Ganga, R. T. Genova-Santos, M. Gerbino, T. Ghosh, J. Gonzalez-Nuevo, K. M. Gorski, S. Gratton, A. Gruppuso, J. E. Gudmundsson, J. Hamann, W. Handley, F. K. Hansen, D. Herranz, S. R. Hildebrandt, E. Hivon, Z. Huang, A. H. Jaffe, W. C. Jones, A. Karakci, E. Keihanen, R. Kesitalo, K. Kiiveri, J. Kim, T. S. Kisner, L. Knox, N. Krachmalnicoff, M. Kunz, H. Kurki-Suonio, G. Lagache, J. M. Lamarre, A. Lasenby, M. Lattanzi, C. R. Lawrence, M. Le Jeune, P. Lemos, J. Lesgourgues, F. Levrier, A. Lewis, M. Liguori, *et al.*, *Astronomy & Astrophysics* **652** (2021), [10.1051/0004-6361/201833910](https://doi.org/10.1051/0004-6361/201833910).
- [5] P. J. E. Peebles, *ApJ* **284**, 439 (1984).
- [6] D. N. Spergel, L. Verde, H. V. Peiris, E. Komatsu, M. R. Nolta, C. L. Bennett, M. Halpern, G. Hinshaw, N. Jarosik, A. Kogut, M. Limon, S. S. Meyer, L. Page, G. S. Tucker, J. L. Weiland, E. Wollack, and E. L. Wright, *ApJS* **148**, 175 (2003), [arXiv:astro-ph/0302209](https://arxiv.org/abs/astro-ph/0302209) [astro-ph] .
- [7] E. Komatsu, K. M. Smith, J. Dunkley, C. L. Bennett, B. Gold, G. Hinshaw, N. Jarosik, D. Larson, M. R. Nolta, L. Page, D. N. Spergel, M. Halpern, R. S. Hill, A. Kogut, M. Limon, S. S. Meyer, N. Odegard, G. S. Tucker, J. L. Weiland, E. Wollack, and E. L. Wright, *ApJS* **192**, 18 (2011), [arXiv:1001.4538](https://arxiv.org/abs/1001.4538) [astro-ph.CO] .
- [8] C. S. Frenk and S. D. M. White, *Annalen der Physik* **524**, 507 (2012), [arXiv:1210.0544](https://arxiv.org/abs/1210.0544) [astro-ph.CO] .
- [9] L. Perivolaropoulos and F. Skara, *New Astronomy Reviews* **95**, 101659 (2022).
- [10] J. S. Bullock and M. Boylan-Kolchin, *ARA&A* **55**, 343 (2017), [arXiv:1707.04256](https://arxiv.org/abs/1707.04256) [astro-ph.CO] .
- [11] D. H. Weinberg, J. S. Bullock, F. Governato, R. K. de Naray, and A. H. G. Peter, *Proceedings of the National Academy of Sciences* **112**, 12249 (2015), <https://www.pnas.org/doi/pdf/10.1073/pnas.1308716112> .
- [12] R. A. Flores and J. R. Primack, *ApJ* **427**, L1 (1994), [arXiv:astro-ph/9402004](https://arxiv.org/abs/astro-ph/9402004) [astro-ph] .
- [13] W. J. G. de Blok, *Adv. Astron.* **2010**, 789293 (2010), [arXiv:0910.3538](https://arxiv.org/abs/0910.3538) [astro-ph.CO] .
- [14] A. Klypin, A. V. Kravtsov, O. Valenzuela, and F. Prada, *The Astrophysical Journal* **522**, 82 (1999).
- [15] B. Moore, S. Ghigna, F. Governato, G. Lake, T. Quinn, J. Stadel, and P. Tozzi, *The Astrophysical Journal* **524**, L19 (1999).

- [16] M. Boylan-Kolchin, J. S. Bullock, and M. Kaplinghat, *Monthly Notices of the Royal Astronomical Society: Letters* **415**, L40 (2011).
- [17] M. Boylan-Kolchin, J. S. Bullock, and M. Kaplinghat, *Monthly Notices of the Royal Astronomical Society* **422**, 1203 (2012), <https://academic.oup.com/mnras/article-pdf/422/2/1203/3464467/mnras0422-1203.pdf>.
- [18] K. A. Oman, J. F. Navarro, A. Fattahi, C. S. Frenk, T. Sawala, S. D. M. White, R. Bower, R. A. Crain, M. Furlong, M. Schaller, J. Schaye, and T. Theuns, *Monthly Notices of the Royal Astronomical Society* **452**, 3650 (2015), <https://academic.oup.com/mnras/article-pdf/452/4/3650/18237239/stv1504.pdf>.
- [19] M. Viel, J. Lesgourgues, M. G. Haehnelt, S. Matarrese, and A. Riotto, *Phys. Rev. D* **71**, 063534 (2005).
- [20] M. R. Lovell, V. Eke, C. S. Frenk, L. Gao, A. Jenkins, T. Theuns, J. Wang, S. D. M. White, A. Boyarsky, and O. Ruchayskiy, *Monthly Notices of the Royal Astronomical Society* **420**, 2318 (2012), <https://academic.oup.com/mnras/article-pdf/420/3/2318/3020178/mnras0420-2318.pdf>.
- [21] M. Viel, G. D. Becker, J. S. Bolton, and M. G. Haehnelt, *Phys. Rev. D* **88**, 043502 (2013).
- [22] D. N. Spergel and P. J. Steinhardt, *Phys. Rev. Lett.* **84**, 3760 (2000).
- [23] S. Tulin and H.-B. Yu, *Physics Reports* **730**, 1 (2018), dark matter self-interactions and small scale structure.
- [24] A. Del Popolo and M. Le Delliou, *Galaxies* **5**, 17 (2017), [arXiv:1606.07790 \[astro-ph.CO\]](https://arxiv.org/abs/1606.07790).
- [25] G. Steigman and M. S. Turner, *Nuclear Physics B* **253**, 375 (1985).
- [26] G. Jungman, M. Kamionkowski, and K. Griest, *Physics Reports-Review Section of Physics Letters* **267**, 195 (1996).
- [27] K. Griest and M. Kamionkowski, *Physical Review Letters* **64**, 615 (1990).
- [28] L. D. Duffy and K. van Bibber, *New Journal of Physics* **11**, 105008 (2009).
- [29] A. Mazumdar, S. Qutub, and K. Saikawa, *Phys. Rev. D* **94**, 065030 (2016).
- [30] D. J. E. Marsh, *Phys. Rep.* **643**, 1 (2016), [arXiv:1510.07633 \[astro-ph.CO\]](https://arxiv.org/abs/1510.07633).
- [31] C. S. Frenk, J. M. Colberg, H. M. P. Couchman, G. Efstathiou, A. E. Evrard, A. Jenkins, T. J. MacFarland, B. Moore, J. A. Peacock, F. R. Pearce, P. A. Thomas, S. D. M. White, and N. Yoshida, [arXiv:astro-ph/0007362v1](https://arxiv.org/abs/astro-ph/0007362v1) (2000), 10.48550/arXiv.astro-ph/0007362.
- [32] A. Jenkins, C. S. Frenk, F. R. Pearce, P. A. Thomas, J. M. Colberg, S. D. M. White, H. M. P. Couchman, J. A. Peacock, G. Efstathiou, and A. H. Nelson, *Astrophysical Journal* **499**, 20 (1998).
- [33] E. Bertschinger, *Phys. Rev. D* **74**, 063509 (2006).
- [34] J. E. Gunn and J. R. Gott, *Astrophysical Journal* **176**, 1 (1972).
- [35] C. Blanco, M. S. Delos, A. L. Erickcek, and D. Hooper, *Phys. Rev. D* **100**, 103010 (2019), [arXiv:1906.00010 \[astro-ph.CO\]](https://arxiv.org/abs/1906.00010).
- [36] Z. Xu, *Physics of Fluids* **35**, 077105 (2023), [arXiv:2202.00910 \[astro-ph\]](https://arxiv.org/abs/2202.00910).
- [37] P. Meszaros, *A&A* **37**, 225 (1974).
- [38] Z. Xu, [arXiv e-prints](https://arxiv.org/abs/2110.05784), [arXiv:2110.05784](https://arxiv.org/abs/2110.05784) (2021).
- [39] Z. Xu, *Scientific Reports* **13**, 16531 (2023), [arXiv:2210.01200 \[astro-ph\]](https://arxiv.org/abs/2210.01200).
- [40] Z. Xu, [arXiv e-prints](https://arxiv.org/abs/2109.09985), [arXiv:2109.09985](https://arxiv.org/abs/2109.09985) (2021).
- [41] M. Castellano, A. Fontana, T. Treu, P. Santini, E. Merlin, N. Leethochawalit, M. Trenti, E. Vanzella, U. Mestric, A. Bonchi, D. Belfiori, M. Nonino, D. Paris, G. Polenta, G. Roberts-Borsani, K. Boyett, M. Bradač, A. Calabrò, K. Glazebrook, C. Grillo, S. Mascia, C. Mason, A. Mercurio, T. Morishita, T. Nanayakkara, L. Pentericci, P. Rosati, B. Vulcani, X. Wang, and L. Yang, *The Astrophysical Journal Letters* **938**, L15 (2022).
- [42] J. L. Feng, *Ann. Rev. Astron. Astrophys.* **48**, 495 (2010), [arXiv:1003.0904 \[astro-ph.CO\]](https://arxiv.org/abs/1003.0904).
- [43] K. L. Pandey, T. Karwal, and S. Das, *Journal of Cosmology and Astroparticle Physics* **2020**, 026 (2020).
- [44] A. Chen, D. Huterer, S. Lee, A. Ferté, N. Weaverdyck, O. Alves, C. D. Leonard, N. MacCrann, M. Raveri, A. Porredon, E. Di Valentino, J. Muir, P. Lemos, A. R. Liddle, J. Blazek, A. Campos, R. Cawthon, A. Choi, S. Dodelson, J. Elvin-Poole, D. Gruen, A. J. Ross, L. F. Secco, I. Sevilla-Noarbe, E. Sheldon, M. A. Troxel, J. Zuntz, T. M. C. Abbott, M. Aguena, S. Allam, J. Annis, S. Avila, E. Bertin, S. Bhargava, S. L. Bridle, D. Brooks, A. Carnero Rosell, M. Carrasco Kind, J. Carretero, M. Costanzi, M. Crocce, L. N. da Costa, M. E. S. Pereira, T. M. Davis, P. Doel, T. F. Eifler, I. Ferrero, P. Fosalba, J. Frieman, J. García-Bellido, E. Gaztanaga, D. W. Gerdes, R. A. Gruendl, J. Gschwend, G. Gutierrez, S. R. Hinton, D. L. Hollowood, K. Honscheid, B. Hoyle, D. J. James, M. Jarvis, K. Kuehn, O. Lahav, M. A. G. Maia, J. L. Marshall, F. Menanteau, R. Miquel, R. Morgan, A. Palmese, F. Paz-Chinchón, A. A. Plazas, A. Roodman, E. Sanchez, V. Scarpine, M. Schubnell, S. Serrano, M. Smith, E. Suchyta, G. Tarle, D. Thomas, C. To, T. N. Varga, J. Weller, and R. D. Wilkinson (DES Collaboration), *Phys. Rev. D* **103**, 123528 (2021).
- [45] O. Seto and Y. Toda, *Phys. Rev. D* **103**, 123501 (2021).
- [46] Z. Xu, *A&A* **675**, A92 (2023), [arXiv:2110.03126 \[astro-ph\]](https://arxiv.org/abs/2110.03126).
- [47] J. Neyman and E. L. Scott, *Astrophysical Journal* **116**, 144 (1952).
- [48] A. Cooray and R. Sheth, *Physics Reports-Review Section of Physics Letters* **372**, 1 (2002).
- [49] D. Nelson, A. Pillepich, S. Genel, M. Vogelsberger, V. Springel, P. Torrey, V. Rodriguez-Gomez, D. Sijacki, G. Snyder, B. Griffen, F. Marinacci, L. Blecha, L. Sales, D. Xu, and L. Hernquist, *Astronomy and Computing* **13**, 12 (2015).
- [50] H. J. Mo and S. D. M. White, *MNRAS* **336**, 112 (2002), [arXiv:astro-ph/0202393 \[astro-ph\]](https://arxiv.org/abs/astro-ph/0202393).
- [51] P. J. E. Peebles, *The Large-Scale Structure of the Universe* (Princeton University Press, Princeton, NJ, 1980).
- [52] Z. Xu, [arXiv e-prints](https://arxiv.org/abs/2202.04054), [arXiv:2202.04054](https://arxiv.org/abs/2202.04054) (2022).
- [53] W. M. Irvine, *Local Irregularities in a Universe Satisfying the Cosmological Principle*, Thesis, HARVARD UNIVERSITY (1961).
- [54] D. Layzer, *Astrophysical Journal* **138**, 174 (1963).
- [55] Z. Xu, *Research Square* (2024), 10.21203/rs.3.rs-4039565/v1, [Research Square:4039565 \[astro-ph\]](https://arxiv.org/abs/2403.09565).
- [56] L. F. Richardson, *Weather Prediction by Numerical Process* (Cambridge University Press, Cambridge, UK, 1922).
- [57] A. N. Kolmogoroff, *Comptes Rendus De L Academie Des Sciences De L Urss* **32**, 16 (1941).
- [58] Z. Xu, *Scientific Reports* **13**, 4165 (2023), [arXiv:2209.03313 \[astro-ph\]](https://arxiv.org/abs/2209.03313).
- [59] J. F. Navarro, C. S. Frenk, and S. D. M. White, *Astrophysical Journal* **490**, 493 (1997).
- [60] J. F. Navarro, A. Ludlow, V. Springel, J. Wang, M. Vogelsberger, S. D. M. White, A. Jenkins, C. S. Frenk, and

- A. Helmi, *Monthly Notices of the Royal Astronomical Society* **402**, 21 (2010), <https://academic.oup.com/mnras/article-pdf/402/1/21/18573804/mnras0402-0021.pdf>.
- [61] J. Diemand and B. Moore, *Advanced Science Letters* **4**, 297 (2011), [arXiv:0906.4340 \[astro-ph.CO\]](https://arxiv.org/abs/0906.4340).
- [62] F. Governato, C. Brook, L. Mayer, A. Brooks, G. Rhee, J. Wadsley, P. Jonsson, B. Willman, G. Stinson, T. Quinn, and P. Madau, *Nature* **463**, 203 (2010).
- [63] D. McKeown, J. S. Bullock, F. J. Mercado, Z. Hafen, M. Boylan-Kolchin, A. Wetzel, L. Necib, P. F. Hopkins, and S. Yu, *MNRAS* **513**, 55 (2022), [arXiv:2111.03076 \[astro-ph.GA\]](https://arxiv.org/abs/2111.03076).
- [64] J. Wang, S. Bose, C. S. Frenk, L. Gao, A. Jenkins, V. Springel, and S. D. M. White, *Nature* **585**, 39 (2020), [arXiv:1911.09720 \[astro-ph.CO\]](https://arxiv.org/abs/1911.09720).
- [65] H. Mo, F. van den Bosch, and S. White, *Galaxy formation and evolution* (Cambridge University Press, Cambridge, 2010).
- [66] J. J. Adams, J. D. Simon, M. H. Fabricius, R. C. E. van den Bosch, J. C. Barentine, R. Bender, K. Gebhardt, G. J. Hill, J. D. Murphy, R. A. Swaters, J. Thomas, and G. van de Ven, *ApJ* **789**, 63 (2014), [arXiv:1405.4854 \[astro-ph.GA\]](https://arxiv.org/abs/1405.4854).
- [67] F. Lelli, S. S. McGaugh, and J. M. Schombert, *AJ* **152**, 157 (2016), [arXiv:1606.09251 \[astro-ph.GA\]](https://arxiv.org/abs/1606.09251).
- [68] P. Li, F. Lelli, S. McGaugh, and J. Schombert, *ApJS* **247**, 31 (2020), [arXiv:2001.10538 \[astro-ph.GA\]](https://arxiv.org/abs/2001.10538).
- [69] T. P. K. Martinsson, M. A. W. Verheijen, K. B. Westfall, M. A. Bershadsky, D. R. Andersen, and R. A. Swaters, *A&A* **557**, A131 (2013), [arXiv:1308.0336 \[astro-ph.CO\]](https://arxiv.org/abs/1308.0336).
- [70] Y. Sofue, *Publications of the Astronomical Society of Japan* **68** (2016), 10.1093/pasj/psv103.
- [71] P. Abreu, M. Aglietta, J. M. Albury, I. Allekotte, K. Almeida Cheminant, A. Almela, R. Aloisio, J. Alvarez-Muñiz, R. Alves Batista, J. Ammerman Yebra, G. A. Anastasi, L. Anchordoqui, B. Andrada, S. Andringa, C. Aramo, P. R. Araújo Ferreira, E. Arnone, J. C. Arteaga Velázquez, H. Asorey, P. Assis, G. Avila, E. Avocone, A. M. Badescu, A. Bakalova, A. Balaceanu, F. Barbato, J. A. Bellido, C. Berat, M. E. Bertaina, G. Bhatta, P. L. Biermann, V. Binet, K. Bismark, T. Bister, J. Biteau, J. Blazek, C. Bleve, J. Blümer, M. Boháčová, D. Boncioli, C. Bonifazi, L. Bonneau Arbeletche, N. Borodai, A. M. Botti, J. Brack, T. Bretz, P. G. Brichetto Orcheria, F. L. Briechle, P. Buchholz, A. Bueno, S. Buitink, M. Buscemi, M. Büsken, K. S. Caballero-Mora, L. Caccianiga, F. Canfora, I. Caracas, R. Caruso, A. Castellina, F. Catalani, G. Cataldi, L. Cazon, M. Cerdá, J. A. Chinellato, J. Chudoba, L. Chytka, R. W. Clay, A. C. Cobos Cerutti, R. Colalillo, A. Coleman, M. R. Coluccia, R. Conceição, A. Condorelli, G. Consolati, F. Contreras, F. Convenga, D. Correia dos Santos, C. E. Coval, S. Dasso, K. Daumiller, B. R. Dawson, J. A. Day, R. M. de Almeida, J. de Jesús, S. J. de Jong, J. R. T. de Mello Neto, I. De Mitri, J. de Oliveira, D. de Oliveira Franco, F. de Palma, V. de Souza, E. De Vito, A. Del Popolo, M. del Río, O. Deligny, L. Deval, A. di Matteo, M. Dobre, C. Dobrigkeit, J. C. D'Olivo, L. M. Domingues Mendes, R. C. dos Anjos, M. T. Dova, J. Ebr, R. Engel, I. Epicoco, M. Erdmann, C. O. Escobar, A. Etchegoyen, H. Falcke, J. Farmer, G. Farrar, A. C. Fauth, N. Fazzini, F. Feldbusch, F. Fenu, B. Fick, J. M. Figueira, A. Filipčič, T. Fitoussi, T. Fodran, T. Fujii, A. Fuster, C. Galea, C. Galelli, B. García, A. L. García Vegas, H. Gemeke, F. Gesualdi, A. Gherghel-Lascu, P. L. Ghia, U. Giaccari, M. Giammarchi, J. Glombitza, F. Gobbi, F. Gollan, G. Golup, M. Gómez Berisso, P. F. Gómez Vitale, J. P. Gongora, J. M. González, N. González, I. Goos, D. Góra, A. Gorgi, M. Gottowik, T. D. Grubb, F. Guarino, G. P. Guedes, E. Guido, S. Hahn, P. Hamal, M. R. Hampel, P. Hansen, D. Harari, V. M. Harvey, A. Haungs, T. Hebbeker, D. Heck, G. C. Hill, C. Hojvat, J. R. Hörandel, P. Horvath, M. Hrabovský, T. Huege, A. Insolia, P. G. Isar, P. Janeczek, J. A. Johnsen, J. Jurysek, A. Kääpä, K. H. Kampert, B. Keilhauer, A. Khakurdikar, V. V. Kizakke Covilakam, H. O. Klages, M. Kleifges, J. Kleinfeller, F. Knapp, N. Kunka, B. L. Lago, N. Langner, M. A. Leigui de Oliveira, V. Lenok, A. Letessier-Selvon, I. Lhenry-Yvon, D. Lo Presti, L. Lopes, R. López, L. Lu, Q. Luce, J. P. Lundquist, A. Machado Payeras, G. Mancarella, D. Mandat, B. C. Manning, J. Manshanden, P. Mantsch, S. Marafico, F. M. Mariani, A. G. Mariazzi, I. C. Mariş, G. Marsella, D. Martello, S. Martinelli, O. Martínez Bravo, M. Mastrodicasa, H. J. Mathes, J. Matthews, G. Matthiae, E. Mayotte, S. Mayotte, P. O. Mazur, G. Medina-Tanco, D. Melo, A. Menshikov, S. Michal, M. I. Micheletti, L. Miramonti, S. Mollerach, F. Montanet, L. Morejon, C. Morello, M. Mostafá, A. L. Müller, M. A. Muller, K. Mulrey, R. Mussa, M. Muzio, W. M. Namasaka, A. Nasr-Esfahani, L. Nellen, G. Nicora, M. Niculescu-Oglinzanu, M. Niechciol, D. Nitz, I. Norwood, D. Nosek, V. Novotny, L. Nožka, A. Nucita, L. A. Núñez, C. Oliveira, M. Palatka, J. Pallotta, P. Papenbreer, G. Parente, A. Parra, J. Pawlowsky, M. Pech, J. Pekala, R. Pelayo, J. Peña-Rodríguez, E. E. Pereira Martins, J. Perez Armand, C. Pérez Bertolli, L. Perrone, S. Petrerá, C. Petrucci, T. Pierog, M. Pimenta, V. Pirronello, M. Platino, B. Pont, M. Pothast, P. Privitera, M. Prouza, A. Puyleart, S. Querschfeld, J. Rautenberg, D. Ravignani, M. Reininghaus, J. Ridky, F. Riehn, M. Risse, V. Rizzi, W. Rodrigues de Carvalho, J. Rodriguez Rojo, M. J. Roncoroni, S. Rossoni, M. Roth, E. Roulet, A. C. Rovero, P. Ruehl, A. Saftoiu, M. Saharan, F. Salamida, H. Salazar, G. Salina, J. D. Sanabria Gomez, F. Sánchez, E. M. Santos, E. Santos, F. Sarazin, R. Sarmento, C. Sarmiento-Cano, R. Sato, P. Savina, C. M. Schäfer, V. Scherini, H. Schieler, M. Schimassek, M. Schimp, F. Schlüter, D. Schmidt, O. Scholten, H. Schoorlemmer, P. Schovánek, F. G. Schröder, J. Schulte, T. Schulz, S. J. Sciutto, M. Scornavacche, A. Segreto, S. Sehgal, R. C. Shellard, G. Sigl, G. Silli, O. Sima, R. Smay, R. Šmída, P. Sommers, J. F. Soriano, R. Squartini, M. Stadelmaier, D. Stanca, S. Stanič, J. Stasielak, P. Stassi, A. Streich, M. Suárez-Durán, T. Sudholz, T. Suomijärvi, A. D. Supanitsky, Z. Szadkowski, A. Tapia, C. Taricco, C. Timmermans, O. Tkachenko, P. Tobiska, C. J. Todero Peixoto, B. Tomé, Z. Torrès, A. Travaini, P. Travnicek, C. Trimarelli, M. Tueros, R. Ulrich, M. Unger, L. Vaclavek, M. Vacula, J. F. Valdés Galicia, L. Valore, E. Varela, A. Vázquez-Ramírez, D. Vebrič, C. Ventura, I. D. Vergara Quispe, V. Verzi, J. Vicha, J. Vink, S. Vorobiov, H. Wahlberg, C. Watanabe, A. A. Watson, A. Weindl, L. Wiencke, H. Wilczyński, D. Wittkowski, B. Wundheiler, A. Yushkov, O. Zapparrata, E. Zas, D. Zavrtanik, M. Zavrtanik, L. Zehrer, and Pierre Auger Collaboration, *Phys. Rev. D* **107**, 042002 (2023), [arXiv:2208.02353 \[astro-ph.HE\]](https://arxiv.org/abs/2208.02353).
- [72] A. Eichhorn, H. Gies, J. Jaeckel, T. Plehn, M. M. Scherer, and R. Sondenheimer, *JHEP* **04**, 022 (2015), [arXiv:1501.02812 \[hep-ph\]](https://arxiv.org/abs/1501.02812).
- [73] G. Goswami and S. Mohanty, *Phys. Lett. B* **751**, 113 (2015), [arXiv:1406.5644 \[hep-ph\]](https://arxiv.org/abs/1406.5644).
- [74] L. H. Ford, *Phys. Rev. D* **35**, 2955 (1987).
- [75] J. Haro and L. A. Saló, *Phys. Rev. D* **100**, 043519 (2019).

- [76] D. J. H. Chung, E. W. Kolb, and A. Riotto, *Physical Review D* **59** (1999), 10.1103/PhysRevD.59.023501.
- [77] E. W. Kolb and A. J. Long, *Physical Review D* **96** (2017), 10.1103/PhysRevD.96.103540.
- [78] J. Ellis, J. L. Lopez, and D. V. Nanopoulos, *Physics Letters B* **247**, 257 (1990).
- [79] K. Benakli, J. Ellis, and D. V. Nanopoulos, *Phys. Rev. D* **59**, 047301 (1999), [arXiv:hep-ph/9803333 \[hep-ph\]](#).
- [80] D. Carney, N. Raj, Y. Bai, J. Berger, C. Blanco, J. Bramante, C. Cappiello, M. Dutra, R. Ebadi, K. Engel, E. Kolb, J. P. Harding, J. Kumar, G. Krnjaic, R. F. Lang, R. K. Leane, B. V. Lehmann, S. Li, A. J. Long, G. Mohlabeng, I. Olcina, E. Pueschel, N. L. Rodd, C. Rott, D. Sengupta, B. Shakya, R. L. Walsworth, and S. Westerdale, “Snowmass2021 cosmic frontier white paper: Ultraheavy particle dark matter,” (2022).
- [81] C. Blanco, B. Elshimy, R. F. Lang, and R. Orlando, *Physical Review D* **105** (2022), 10.1103/physrevd.105.115031.
- [82] M. Shaposhnikov, *Nuclear Physics B* **1003**, 116496 (2024), special Issue of Nobel Symposium 182 on Dark Matter.
- [83] M. Fukugita and T. Yanagida, *Phys. Lett. B* **174**, 45 (1986).
- [84] W. F. Vinen, *Phys. Rev. B* **64**, 134520 (2001).
- [85] N. Aggarwal, G. P. Winstone, M. Teo, M. Baryakhtar, S. L. Larson, V. Kalogera, and A. A. Geraci, *Phys. Rev. Lett.* **128**, 111101 (2022).
- [86] F. Chadha-Day, J. Ellis, and D. J. E. Marsh, *Science Advances* **8**, eabj3618 (2022), <https://www.science.org/doi/pdf/10.1126/sciadv.abj3618>.
- [87] Y. K. Semertzidis and S. Youn, *Science Advances* **8**, eabm9928 (2022), <https://www.science.org/doi/pdf/10.1126/sciadv.abm9928>.
- [88] M. Rocha, A. H. G. Peter, J. S. Bullock, M. Kaplinghat, S. Garrison-Kimmel, J. Oñorbe, and L. A. Moustakas, *Monthly Notices of the Royal Astronomical Society* **430**, 81 (2013), <https://academic.oup.com/mnras/article-pdf/430/1/81/3064615/sts514.pdf>.
- [89] Z. Xu, “Dark matter flow dataset part i: Halo-based statistics from cosmological n-body simulation,” (2022).
- [90] Z. Xu, “Dark matter flow dataset part ii: Correlation-based statistics from cosmological n-body simulation,” (2022).
- [91] Z. Xu, “A comparative study of dark matter flow & hydrodynamic turbulence and its applications,” (2022).
- [92] Z. Xu, “Dark matter flow dataset,” (2022).